BEHRUZ KARDAN

CENTRALITY DETERMINATION AT 1.23 AGEV GOLD-GOLD COLLISION AND READOUT-ELECTRONICS FOR THE HADES ELECTROMAGNETIC CALORIMETER

GOETHE UNIVERSITÄT

Centrality Determination at 1.23 AGeV Gold-Gold collision
and readout-electronics for the HADES electromagnetic calorimeter

vorgelegt am Fachbereich Physik der Johann Wolfgang Goethe-Universität in Frankfurt am Main.

Behruz Kardan, *Juni 2015*

Dedicated to my mother.

Contents

Introduction **7**
- Elementary particles and fundamental forces 7
- Heavy-ion collisions 10
- Quantum Chromodynamics Phase Diagram 11
- Motivation and goal of the thesis 12

The HADES Experiment **19**
- Physics program and beamtimes 19
- Detector & Requirements 20
- Particle Identification 22
- Physical principle of electromagnetic calorimeter 23
- Schwerionen-Synchrotron SIS18 25
- Segmented Target 26
- Diamond START- and VETO-counter 26
- DAQ, Central-Trigger-System (CTS) & slow control 27
- Analysis Framework 27
- Magnetic Spectrometer 29
- Time of flight measurement 32
- Electron and Hadron separation 34

Electromagnetic Calorimeter for HADES **43**
- Module Properties 44
- Readout Scheme and Electronics 46
- Test Results & Beam-Time 50
- Performance & Simulation 56

Glauber Model Framework **61**
- Limitation of the Glauber Model at low energies 62
- Geometrical picture of nucleus-nucleus collision 63
- Glauber Monte Carlo 65
- Parameter range and systematic errors 67
- Calculated quantities 72
- Total reaction cross section 77
- Centrality classes 79

Methods of Event Characterization **93**
Centrality Estimators 93
Cross section and trigger bias determination 96
Event selection 100
Centrality Determination via Glauber-fit 104
Particle multiplicity and centrality dependence 108

Danksagung **113**

Introduction

This Century-old question about the structure of matter and its elementary building blocks drive generation of philosophers and scientists. The idea that matter is composed of indivisible and indestructible entities called *atoms* and filled with empty space in between was conceived in the 5th century BCE by Democritus and his mentor Leucippus [35]. In contrary, Aristoteles argued that matter is build up by continuous elements of fire, air, earth, and water and their transformation into each other. Both ideas can be understood as the origin of our modern view of matter and its different states. But this ancient concepts were based entirely upon philosophical considerations and it took until the 19th century, that these hypothesis could be tested empirically by experiments.

Elementary particles and fundamental forces

The first discovered elementary particle was the *electron*. 1897 J.J. Thomson concluded that cathode rays consist of negatively charged particles following measurements of the mass-to-charge ratio m/e. [15] By the deflection in a transverse electric field he determined the *charge*, with an additional compensating perpendicular magnetic field the *velocity* and in combination with the accumulated charge and the generated heat at a collector he could determine the mass of the *electron*. His estimation of the mass of the electron was three magnitudes smaller than the mass of a hydrogen ion [39]. Besides many others, his experimental methods in contrast to the previously used methods of chemistry, introduced the new field of experimental particle physics. A decade later, in 1911, Rutherford together with Geiger and Marsden showed with their scattering experiments, where a gold foil was bombarded with α-particles, that the mass of an atom is concentrated in a massive centre carrying a positive charge, - the atomic *nucleus* [37].

With one of the first nuclear reaction Rutherford was able to show the existence of the *proton* as constituent of the atomic nucleus. Using alpha particles directed at nitrogen, one hydrogen nucleus was knocked out, producing oxygen by the nuclear transmutation (see fig. 1) [36, 8].

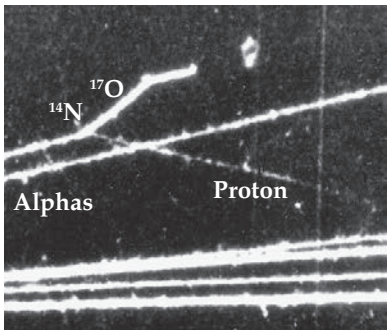

Figure 1: Picture of a cloud chamber photograph made in 1925 [8, 38] from the nuclear reaction $^{14}N + \alpha \rightarrow {}^{17}O + p$. First conducted by Rutherford in 1917 [36].

With the discovery of the *neutron* by Chadwick in 1932 [17] the building blocks of matter were simplified from around 90 different chemical elements to three constituents: *electron*, *proton* and *neutron*.

In the following years, by studying Cloud Chamber photographs of high energetic cosmic radiation, the *positron* was found 1932 by Anderson [2] and together with his student Neddermeyer the *muon* four years later (1936) [3]. They were also able to proof the existence of the *positron* with a further experiment, where they produced *positron-electron* pairs by radiating a lead plate with a gamma-source ("Thorium C" ,^{208}Tl) [4]. This could be seen as the first conducted *di-lepton* experiment and it was followed independently in similar ways by Curie and Joliot and by Meitner and Philipp in early 1933. A near ten year long search, using further developed photographic emulsions, sensitive even to minimum ionization of charged particles, exposed at high-altitude mountains, lead to the discovery of the *pion* in 1947 by Powell and his collaborators [33, 29, 13]. In figure 2 the complete decay chain of a charged cosmic pion to a muon and the successive decay to an electron is shown. Up to now cosmic muons with their relative long lifetimes are one of the practical sources to calibrate or measure the alignment of detector systems. Around the same year (1947) Rochester and Butler [34] observed

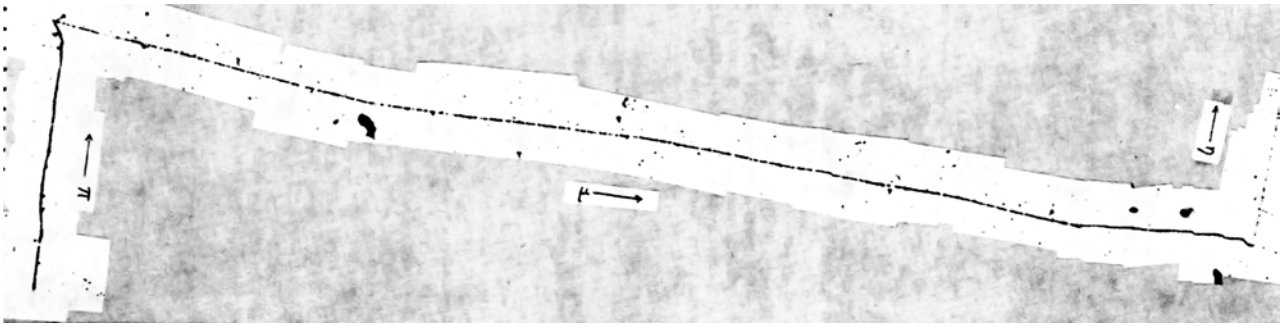

Figure 2: Image of the decay chain of a cosmic pion taken in 1948 [13] with a electron-sensitive emulsions. The incoming pion (down-left), leaving a strong track, decays into a muon. Its abrupt change in direction results from the emission of an invisible lightweight neutrino. The muon leaves a more and more denser track shortly before decaying into an electron visible as a faint track and a second invisible neutrino.

in cosmic-rays, beside pions and muons, a new type of unstable particle with curiously V-shaped tracks - the first strange particles. Further analysis by Brown et al. [14] and Armenteros et al. [6] revealed a second kind of heavier strange particle decaying into an additional proton. These strange particles, known today as kaons and lambdas are produced by the strong interactions and only decay via the weak interaction.

With the advent of particle accelerators, powerful enough to produce these newly discovery particles, their detailed properties could be studied under controlled conditions. One of the first successes was the observation of pions produced in a carbon-target with alpha-particles accelerated to 380 MeV with the 184 inch *synchronized cyclotron* build by Lawrence in Berkeley [22]. Soon larger accelerators, *e.g.* Cosmotron (3.3 GeV, 1953–1968), Bevatron (6.2 GeV, 1954–1971),

Synchrophasotron (10 GeV, 1957-2003), PS (28 GeV, 1959–now) and AGS (33 GeV, 1960–now), were build and the list of newly discovered particle and their exited states was growing. This motivated the search for an underlying model to categorize the different particles species. In 1957 Gell-Mann and Rosenfeld summarized the properties of the observed particles in an review [24], which is one of the predecessor of todays *Particle Data Book*.

The answer to the diversity of particle species came 1964 from Gell-Mann [23] and Zweig [40]. The observed particles are not elementary objects, but are built from more basic constituents, Gell-Mann called the *quarks*. The experimental evidence for point-like constituents inside protons was shown in 1968 at the Stanford Linear Accelerator Centre with electron-proton deep-inelastic scattering experiments [9, 12]. The postulated idea of the *quark model*, now 50 years old, can up to now describe all observed mesons (quark-antiquark bound state) and baryons (three quark bound state) by six *quark flavors* (u, d, s, c, b, t). Like the six *leptons* $(e, \nu_e, \mu, \nu_\mu, \tau, \nu_\tau)$, the *quarks* are grouped into three generations, but with the difference that each *quark-flavor* has three versions, characterized by the quantum number *color* (see fig. 3).

It took nearly ten years (1972) for the formulation of the the *Quantum Chromodynamics* (QCD) as the underlying quantum field theory of the strong force. By describing the coupling of *gluons* to the *color-charge* of the quarks and gluons themselves, two features of QCD became apparent. One is the *color confinement*, a consequence of the fact that the *color-charge* is not directly observable and the hadron spectrum contains only color neutral states. The other, called the *asymptotic freedom* [25, 32], is describing that the strength of the strong interaction becomes asymptotically weaker with increasing energy, thus probing smaller distances. To illustrate this the *running coupling constant* α_s (see fig. 4) rises towards smaller *momentum transfer* Q:

$$\alpha_s(q^2) = \frac{12\pi}{(33 - 2n_f)\ln(q^2/\Lambda^2)} \tag{1}$$

here Λ is the QCD scale parameter, q the 4-momentum transfer and n_f the number of flavors. In other words, at very small distances quarks behave as free particles up to the resolution scale of a nucleon, where they are confined. While this behavior at large momentum transfers can be treated with perturbation theory, the description of the interactions at small momentum transfers has to rely on effective models. The understanding of *color confinement* and *mass generation* in QCD is one of the unanswered key question in modern physics.

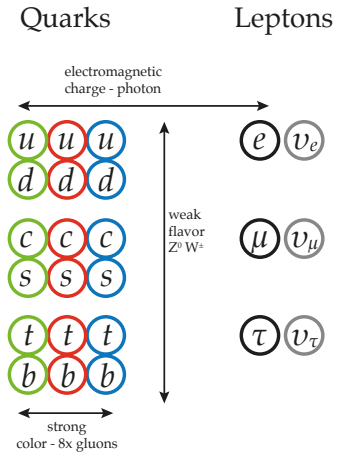

Figure 3: The six *leptons* $(e, \nu_e, \mu, \nu_\mu, \tau, \nu_\tau)$ and the six *quarks* (u, d, s, c, b, t) are grouped into three generations, their flavor is the source of the weak interaction, which is mediated by the W^0 and $Z^\pm$ bosons. Each *quark-flavor* has three *colored* versions, where their *color-charge* is the source of the *strong force* mediated by eight *colored* gluons. Beside the *neutrinos* all elementary particles are charged and experience *electromagnetic interaction* by the *photon*.

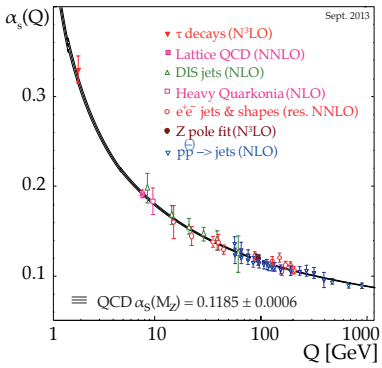

Figure 4: The coupling constant of the strong interaction as a function of momentum transfer squared $Q^2 = -q^2$. Experimental values are shown. (from ref. [30]

Heavy-ion collisions

For the understanding of the properties of matter governed by the strong interaction, a common characterization, is the *QCD phase diagram*. It maps the relationship between net-baryon density and temperature and and depends on the *Equation of State* (EOS) of nuclear matter. It is distinguished into ordinary nuclear, hadronic and partonic matter by the available degrees of freedom. To systematically investigate the phases of QCD matter by the creation of high energy densities in the laboratory, heavy-ion collisions provide the only choice. By the variation of the collision energy and the system size, different regions of the QCD phase diagram can be probed experimentally. At very high energies, provided by the LHC at CERN or RHIC at BNL, a state of matter with nearly vanishing chemical potential can be created with similar properties as the matter in the early universe about 10 microseconds after the Big Bang. At the lowest relativistic energy domain ($E_{lab} \simeq 1 - 2$ AGeV), nuclear matter with extreme net-baryon densities up to three times the ground state matter density can be studied. At different stages in the evolution of heavy-ion collisions various physics observables are formed. The systematic survey of these as a function of beam energy and system size, can reveal the complex dynamics of nucleus-nucleus collisions. The first stage of a heavy-ion reaction, called the *initial*

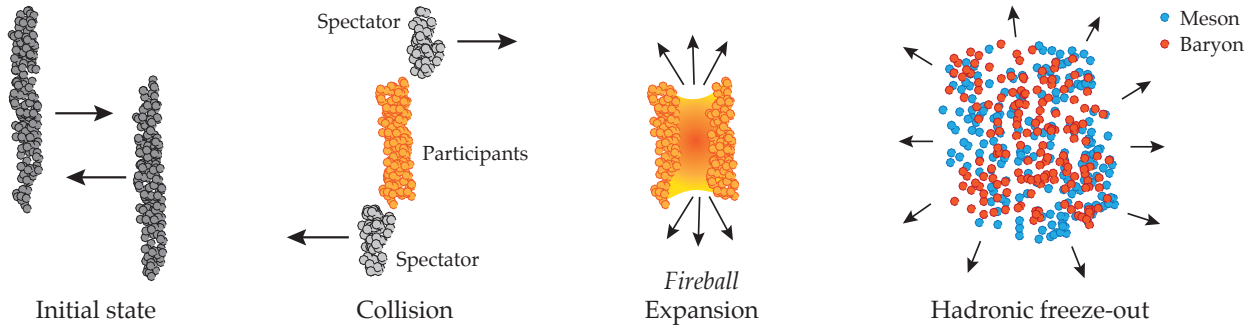

state interaction, is commonly pictured as two Lorentz-contracted nuclei in the ground state where the configuration of the nucleons are approximated to be frozen. The geometrical aspects of the collision are characterized by the transverse distance between their centers (*impact parameter*) and their angular orientation (*reaction plane*). The reaction cross section in therms of the overall surviving probabilities of the individual scattered nucleons can be achieved by the Glauber Model and is the topic of Chapter 4. The kinetic energy of the collision is converted into compression energy in the pre-equilibrium stage and is released during the thermalization of this high density phase in a collectively expanding system. Once the system cools down to the critical tem-

perature hadrons form (*hadronization*) and once no sequential inelastic collisions occur any more the *chemical freeze-out* point is reached, *i.e.* the observable particle abundances get fixed. In the further development the phase space distributions of the hadrons changes until the *kinetic freeze-out* is reached, where elastic collision cease. Observables of bulk properties, like radial, directed and elliptic flow, as well the abundance of fragments due to coalescence, remain unchanged. The measurement of particle correlations (*femtoscopy*) provides informations on the space-time freeze-out volume at this stage. The goal is to find signatures that preserve the information of the subsequent stages, *e.g.* electromagnetic probes.

Quantum Chromodynamics Phase Diagram

The phases of strongly interacting matter and their transformations are some of the key questions of nuclear physics. The phase diagram of nuclear matter can be parameterized by the temperature T and the baryo-chemical potential μ_B and is shown in figure 5. The

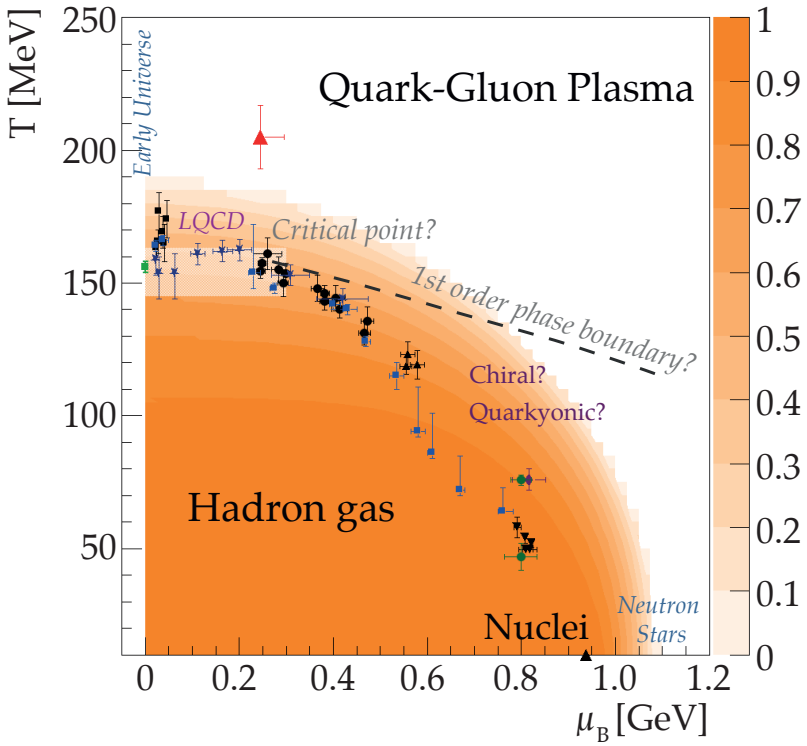

Figure 5: Sketch of the phase diagram of QCD matter including data points in T and μ_B describing the final hadro-chemical freeze-out from grand canonical statistical model. Adapted from [21]

best empirically observed region in this diagram, is nuclear matter at ground state density $\rho_0 = 0.16$ fm^{-3}, equivalent to energy density at $\epsilon_0 \approx 0.14$ GeV fm^3 and zero temperature. Here nuclei exist as a *quantum liquid*, a system of up to hundreds of nucleons bound by the nuclear

forces. At low excitations energies of around 10 MeV per nucleon a liquid-gas phase transition is believed to occur [31]. In the energy regime of relativistic heavy-ion collisions the produced energy densities are high enough to excite nucleons into baryonic resonances. It is expected that this excited baryons and the other produced particles, create a state of hadronic matter. This hadronic phase relies only on hadronic degrees of freedom of *color-confined* hadrons. For sufficiently large energy densities the system is expected to be in a *de-confined* phase with quarks and gluons as the relevant degrees of freedom. This *de-confined* phase is named *Quark-Gluon Plasma* (QGP). Very early after the development of QCD, Cabibbo and Parisi (1975) [16] formulated the idea of a phase transition between confined/de-confined matter based on the physical interpretation of the Hagedorn limiting temperature [26]. Recent results of lattice QCD calculations [27, 1, 19] predict the phase transformation between confined hadrons and de-confined quarks and gluons at vanishing baryo-chemical potentials ($\mu_B \rightarrow 0$ MeV), with a smooth *cross-over* between the two phases, and at a temperatures of about $150 - 160$ MeV [11]. For higher baryo-chemical potentials it is expected that the parton-hadron phase boundary changes from a *cross-over* to a *first order phase transition*, with the consequence of a hypothetical *critical end-point*. For the description of *hadronization* at the parton-hadron phase boundary line, the measured hadron production data are used to determine the degree of chemical equilibration. The *statistical hadronization model* (SHM) [18, 7, 5] and the *hadron resonance gas* (HRG) model [10, 28] are used for the extraction of the chemical freeze-out parameters T_{ch} and μ_B. It should be emphasized that regardless of the oversimplified description neglecting dynamics, these models are in good agreement with the experimental abundancies [20]. A smooth interpolation of these points by the hadro-chemical freeze-out curve [18] is shown in figure 5.

Motivation and goal of the thesis

The main goal of this work is the determination of the reaction centrality and the study of the event characteristics of Au+Au collisions at 1.23 AGeV data taken with HADES in the framework of a Glauber Model in the Monte Carlo approach. Furthermore, the development, test and commissioning of the new Electromagnetic Calorimeter (ECAL) detector, including the proposed readout system, is described. In Chapter 2 the HADES experiment and its physical goals are summarized. In the following Chapter 3 the requirements for the ECAL and its readout system are specified. In order to investigate the optimal functionality of the calorimeter modules a series of dedicated test experiments of the prototype frontend-electronics in combination with different PMT

types have been performed. An overview over the Glauber framework and the systematics specific to the Monte Carlo approach are given in Chapter 4. The following Chapter 5 is devoted to the methods of global event characterization with a special focus on event selection methods, the centrality determination and systematics in the context of identified particles.

Bibliography

[1] C. R. Allton et al. "Equation of state for two flavor QCD at nonzero chemical potential". In: *Phys. Rev. D* 68 (1 July 2003), p. 014507. DOI: 10.1103/PhysRevD.68.014507.

[2] Carl D. Anderson. "The Positive Electron". In: *Phys. Rev.* 43 (6 Mar. 1933), pp. 491–494. DOI: 10.1103/PhysRev.43.491.

[3] Carl D. Anderson and Seth H. Neddermeyer. "Cloud Chamber Observations of Cosmic Rays at 4300 Meters Elevation and Near Sea-Level". In: *Phys. Rev.* 50 (4 Aug. 1936), pp. 263–271. DOI: 10.1103/PhysRev.50.263.

[4] Carl D. Anderson and Seth H. Neddermeyer. "Positrons from Gamma-Rays". In: *Phys. Rev.* 43 (12 June 1933), pp. 1034–1034. DOI: 10.1103/PhysRev.43.1034.

[5] A. Andronic, P. Braun-Munzinger, and J. Stachel. "Thermal hadron production in relativistic nuclear collisions: The hadron mass spectrum, the horn, and the {QCD} phase transition". In: *Physics Letters B* 673.2 (2009), pp. 142 –145. ISSN: 0370-2693. DOI: 10.1016/j.physletb.2009.02.014.

[6] R. Armenteros et al. "Decay of V-Particles". In: *Nature* 167 (1951), p. 501. DOI: 10.1038/167501a0. URL: http://www.nature.com/nature/journal/v167/n4248/pdf/167501a0.pdf.

[7] F. Becattini, J. Manninen, and M. Ga ździcki. "Energy and system size dependence of chemical freeze-out in relativistic nuclear collisions". In: *Phys. Rev. C* 73 (4 Apr. 2006), p. 044905. DOI: 10.1103/PhysRevC.73.044905.

[8] P. M. S. Blackett. "The Ejection of Protons from Nitrogen Nuclei, Photographed by the Wilson Method". In: *Proceedings of the Royal Society of London A: Mathematical, Physical and Engineering Sciences* 107.742 (1925), pp. 349–360. ISSN: 0950-1207. DOI: 10.1098/rspa.1925.0029.

[9] E. D. Bloom et al. "High-Energy Inelastic $e - p$ Scattering at 6° and 10°". In: *Phys. Rev. Lett.* 23 (16 Oct. 1969), pp. 930–934. DOI: 10.1103/PhysRevLett.23.930.

[10] Szabolcs Borsanyi et al. "QCD thermodynamics on the lattice and in the Hadron Resonance Gas model". In: *Journal of Physics: Conference Series* 336.1 (2011), p. 012019. URL: http://stacks.iop.org/1742-6596/336/i=1/a=012019.

[11] Szabolcs Borsányi et al. "The QCD equation of state with dynamical quarks". English. In: *Journal of High Energy Physics* 2010.11, 77 (2010). DOI: 10.1007/JHEP11(2010)077.

[12] M. Breidenbach et al. "Observed Behavior of Highly Inelastic Electron-Proton Scattering". In: *Phys. Rev. Lett.* 23 (16 Oct. 1969), pp. 935–939. DOI: 10.1103/PhysRevLett.23.935.

[13] R. Brown et al. "Observations With Electron Sensitive Plates Exposed to Cosmic Radiation". In: *Nature* 163 (1949), p. 47. DOI: 10.1038/163047a0. URL: http://www.nature.com/nature/journal/v163/n4132/pdf/163047a0.pdf.

[14] R. Brown et al. "Observations With Electron Sensitive Plates Exposed to Cosmic Radiation - Part2". In: *Nature* 163 (1949), p. 82. DOI: 10.1038/163082a0. URL: http://www.nature.com/nature/journal/v163/n4133/pdf/163082a0.pdf.

[15] J.Z. Buchwald and A. Warwick. *Histories of the Electron: The Birth of Microphysics*. Dibner Institute Studies in the History of Science and Technology. MIT Press, 2004. ISBN: 9780262524247. URL: http://mitpress.mit.edu/sites/default/files/titles/content/9780262524247_sch_0001.pdf.

[16] N. Cabibbo and G. Parisi. "Exponential hadronic spectrum and quark liberation". In: *Physics Letters B* 59.1 (1975), pp. 67 –69. ISSN: 0370-2693. DOI: 10.1016/0370-2693(75)90158-6.

[17] J. Chadwick. "Possible Existence of a Neutron". In: *Nature* 129 (1932), p. 312. DOI: 10.1038/129312a0. URL: http://dx.doi.org/10.1038/129312a0.

[18] J. Cleymans et al. "Comparison of chemical freeze-out criteria in heavy-ion collisions". In: *Phys. Rev. C* 73 (3 Mar. 2006), p. 034905. DOI: 10.1103/PhysRevC.73.034905.

[19] G. Endrődi et al. "The QCD phase diagram at nonzero quark density". English. In: *Journal of High Energy Physics* 2011.4, 1 (2011). DOI: 10.1007/JHEP04(2011)001.

[20] Kenji Fukushima. "Hadron resonance gas and mean-field nuclear matter for baryon number fluctuations". In: *Phys. Rev. C* 91 (4 Apr. 2015), p. 044910. DOI: 10.1103/PhysRevC.91.044910.

[21] Tetyana Galatyuk. "HADES overview". In: *Nuclear Physics A* (2014), ISSN: 0375-9474. DOI: 10.1016/j.nuclphysa.2014.10.044.

[22] Eugene Gardner and C. M. G. Lattes. "Production of Mesons by the 184-Inch Berkeley Cyclotron". In: *Science* 107.2776 (1948), pp. 270–271. DOI: 10.1126/science.107.2776.270. URL: http://www.sciencemag.org/content/107/2776/270.short.

[23] M. Gell-Mann. "A schematic model of baryons and mesons". In: *Physics Letters* 8.3 (1964), pp. 214 –215. ISSN: 0031-9163. DOI: 10.1016/S0031-9163(64)92001-3.

[24] M Gell-Mann and A H Rosenfeld. "Hyperons and Heavy Mesons (Systematics and Decay)". In: *Annual Review of Nuclear Science* 7.1 (1957), pp. 407–478. DOI: 10.1146/annurev.ns.07.120157.002203.

[25] David J. Gross and Frank Wilczek. "Ultraviolet Behavior of Non-Abelian Gauge Theories". In: *Phys. Rev. Lett.* 30 (26 June 1973), pp. 1343–1346. DOI: 10.1103/PhysRevLett.30.1343.

[26] R. Hagedorn. "Statistical thermodynamics of strong interactions at high-energies". In: *Nuovo Cim.Suppl.* 3 (1965), pp. 147–186.

[27] O. Kaczmarek et al. "Phase boundary for the chiral transition in $(2+1)$-flavor QCD at small values of the chemical potential". In: *Phys. Rev. D* 83 (1 Jan. 2011), p. 014504. DOI: 10.1103/PhysRevD.83.014504.

[28] F. Karsch and K. Redlich. "Probing freeze-out conditions in heavy ion collisions with moments of charge fluctuations". In: *Physics Letters B* 695.1–4 (2011), pp. 136 –142. ISSN: 0370-2693. DOI: 10.1016/j.physletb.2010.10.046.

[29] C.M.G. Lattes et al. "Processes involving charged Mesons". In: *Nature* 159 (1947), pp. 694–697. DOI: 10.1038/159694a0. URL: http://dx.doi.org/10.1038/159694a0.

[30] K.A. Olive et al. "Review of Particle Physics". In: *Chin.Phys.* C38 (2014), p. 090001. DOI: 10.1088/1674-1137/38/9/090001.

[31] J. Pochodzalla et al. "Probing the Nuclear Liquid-Gas Phase Transition". In: *Phys. Rev. Lett.* 75 (6 Aug. 1995), pp. 1040–1043. DOI: 10.1103/PhysRevLett.75.1040.

[32] H. David Politzer. "Reliable Perturbative Results for Strong Interactions?" In: *Phys. Rev. Lett.* 30 (26 June 1973), pp. 1346–1349. DOI: 10.1103/PhysRevLett.30.1346.

[33] Cecil Powell. "Nobel Lecture: The Cosmic Radiation". In: (1964). URL: http://www.nobelprize.org/nobel_prizes/physics/laureates/1950/powell-lecture.pdf.

[34] G.D. Rochester and C.C. Butler. "Evidence for the Existence of New Unstable Elementary Particles". In: *Nature* 160 (1947), pp. 855–857. DOI: 10.1038/160855a0. URL: http://www.nature.com/nature/journal/v160/n4077/abs/160855a0.html.

[35] B. Russell. *History of Western Philosophy*. Routledge classics. Routledge, 2004. ISBN: 9780415325059. URL: http://books.google.de/books?id=Ey94E3sOMA0C.

[36] E. Rutherford. "LI. Collision of particles with light atoms I. Hydrogen". In: *Philosophical Magazine Series 6* 37.222 (1919), pp. 537–561. DOI: 10.1080/14786440608635916.

[37] E. Rutherford. "LXXIX. The scattering of and particles by matter and the structure of the atom". In: *Philosophical Magazine Series 6* 21.125 (1911), pp. 669–688. DOI: 10.1080/14786440508637080. URL: http://dx.doi.org/10.1080/14786440508637080.

[38] H.P. Schieck. *Nuclear Reactions: An Introduction*. Lecture Notes in Physics. Springer Berlin Heidelberg, 2014. ISBN: 9783642539862. DOI: 10.1007/978-3-642-53986-2. URL: https://books.google.de/books?id=Ep65BQAAQBAJ.

[39] J. J. Thomson. "XL. Cathode Rays". In: *Philosophical Magazine Series 5* 44.269 (1897), pp. 293–316. DOI: 10.1080/14786449708621070. URL: http://dx.doi.org/10.1080/14786449708621070.

[40] G Zweig. *An SU_3 model for strong interaction symmetry and its breaking; Version 1*. Tech. rep. CERN-TH-401. Geneva: CERN, Jan. 1964. URL: https://cds.cern.ch/record/352337.

The HADES Experiment

Physics program and beamtimes

Between 2002 and 2014 various experiments with different collision systems, *i.e.* in elementary and heavy-ion reactions, at beam energies of 1 - 3.5 GeV have been investigated by HADES. The complete list of experiments (without test runs) is given in table 1. The first runs with carbon-carbon reactions at 1 and 2 AGeV [2, 3, 8] were performed to confirm, with better acceptance and statistics, data which have been taken by the DLS (DiLeptonen Spektrometer) collaboration [41] at Bevalac and which showed an enhancement of low-mass dileptons in heavy-ion reactions.
The reactions p+p & d(n)+p conducted in 2006 and 2007 allows to draw conclusions on the origin of virtual photons in elementary and light collision systems, *i.e.* C+C. Cold nuclear matter at saturation density was studied in 2008 with p+Nb reactions and the elementary reference p+p at 3.5 GeV in 2007.

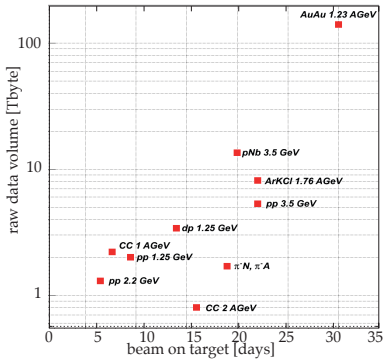

Figure 6: Compilation of all HADES production beamtimes, organized in raw recorded data volume [TByte] and length of the beam campaign [in days].

Year	System	Energy	rec. [10^9]	data [Tbyte]	Reference
2002	C+C	2 AGeV	0.25	1.2	[2]
2004	p+p	2.2 GeV	0.44	0.9	
2004	C+C	1 AGeV	0.495	1.1	[8]
2005	Ar+KCl	1.765 AGeV	0.925	8.3	[5]
2006	d(n)+p	1.25 GeV	0.85	1.9	
2007	p+p	1.25 GeV	1.70	5.3	
2007	p+p	3.5 GeV	1.18	3.1	[7]
2008	p+Nb	3.5 GeV	4.21	13.6	[6]
2012	Au+Au	1.23 AGeV	7.31	138	[26, 35]
2014	π^-+A	0.5 – 1.57 GeV	0.38	2.1	[17]
2014	π^-+p	0.5 – 1.57 GeV	1.23	6.6	[17]

Table 1: Between 2002 and 2014 several experiments with different collision systems and beam energies have been conducted with the HADES spectrometer. The number of events and the data volume recorded is shown.

The medium sized system Ar+KCl [5] was measured in 2005 and the large size system Au+Au [26, 35] in 2012 with 7.3 billion events accumulated over 5 weeks of beam time. A measurement of pion induced reactions in the momentum region $0.612 - 1.7$ GeV/c and using tungsten (^{74}W), carbon (^{12}C) and polyethylene (CH_2) as target is accomplished in 2014.

Detector & Requirements

The *High-Acceptance Dielectron Spectrometer* (HADES) is located at the *GSI Helmholtzzentrum für Schwerionenforschung GmbH* accelerator facility in Darmstadt and was developed to reconstruct in particular di-electrons from decays of the light vector mesons ρ and ω in heavy-ion beam in the energy regime of 1-2 AGeV. This physics goal puts specific constraints on the apparatus [42]:

- *High geometrical and kinematic acceptance:* to increase the statistics of the rare di-electron pairs from low mass ($\leq$ 1 GeV) vector meson decays with large opening angles.
- *Fast detectors for high rates:* allows the operation at beam intensities of up to 10^8 Hz to collect high statistics. This is necessary since the decay of vector mesons is suppressed by an additional coupling constant.
- *High granularity:* ability to cope with high particle multiplicities.
- *High momentum resolution:* a sufficient resolution in the invariant mass region of light vector mesons with $\Delta M/M \approx 1\%$ is required.
- *Low material budget:* to minimize the background from γ-conversion into di-electron pairs inside the detector and to reduce multiple scattering.
- *Lepton/Hadron identification & discrimination:* to provide a clean electron/positron sample by rejecting the hadronic background.

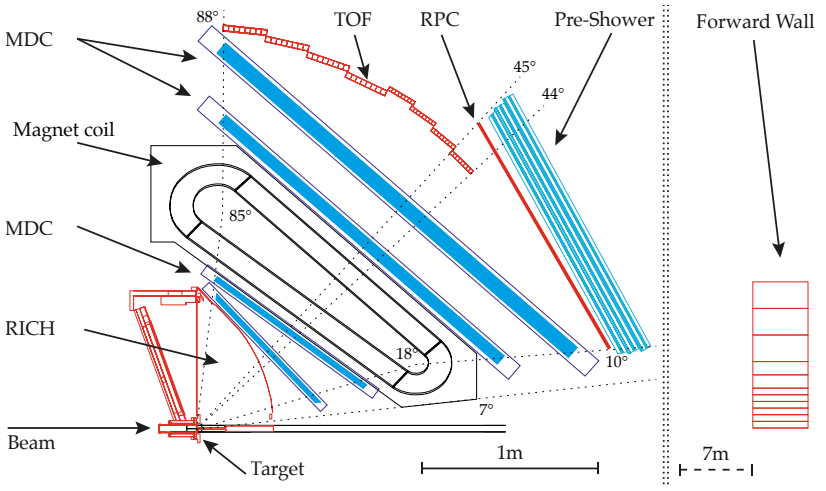

Figure 7: Cross section of one HADES sector. The segmented target irradiated by the beam, which is fully surrounded by the RICH detector. The magnet spectrometer consists of four layers of drift chambers (MDC), each two in front of and behind the toroidal magnetic field. At the end of the apparatus the *time-of-flight wall* (TOF) and the *Resistive Plate Chambers* (RPC), followed by the electromagnetic pre-shower detector, are placed. The TOF detector covers the geometrical polar angel between 44° and 88°, the RPC 10° and 45°, with an overlap of 1°. The maximal acceptance coverage in polar angle for charged particle corresponds to the coverage of magnetic field between $18° - 85°$.

The above requirements are realized by an acceptance coverage of the polar angle from 18° to 85° and in the practically whole azimuthal

angle, with six identical sectors. The resulting acceptance for low mass vector meson pairs is of the order of $\approx 40\%$ for beam energies between $1 - 2$ GeV. The momentum resolution of 1% is achieved with a spatial resolution in the MDC of $35 - 50\mu$m in polar direction and $85 - 125\mu$m in azimuthal direction. All detectors can be read out with rates of $10 - 50$ kHz depending on the particle multiplicity [36]. The spectrometer has also excellent capability for hadron identification.

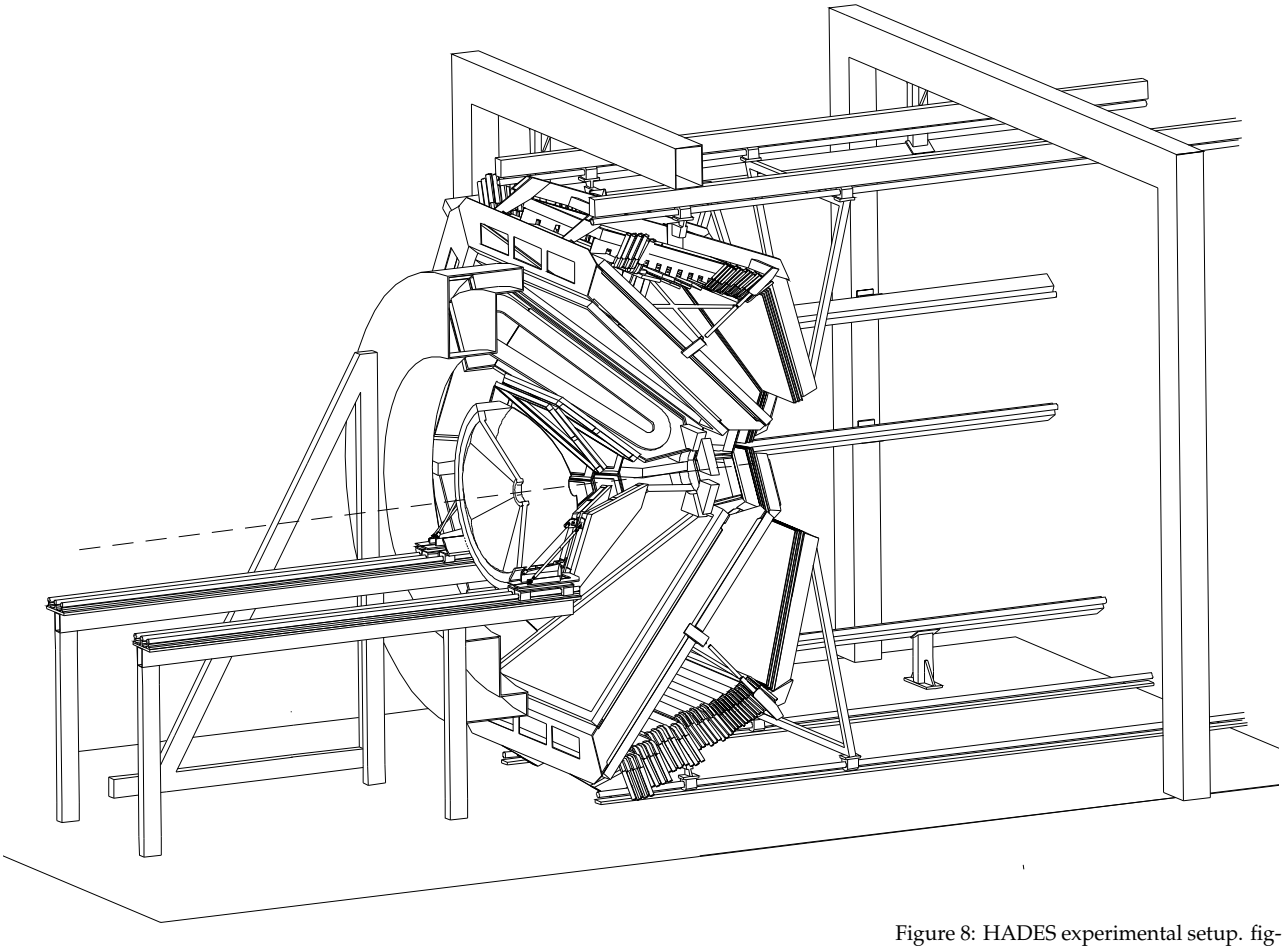

Figure 8: HADES experimental setup. figure adapted from [45]

The 6 m high hexagonal structure of the HADES spectrometer is sketched in fig. 8 and the cross section through the mid-plane of one sector in fig. 7. As beam detectors two *diamond counters* are mounted directly in front of and behind the segmented target (Start-Target-Veto). Together with the *Multiplicity and Trigger Array* (META) consisting of two time-of-flight walls, placed in the region behind the tracking system, they provide the trigger information for the *Central Trigger System* (CTS). At larger polar angles between 44° and 88° the scintillating *time-of-flight wall* (TOF), consisting in each sector 64 of scintillator bars organized in 8 modules and read out at both ends

by photomultiplier tubes. The forward region between 18° and 45° is instrumented with *Resistive Plate Chambers* (RPC), a gaseous parallel plate avalanche detector. The *Forward Wall* (FW) is placed at a distance of 7 m behind the target at the small forward angle between 0.3° and 7°. The momentum reconstruction is carried out by measuring the deflection angle of particle trajectories derived from the hit positions in 24 multiwire driftchambers, the so-called *Mini-Drift Chambers* (MDC) placed in two layers in front of and behind a toroidal magnetic field of the *superconducting magnet coils* (ILSE). For the identification of electrons and positrons the HADES setup has two dedicated detectors. The hadron-blind gas *Ring Imaging Cherenkov detector* (RICH), operating in a field-free region surrounding the segmented target and the electromagnetic shower detectors (Pre-SHOWER) at the end of the detector system.

Particle Identification

The detection of (charged) particles is based on the interactions between particles and with detector material [34]. A detector setup consisting of several specialized sub-detectors for different purposes like position measurements (tracking) used for momentum determination in a magnetic field and particle identification (PID) via their specific characteristic: mass, charge energy loss or time of flight.

- *Momentum* and *polarity* by tracking in a magnetic spectrometer and measuring the curvature of the track,
- *velocity* by time-of-flight, Cherenkov- or transition radiation,
- *specific energy loss* dE/dx due to the ionization power of the charged particle and the *total energy* measurement in calorimeter.

Photons are detectable in electromagnetic, and hadrons in hadronic calorimeter. Electrons and charged hadrons are distinguished with threshold detectors like threshold Cherenkov, Transition Radiation Detector (TRD) or electromagnetic calorimeter, as illustrated in figure 9. The combination of velocity together with momentum or energy measurement enables the determination of particle mass.

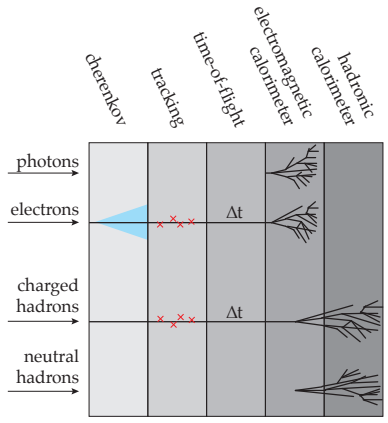

Figure 9: Particle detectors consist of several layers of specific subdetector systems with certain sensitivity to the specific characteristic of the examined particles (charge and mass, interchangeable with energy, momentum or velocity).

Physical principle of electromagnetic calorimeter

The underlying principle of calorimeters is the conservation of the energy of an incident particle, which is converted into a detector response proportional to it. A useful calorimeter for high-energy physics experiments [23] must ensure that nearly the complete energy of the impinging particle is lost to the system. In comparison with magnetic spectrometer, where the momentum resolution is linearly decreasing with the particle momentum ($\sigma_p/p \sim p$), the energy resolution of a calorimeter improves with increasing energy ($\sigma_E/E \sim 1/\sqrt{E}$). The momentum resolution of the HADES magnetic spectrometer for 1 GeV/c momentum protons (at $\theta = 23°$) is around 2% and for 3 GeV/c quoted with 4% [4]. The direct comparison for particles with an energy of 1 GeV, the aimed energy resolution for the calorimeter would be 5% and for 4 GeV around 2.5%. The other advantage of calorimeter in general is their sensitivity to charged and neutral particles. The limit for the *energy resolution* of a calorimeter is determined by fluctuations in the absorption and detection process and are commonly parameterized as following:

$$\sigma_E/E = \frac{a}{\sqrt{E}} \oplus \frac{b}{E} \oplus c \tag{2}$$

with the parameter a, b and c describing the contribution of the *stochastic term*, *noise term* and *constant term*. The fluctuations in the development of the showers and the photo-electron detection are stochastic processes and can be described by the Poisson statistic. In the measurement of the calorimeter energy we expect a *stochastic term* and its fractional error should evolve as $\sim 1/\sqrt{E}$. Additionally, there are non-stochastic contributions limiting the accuracy of the energy measurement, caused by instrumental and calibration limits. These components are due electronic noise, pedestal fluctuations, light attenuation, non-uniformity and non-linearities in photomultipliers and signal processing, and calibration errors. The convolution of these effects are often divided into an energy dependent *noise term* $\sim 1/E$ and an energy independent *constant term* $\approx const$.

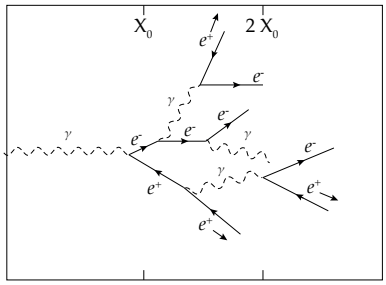

Figure 10: Schematic of an electromagnetic cascade, where a photon produces a conversion pair after one radiation length X_0 and each electron and positron emit one bremsstrahlung photon in average after another radiation length.

Electromagnetic shower

The interaction of high-energy electrons and photons with matter is driven primarily by electromagnetic (EM) interactions with the nucleus and at lower energies with the atomic electrons. A high-energy photon develops an electromagnetic shower, shown in figure 10, in a calorimeter through the multiplication of a sequential cascade of pair production from photons (fig. 12) and bremsstrahlung of electrons (fig. 11). The main feature of EM shower is described by the radiation length X_0, a characteristic depending on the material. After around one radiation

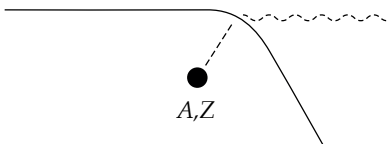

Figure 11: Bremsstrahlung produced by an electron deflected in the electric field of an atomic nucleus (Z)

length ($9/7X_0$) in average a photon produces a conversion pair and each electron and positron emit one bremsstrahlung photon after another radiation length and so on. The shower maximum will occur when the

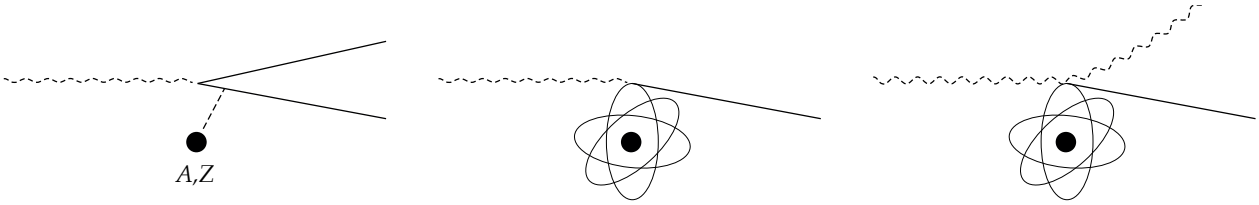

Figure 12: (left) *Pair production* by a photon creating an electron-positron pair near a nucleus (middle) *photo electric effect* by the emission of photoelectrons out of the atomic electron shell (right) and *Compton scattering* by the inelastic scattering of a photon by an electron.

energy falls below a critical energy $E_c = 620\ \text{MeV}/(Z + 1.24)$ at which ionization loss becomes equal to bremsstrahlung loss. Generally, at very low photon energies ($10 - 1000$ eV), coherent Rayleigh scattering and the photoelectric effect predominate. At low energies ($0.01 - 1.0$ MeV), Compton scattering is dominant, while above 410 MeV pair production is dominant. (see left fig. 13)

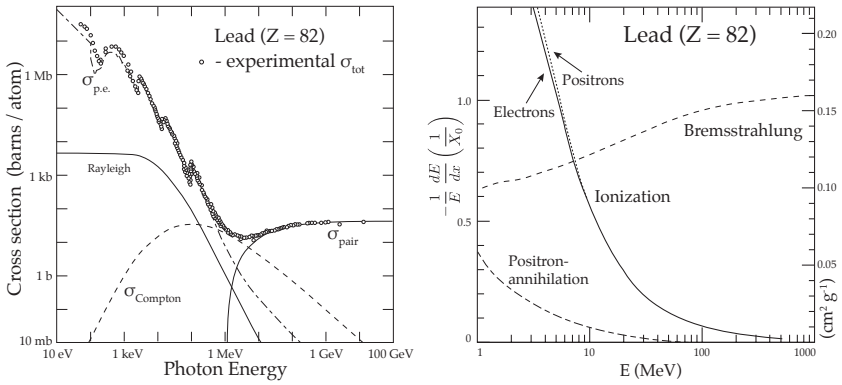

Figure 13: (left) Photon total cross sections as a function of energy in lead(right) Fractional energy loss per radiation length in lead as a function of electron or positron energy

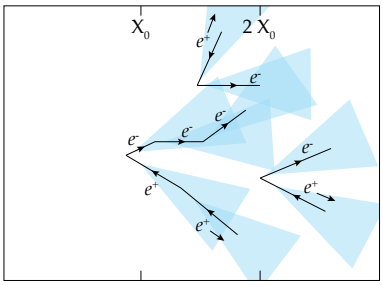

Figure 14: Cherenkov light produced by electrons and positrons of the EM shower in lead-glass

Lead-glass Cherenkov counters

Radiation detectors based on the Cherenkov effect use lead glass as the detector of choice, owing to its ability to absorb high-energy particles, high uniformity and high transmission. The Cherenkov effect itself is the photonic analogue to an acoustic shock wave: when a high-energy particle encounters a material at a velocity higher than the inherent photonic phase velocity of the material, Cherenkov radiation is emitted as an electromagnetic shock wave. The angle θ of emitted photons with respect to the initial, high-energy particle trajectory is given by:

$$\cos\theta = 1/\beta n \tag{3}$$

An very important advantage of lead-glass Cherenkov counters is that the Cherenkov radiation from charged particles provides a fast timing signal in comparison to scintillator signals.

Schwerionen-Synchrotron SIS18

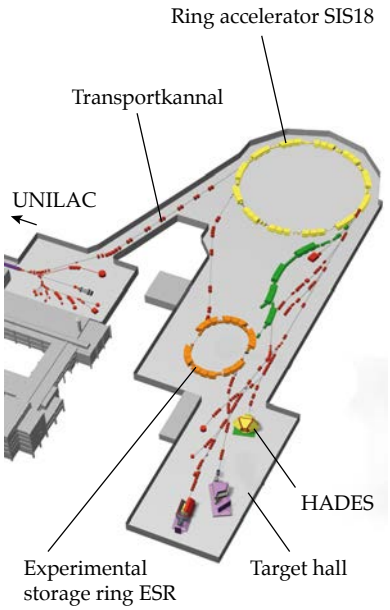

The accelerator complex, which provides beams for the HADES experiment, is located at the *GSI Helmholtzzentrum für Schwerionenforschung GmbH* facility in Darmstadt, Germany. The first section, the *Universal Linear Accelerator* (UNILAC) with the versatility to accelerate ions over a wide range of masses and charge states from protons to Uranium came under operation in 1975. The *Schwerionen-Synchrotron 18* (SIS18) - heavy ion synchrotron was built to raise the beam energy and came into operation in 1990. As the name indicates the maximum magnetic rigidity of the synchrotron is 18 Tm and the maximum energy depends on the mass-to-charge ratio of the ion and lies between 1 AGeV for U^{73+} and 4.5 GeV for protons. The beam is than extracted and transferred to the experimental areas or to the *Experimental Storage Ring* (ESR). The full process of the ion acceleration takes $\sim 1-3$ s, depending on the required ion kinetic energy. The maximal limit of SIS18 for Au^{69+} is 1.25 AGeV. By a two-step acceleration with intermediate beam cooling and stripping in the ESR and re-injection into the SIS18 an energy of 1.5 AGeV for Au^{79+} is possible, but at the cost of a limited duty cycle and beam intensity. The purpose of the UNILAC is to extract ions, pre-

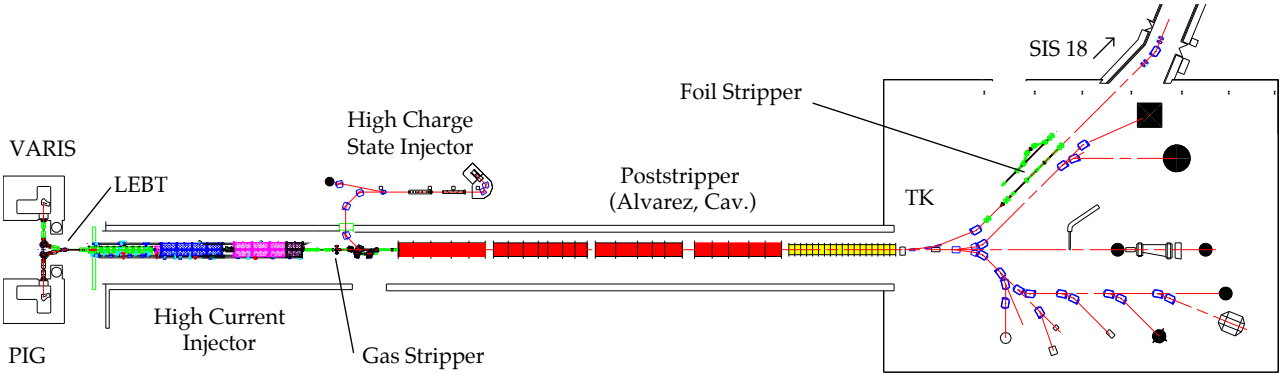

Figure 15: UNILAC: The ion source (VARIS), the Low Energy Beam Transport system (LEBT), High Current Injector with 4 Stages (RFQ, Super Lens, HI1, HI2), Gas Stripper, 4 Stages of Alvarez linear accelerators and the 150 m long Transport-Kanal(TK) to the SIS18. Image adapted from [27]

accelerate and inject them into the synchrotron. With the new installed *Vacuum ARc Ion Source* (VARIS) source a stable beam of Au^{4+} ions with currents up to 6 mA and a short conditioning time (10-20 min) [30] were achieved and it was used for the first time in 2012. An admixtures of 50% ^{197}Au and 50% of chromium ^{24}Cr [1] was used to produce a high intensity beam of the charge-state Au^{4+}. In the next step a *Low Energy Beam Transport system* (LEBT) together with a mass spectrometer for selecting appropriate isotopes is used and the beam is transported with a kinetic energy of 0.0022 AMeV to the *High Current Injector*. The ions with an energy of 1.4 AMeV at maximum are stripped by a supersonic gas jet in the gas stripper and a particular ion charge state is selected.

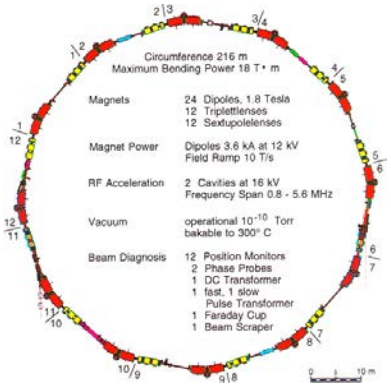

Figure 16: SIS18: 12 identical sections each with two 1.8 T dipoles(red) and one quadrupole triplet and one sextupole(yellow). Two ferrite cavities(blue) on opposite sides of the ring.

Figure 17: 15 gold foils placed on kapton strips and mounted on the target holder tube. [28]

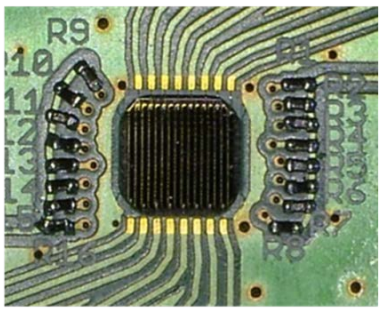

Figure 18: START diamond detector (single-crystalline Chemical Vapour Deposition) [38]

In the next stage an Alvarez linear accelerator increases the energy of the ions to 11.4 AMeV from where the beam is transported in a 150 m long *Transport-Kanal* (TK - transport canal) and injected in to the SIS18.

The SIS18 with the circumference of 216.72 m consists of 24 bending and 24 focusing magnets and two ferrite cavities. It is divided into 12 identical sections, each equipped with two 1.8 T dipoles for beam bending, one quadrupole triplet and one sextupole for beam focusing. The acceleration of the ions is realized in two ferrite cavities. Each ion at this point experiences a potential of 16 kV in a frequency range of $0.8 - 5.6$ MHz. The vacuum in the beam pipe is on the level of 1.3×10^{-7} Pa. Within the 5 weeks of beamtime the SIS18 delivered 684 hours of Au^{69+} ions beam to the HADES cave [15] with an intensity of $1.2 - 2.2 \times 10^6$ ions per second.

Segmented Target

The target is shown in figure 17 is a 15-fold segmented gold target. Each gold disk with a thickness of 25μm is glued on two points on a kapton strip with a thickness of 7μm and a hole at the area of the target disk [31]. The kapton stripes are mounted on a carbon fibre tubes with an inner diameter of 20 mm and a wall thickness of 0.5 mm. The total available length of 54.5 mm in the target holder results in a distance of 4 mm between the target disks and corresponds to an overall interaction length of 1.35%. The low Z of the carbon target holder tube and the kapton stripes together with the arrangement of the segmented gold targets ensures that the gamma-conversion probability in the target region is as low as possible.

Diamond START- and VETO-counter

The beam detector START is used for event-triggering in coincidence with the multiplicity-trigger and provides a high resolution start time (T_0) of the collision event. Together with the time-of-flight walls (TOF, RPC and FW), it is used for the time-of-flight determination. Additionally, the beam quality and luminosity is monitored.

The signal of the VETO detector can be used in anti-coincidence with the multiplicity-trigger to suppress pile-up or peripheral reactions. To achieve this goal, a radiation hard pcCVD or scCVD (poly- or single-crystalline Chemical Vapour Deposition) diamond detectors [40, 39] is used. The main properties of the detector are the highly efficient charge collection and the short signal collection time, together with a low interaction probability with beam ions achieved with a thickness of $\sim 60\mu$m [38]. The metallization of the START detector consist of a 50 nm Cr layer on a 150 nm Au layer arranged in 16 stripes with a width

200μm and 90μm gaps at each side of the diamond providing a x-y position measurement. The VETO detector, located 70 cm downstream of the target, is made of 100μm polycrystalline material and is aligned along the beam line axis.

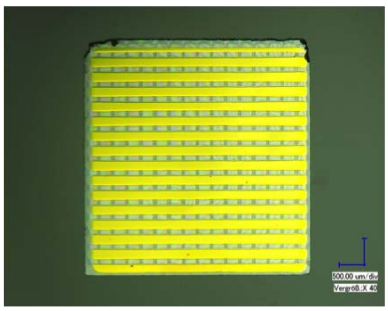

Figure 19: Active area of START diamond detector (4.39×4.39 mm^2) [38]

DAQ, Central-Trigger-System (CTS) & slow control

One of the challenges in heavy-ions experiments is the huge multiplicity per event in comparison to elementary particle experiments. The main goal of each trigger-system is the reduction of the recorded data size by the selection and enhancement of physically relevant events.

For this reason a multi-purpose electronic device with on-board data acquisition was developed at GSI, the trigger and readout board (TRB). The board provides a general read out and data transfer system, generates the trigger signal and also provides slow control access to the detectors. The communication and data transport in the network is realized with the TrbNet protocol. The *Central Trigger System* (CTS) is implemented on a dedicated AddOn board to the TRB but can also be operated in a stand-alone mode. It collects all trigger-signals from different detectors and distributes the trigger decision to all readout boards. In the Au+Au beam-time there were two Physics Trigger (PT) activated. These multiplicity-trigger were set to a threshold corresponding 5 hits (PT2) and 20 hits (PT3) in the TOF detector in coincidence with the Start-Trigger. Details on the systematics of the trigger w.r.t the centrality selection are discussed in chapter 5. The accepted data-packages from different sub-detectors are collected event-wise by eight event-builders and are written out to mass storage in the binary raw event files format, the HADES List-mode Data (HLD). The *slow control* is based on the EPICS[1] control system and includes the controlling of hardware, the recording and the monitoring of all detector parameters during data collection.

[1] Experimental Physics and Industrial Control System

Analysis Framework

The data analysis is realized within the *Hades sYstem for Data Reduction and Analysis* (HYDRA) framework, developed by the HADES collaboration. The main goal of the HYDRA framework is the on-line or off-line processing of events recorded in HADES. It is based on the ROOT class package originally developed in 1995 for the NA49 heavy-ion experiment and which since than became a standard in nuclear and particle physics. The object-oriented design allows in a very flexible way to derive detector- or task-specific classes from a common set of base classes. The data input can be taken from several data sources: directly from the event builders (via TCP/IP), from recorded HADES List-mode

Data (HLD) files or processed Data Summary Files (DST) in the various stages of analysis. The initialization of geometry, setup and calibration parameters is obtained by the HADES data base (implemented as ORACLE DB) and from ROOT files.

Experimental Data

The first level of event processing is the decoding of the binary data by the so-called *Unpacker* for each detector. The data is structured into the HYDRA classes scheme stored in the *Raw level*. The *Cal level* is reached by one or more calibration steps, where the detector readout values are translated into physical values. The *Hit level* is filled by the *Hit finder* which retrieves the information of the impact of a particle on an active area of a given detector in relative setup coordinate space. The following core-process of the framework (*Tracking*) assemble all hit information of the sub-detector and reconstructs the *Particle Candidates* on the *Track level*. From this stage the data content is no longer refined or modified, but only additional extracted physical information are added, such as the momentum, polarity, track quality, matching quality and finally particle identification properties.

Simulated Data

Simulated events are generated with event-generator based on Quantum Transport Models (BUU or UrQMD) or with thermal models (PLUTO), and provide information about the impact parameter of the reaction, and the energy and momentum of the generated particles together with their identity. The particles of each event are then *tracked* through the HADES detector by HGeant, the HADES simulation package based on Geant 3.21. The full geometry with material budget, the specific interaction cross sections with the material and an accurate magnetic field map are included. The detector response to the interaction to the detected particle is implemented in the *Digitizers* where a signal pattern is generated, mimicking the calibrated real detector readout. This information is filled in to the *Sim Cal level*, corresponding to the *Cal level* of experimental data, but in addition also contains the information to retrieve the known Monte Carlo primary source. From this stage on, the reconstruction of simulated data is treated exactly in the same way as the experimental data. The framework allows the overlay of simulated tracks onto real events for efficiency and performance investigations, a procedure which is called *embedding*.

Magnetic Spectrometer

The Magnetic Spectrometer consists of a toroidal field provided by the superconducting coils and four planes of low-mass mini-drift chambers (MDC). It allows to reconstruct the trajectories of charged particles and with the *bending radius* ρ upon the deflection in the known magnetic field B the *magnetic rigidity* $p/Z = B\rho$ is determined. There are two planes of MDC in front and two planes behind the coils of a superconducting magnet in order to reconstruct *tracklets* before and after the deflection. Furthermore, a large momentum range of $p = 0.1 - 2\,\mathrm{GeV}/c$ must be accepted simultaneously within a large solid angle. The purpose of the magnet is to provide a transverse kick to charged particles in order to obtain their momenta with sufficient resolution which is of the order of $\sigma_p/p \approx 1.5 - 2\%$ for electrons and $\sigma_p/p \approx 2 - 4\%$ protons.

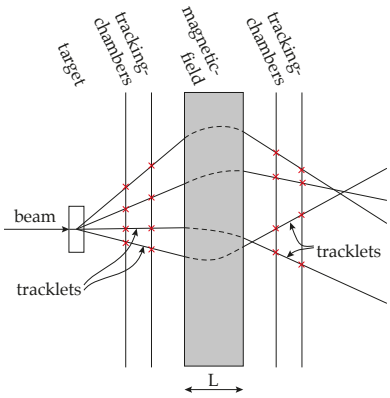

Figure 20: Principle of a magnetic spectrometer

Superconducting magnet

The superconducting toroidal magnet (ILSE) [19], shown in figure 21 consists of six superconducting coils surrounding the beam axis and produces a toroidal field which bends the particles in first approximation only in the polar direction. The magnetic field strength inside the coil corresponds to $B \approx 3.5$ T and in the HADES acceptance it reaches a maximum of ≈ 3 T and falls to a value of $0.7 - 0.9$ T between two coils.

This field geometry results is an additional deflection in azimuthal direction, especially at the borders of a sector and causes a focusing effect w.r.t. the trajectory passing through middle of a sector. The resulting momentum kick is in the order of 100 MeV/c and at smaller polar angles it is higher to achieve a good momentum resolution without losing low momenta particles [19, 44]. The maximum current in the coils amounts to $I \approx 3500$ A and the superconducting material in the coils is a niobium-titanium alloy enclosed in a copper matrix. The copper is needed for mechanical stability, and in the case the superconductivity is lost, so-called *quench*, it will drain away the large currents. The copper and niobium-titanium matrix, twisted into wires, is also inclosed again in aluminum to ensure that a sudden drop of the magnetic field will not damage the coils [19]. The coils are surrounded by a shield cooled by liquid nitrogen at 85 K and the current leads are cooled with single phase He at 2.8 bar and 4.7 K.

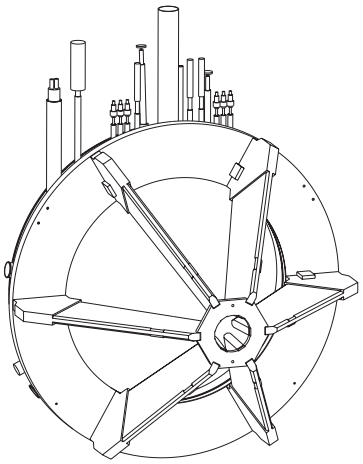

Figure 21: The superconducting magnet consisting of 6 coils, surrounding the beam axis and a circular support structure. On the upper part the power and gas supplies are connected.

Mini-Drift Chambers (MDC)

The active area of the smallest inner chambers is 0.34 m^2 and 2.83 m^2 for the outer chambers and is covering the same solid angle per sector. The smallest sensitive unit of the multi-wire drift chamber is the mini-drift cell which consist of one plane with one sense wire in the center

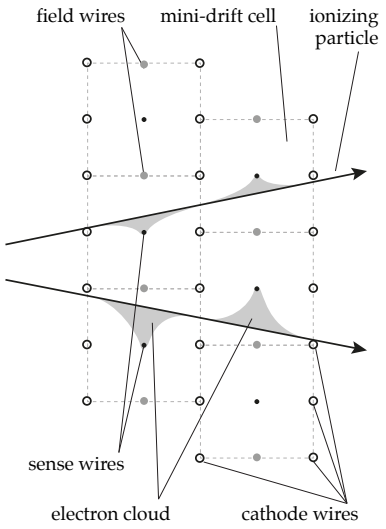

Figure 22: Sketch of a trajectory of ionizing particle reconstructed inside the MDC drift cells via the drift time of the electron cloud

of the cell and potential wires on both sides. This plane is enclosed by planes of cathode wires, see fig. 22. The cathode and potential wires are made from annealed aluminum with $80 - 100\mu$m diameter and the sense wires from gold-plated tungsten with a diameter of $20 - 30\mu$m.

Each chamber contains about 1100 of these elongated mini-drift cells organized in 6 layers with 5 different orientation angles with respect to each other ($0°, \pm 20°, \pm 40°$). This pattern ensures a homogeneous spatial resolution of $85 - 125\mu$m with respect to the azimuthal angle and enhances the spatial resolution of $35 - 50\mu$m in polar angles pointing in the direction of the momentum kick [37, 4]. The most inner chambers plane I are filled with with Ar/CO_2 (70 : 30) as counting gas and the three other chambers II-IV with argon-isobutane (84 : 16). Charged particles flying through the chamber ionize the gas and electrons and ions start drifting due to the potential difference between the field and cathode wires. On their way they can ionize other atoms and an avalanche is generated close to the sense wire which is read out. The mini-drift cells signal are read-out on the sense wires and the collected charge pulse is amplified, shaped and discriminated by a dedicated ASIC (ASD8-B) on the front-end boards. This chip provides additionally the *time-over-threshold* (ToT) of each hit. These signals are routed to TDCs where all transitions are recorded, stored and transmitted to the general read-out system TRB by Optical End-Point (OEP) based on FPGAs [36].

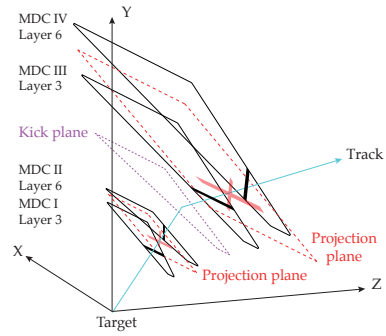

Figure 23: Principle of the track candidate search finding an inner and outer track segment. Only one MDC layer per module is shown [4].

Track reconstruction

The track reconstruction is accomplished by a spatial search of possible *track candidates* and thereafter by a precise fit to a track model function by including the distance to the sense wires [7] (see in fig. 23):

- The spatial correlation of all fired drift cells in the inner or the outer chambers are projected into virtual projection planes and the localization of the maxima in this planes are called *wire clusters*.
- The impact point of a track on the inner projection plane constructed by the *wire clusters* define together with an estimated target position a straight *track segment* (synonymous with the term *tracklet*).
- The deflection of a charged particle track by the toroidal magnetic field is approximated by a momentum kick in a virtual *kick plane* between the inner and outer chambers.
- The *wire clusters* of the outer projection plane define together with the intersection point of an inner *track segment* on the *kick plane* the resulting outer *track segment*.

- This inherent matching of inner and outer *track segments* in one sector results in *track candidates*.
- The spatial precision of the *track candidates* is improved by making use of the drift time measurement of each drift cell, which can be converted into the distance to the sense wires, based on GARFIELD simulations.
- The *track candidates* are matched with the hit points of the two META detectors TOF and RPC and for electron identification the inner *track segments* are matched with rings of the RICH detector.

Momentum determination

In the HADES analysis framework there are four different momentum reconstruction algorithms implemented. The fastest estimate is done by the *kick plane* method, but due to the limited precision of the straight-line-model, it is not used in the data production. The *spline* method utilizes a three-dimensional magnetic-field map and a cubic spline to model a smooth trajectory passing through the detector hit points. The resulting momentum estimate and particle polarity is used together with vertex and META-Hit information as the initial condition by the iterative *Runge-Kutta* method. The *Runge-Kutta* method solves the equation of motion in an known magnetic field in a recursive way. A least-square minimization estimates the parameter of the charged-particle trajectory and in addition provides the specific χ^2_{RK} as a track quality criteria. As a complementary method based on an extension of the *Kalman filter*, the Deterministic Annealing Filter is implemented [32].

Energy loss in the drift chambers

In addition to the timing-signal of each hit in the MDC cells the width of the signal in time (*time-over-threshold* ToT) is read out, which allows to reconstruct the collected charge corresponding to the deposited energy of the particle. The measured drift time depends on the gas mixture and pressure, the electric field in the cell, the cell size and also on the track geometry, in particular its minimum distance to the sense wire and its impact angle. The ToT of the drift time signal additionally depends on the threshold settings of the read-out chip (ASD8) and can be calibrated with the non-linear correlation with the particle energy loss parametrized by the formula:

$$ToT = f(dE/dx) = c_0 + c_1[\log_{10}(dE/dx + c_3)]^{c_2}, \tag{4}$$

with the parameters c_0, c_1, c_2 and c_3. Knowing the value of the momentum and the particle type from the other detectors, the energy loss of the particle can then be fitted to theoretical Bethe-Bloch formula.

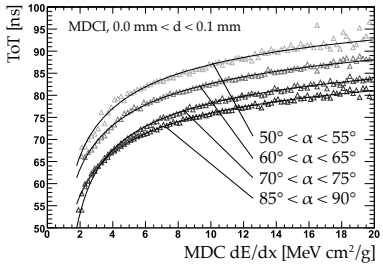

Figure 24: ToT vs. energy loss correlation from [7]

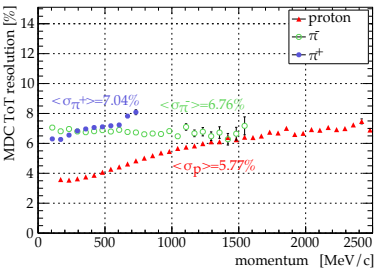

Figure 25: ToT resolution vs. particle momentum from [7]

Time of flight measurement

TOF Wall

The scintillator time of flight wall (TOF) [9] covers the polar angles between 45° and 85°. Each of the eight modules in a given sector consists of a set of eight scintillator rods, with a total of 384 rods. Each rod is made of polyvinyltoluene-based plastic scintillator *BC-408* from Bicron, which was chosen for its good light attenuation length, high scintillation light yield and short decay time. The rod cross section is 20×20 mm^2 for the innermost 192 rods and 30×30 mm^2 for the outermost 192 rods. This reflects the requirement to reduce the probability two particles hitting the same rod (double hits) to less than 10 %. By passing through the scintillating material a charged particle generate excited states in the atoms and molecules of the material, which fall back to their ground state by light emission. The theoretical energy loss dE/dx for different charged particle species can be calculated using the Bethe-Bloch formula. The differential light yield dL/dx of the scintillation can be parametrized by the empirical Birks formula, which accounts for the intrinsic non-proportional response due to the light-output degradation at high ionization density:

$$\frac{dL}{dE} = \frac{L_0}{1 + k_B \frac{dE}{dx}} \tag{5}$$

The light travels with a specific group velocity inside the rod to both ends, where it is read-out by two photomultiplier tubes EMI 9133B. Each hit produces two arrival times t_{left}, t_{right} and two amplitudes a_{left}, a_{right} of the light signal. By combining these information one can extract the time-of-flight:

$$tof = 0.5 \cdot (t_{right} + t_{left} - l/V_g), \tag{6}$$

the hit and redundant hit position:

$$x = 0.5 \cdot (t_{right} - t_{left}) \cdot V_g, \tag{7}$$

$$\hat{x} = \lambda_{at}/2 \cdot \ln(a_{left}/a_{right}), \tag{8}$$

as well the light yield (ΔL) corresponding to the deposited energy (ΔE):

$$\Delta L = k\sqrt{a_{right} a_{left} e^{l/\lambda_{at}}}, \tag{9}$$

where V_g is the group velocity of the light inside the scintillator rod, λ_{at} its light attenuation length, l the rod length. Both the time of flight and the energy loss of the particle can be used for particle identification. The short flight length of $\sim$ 2 m requires a time resolution of better than 150 ps to be able to resolve electrons from pions up to 0.5 GeV/c

and from protons up to 2 GeV/c[9]. The time resolution in Au+Au 1.23 AGeV is measured with $\sigma_{TOF} \approx 190$ ps in coincidence with the start signal and corresponds to an intrinsic resolution of $\sigma_{TOFint} \approx 150$ ps and the spatial resolution is on average $\sigma_x \leq 25 - 27$ mm, depending on rod size.

RPC Wall

The Resistive Plate Chamber (RPC) detector [16, 18] replaced the *TOFino* detector in 2008. Each of the six RPC modules has two partially overlapping layers of the individually shielded RPC cells. Each RPC cell consists of a shielding insulated with kapton, a plastic pressure object (screw) and three stacked aluminum electrodes isolated with two glass plates in between. The cell is filled with admixture of SF_6 and $C_2H_2F_4$ gas. To the electrodes a high voltage (5 kV) is supplied and when a charged particle is crossing the cell it ionizes the gas. The electrons are accelerated in the electric field towards the anode. This causes further ionization and creates an electron avalanche and a measurable electric signal. The signal is detected on both sides of the detector cell by dedicated front-end electronics. The achieved time resolution is ~ 80 ps, the hit position has a spatial resolution of better than 8 mm and an efficiency of particle hit detection of 97%.

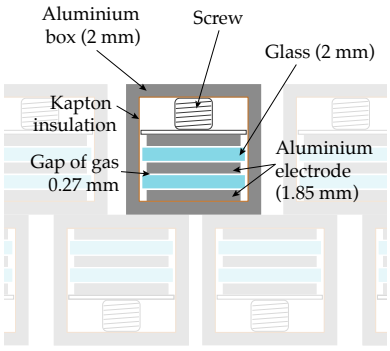

Figure 26: RPC cell

Figure 27: RPC cell with Aluminium-electrodes, glass electrodes, plastic pressure plate, kapton insulation, Aluminium-shielding tube. taken from [22]

Forward Wall

The Forward hodoscope Wall (FW) was installed 2007 [12] and is build from scintillators and photomultiplier tubes from the small-angle spectator hodoscope originally used for the Bevalac Streamer Chamber experiment [29, 21] and was also part of the TAPS [46] and KAOS experiments [43]. In May 2007 it was successfully used in the d+p experiment [33] for tagging the spectator proton to select quasi-free n+p reaction at 1.25 GeV. In the Au+Au experiment in 2012 its main purpose is the determination of the reaction plane and the centrality by measuring the reaction spectators.

The FW is positioned ≈ 7 m downstream of the target. In the area between HADES and the FW a helium-ballon is installed to reduce multiple scattering of the spectators. The 288-element array covers an active area of 1.8×1.8 m^2, corresponding to an polar angular range of $0.3° < \theta < 7.3°$. Most of the particles emitted to this angular range are spectator nucleons and fragments. An estimation for the maximal θ angle for spectator nucleons with $\approx 7°$ can be calculated with:

$$\tan\theta_{lab}^{max} = \frac{\beta_{fermi}}{\gamma\sqrt{\beta^2 - \beta_{fermi}^2}} = \frac{p_{fermi}}{p_{beam}} \tag{10}$$

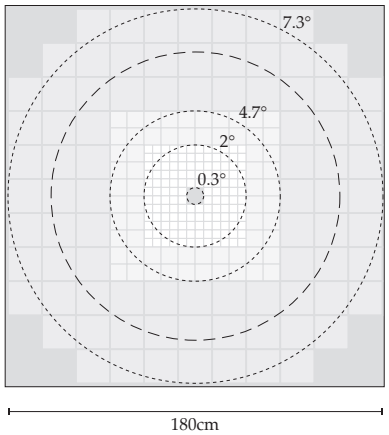

Figure 28: Forward hodoscope Wall

The support structure of the magnet coils shadows a region between 7° at the lower edge and 18° where the magnetic kick plane starts. To match the increasing spectator multiplicity at smaller angles the granularity of the detector cells size varies according to the expected particle flux: a 8×8 cm beam hole in the center, 140 small cells (4×4 cm) near the beam axis, 64 mid-size cells (8×8 cm) and 84 large cells (16×16 cm) on the border of the detector (see fig. 28). The cells thickness is 2.54 cm (1Zoll) and consists of the plastic-scintillator BC408 [43] also used for the TOF detector[2].

This detector system provides information on the position, charge, and time of flight. The projectile spectators are identified by the ΔE signal in the scintillator modules and by their time of flight. The position information of the identified spectators is used to reconstruct the event plane. Protons with the kinetic energy of 1 GeV lose an energy of ~ 5 MeV when they transverse the scintillator. The estimated time resolution of the FW in the 2012 Au+Au beam-time is $\sigma_{tof} = 400 - 500$ ps, thus the estimated momentum resolution of the detected particles (protons) is about 11%.

[2] in contrary some reference [20] quoting NE 110 as scintillator material

Electron and Hadron separation

RICH

The *Ring Imaging Cherenkov* (RICH) detector is a hadron-blind gas detector designed to identify electrons and positrons with momenta larger than 100 MeV/c. The Cherenkov light cone emitted along the particle trajectory in the radiator volume is reflected by a low mass spherical mirror ($R = 872$ mm) trough a CaF_2 window of 5 mm thickness onto the photosensitive vacuum-metallized CsI cathodes of six multi-wire proportional chambers (MWPC), operated with pure methane CH_4, shown in figure 29 and magnified in 30.

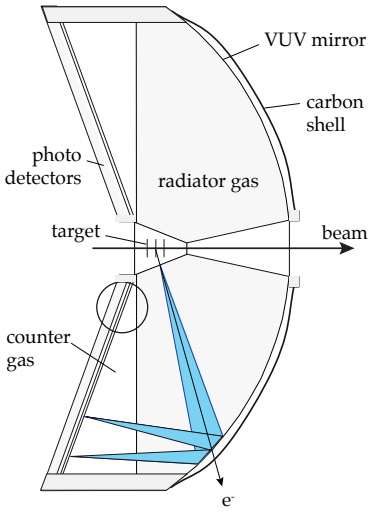

Figure 29: Schematic view of the RICH detector: An electron emits a light cone (blue), reflected by a spherical mirror to the photon detector at backward angles.

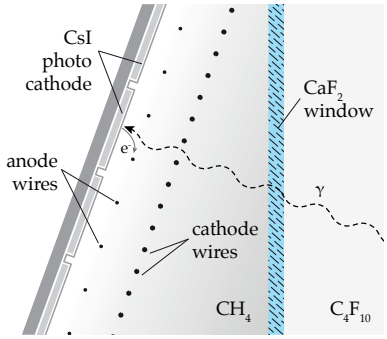

Figure 30: Magnified view with the radiator gas C_4F_{10}, the CaF_2 window, the CH_4 counting gas, the MWPC wire and the photosensitive CsI cathodes

Cherenkov radiation propagates with a characteristic emission angle depending on the velocity of the particle and the refractive index of the medium:

$$\cos\theta_c = \frac{1}{n(\lambda)\beta} \tag{11}$$

Cherenkov radiation is only emitted for the condition $|\cos\theta_c| \geq 1$ which results [34] in the threshold velocity

$$\beta_t = 1/n \text{ and } \gamma_{th} = 1/\sqrt{1 - \frac{1}{n^2}}\,. \tag{12}$$

The refractive index in general varies with the photon wavelength (chromatic dispersion) and can be parametrized by the Sellmeier ap-

proximation for the radiator gas perfluorobutane (C_4F_{10}) [10, 24]:

$$n = 1 + \frac{A}{\lambda_0^{-2} - \lambda^{-2}} \tag{13}$$

with $A = 0.2375 \times 10^{-6}$ and $\lambda_0 = 73.63$ nm and shown with the corresponding Cherenkov threshold in table 2.

The radiator gas is chosen such to maximize the transparency for UV photons down to $\lambda \geq 145$ nm with a minimum of scintillation.

λ	refractive index n	γ_{th}
145 nm	1.001734	17.0
210 nm	1.001468	18.5

Table 2: The refractive index for C_4F_{10} at 145 nm (absorption threshold) and 210 nm (detection limit of the photo detector) and the corresponding Cherenkov threshold.

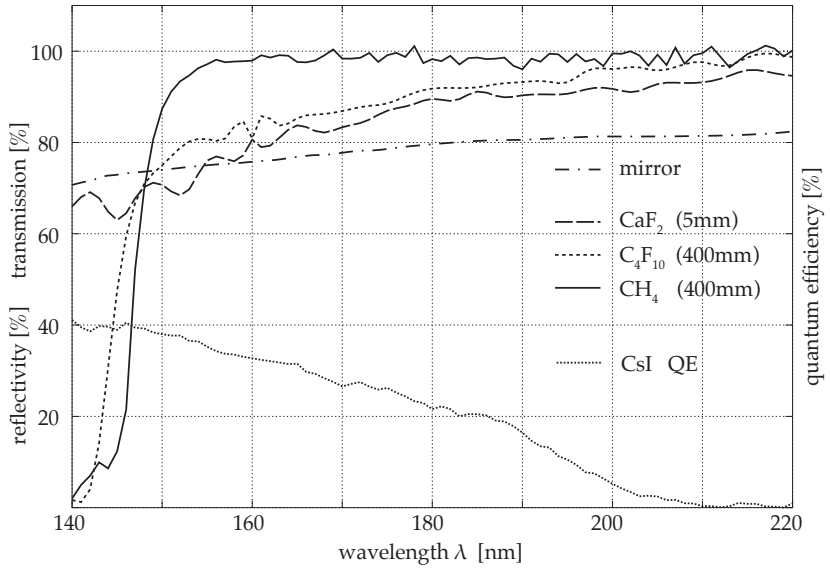

Figure 31: Optical parameters of the different RICH detector components: measured transmissions of the radiator gas C_4F_{10}, the counting gas CH_4, the CaF_2 window and the CsI photocathode quantum efficiency (Q.E.) [47] together with the mirror reflectivity in 2001 [25].

Pre-Shower

Together with the RICH detector, the second sub-detector for the dedicated lepton identification is the Pre-Shower located behind the RPC. It uses the electromagnetic cascade of electrons for their detection, which is more efficient at higher momenta. Each of the six sector modules consists of three trapezoidal wire chambers: one pre-chamber and two post-chamber, separated by lead converter plates with a length of 2 and 1.5 times the radiation length of lead ($X_0 = 0.56$ cm) [14].

A charged particle passing through the gas chambers is registered by measuring the induced charge on the cathode pads. In the case that a particle develops an electromagnetic shower a comparison of the integrated charges from the different layers would show an increase from chamber to chamber. The wire chambers are filled with an isobutane-based gas mixture and operated in the limited self-quenching streamer (SQS) mode to exclude the contributions from non-minimum ionizing protons [11, 13]. In this mode the collected charge is rather proportional to the number of particles propagating throw the chamber than to their specific energy loss.

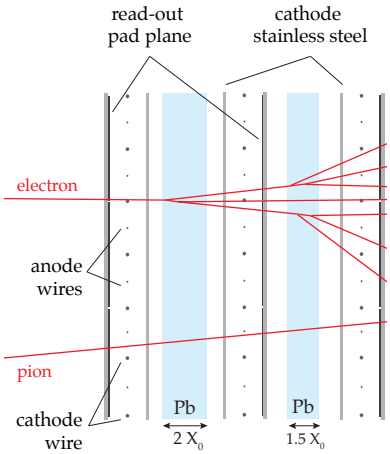

Figure 32: Cross section of a Pre-Shower cell consisting of 3 wire chambers and 2 Pb converters. While leptons generate an electromagnetic shower, the effect is suppressed for hadrons.

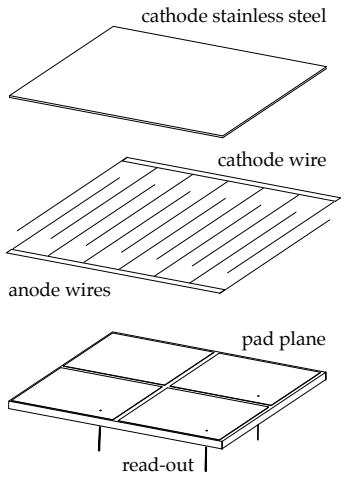

Figure 33: Configuration of one wire chamber with anode and cathode wire, 4 read-out pads and the cathode plate

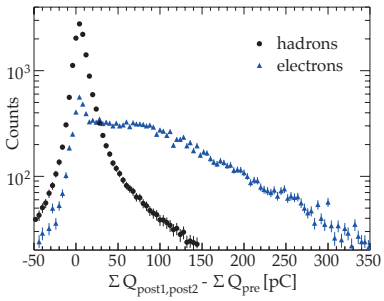

Figure 34: Sum of charge ΣQ, measured by the post-chambers and subtracted with the pre-chamber measurement. Electrons with momenta $p \sim 0.5$ GeV/c (triangles) produce electromagnetic cascades in the Pb converters which results in a larger charge deposit compared to the one from hadrons, here π^- (dots).

The charge measurement is performed as follows:

- finding a local maximum of the charge distribution in the pre-chamber (reference position)
- integrating the charge over 3×3 pads around the local maximum in the pre-chamber (Σ_{pre}), first post-chamber (Σ_{post1}) and second post-chamber (Σ_{post2})
- ratios among these integrated charges allow two methods of hadron-discrimination by applying suitable threshold values:

$$\frac{\Sigma_{post1}}{\Sigma_{pre}} \geq T_{S1}(p) \quad or \quad \frac{\Sigma_{post2}}{\Sigma_{pre}} \geq T_{S2}(p), \tag{14}$$

$$\Sigma_{post1} + \Sigma_{post2} - \Sigma_{pre}(p) \geq T_{SD}(p). \tag{15}$$

The thresholds $T_{S1}(p), T_{S2}(p)$ and $T_{SD}(p)$ for both algorithms evolve as a function of momentum and have been optimized by simulation for high electron efficiency (≥ 80 %) and hadron suppression over a broad momentum range (0.1 GeV/$c \leq p \leq$ 1.5 GeV/c).

To improve the particle identification and also include photon detection, it is foreseen to replace the Pre-Shower detector by an Electromagnetic Calorimeter (ECAL). The development, testing and commissioning of the ECAL detector including the proposed readout system for the HADES experiment at SIS18 and SIS100 is described in Chapter 3.

Bibliography

[1] A. Adonin and R. Hollinger. "*R&D* Projects with High Current Ion Sources". In: vol. 2013-1. Darmstadt: GSI Helmholtzzentrum für Schwerionenforschung, 2013, 265 p. URL: http://repository.gsi.de/record/52160.

[2] G. Agakichiev et al. "Dielectron Production in C12+C12 Collisions at 2A GeV with the HADES Spectrometer". In: *Phys. Rev. Lett.* 98 (5 Feb. 2007), p. 052302. DOI: 10.1103/PhysRevLett.98.052302.

[3] G. Agakichiev et al. "Origin of the low-mass electron pair excess in light nucleus–nucleus collisions". In: *Physics Letters B* 690.2 (2010), pp. 118 –122. ISSN: 0370-2693. DOI: http://dx.doi.org/10.1016/j.physletb.2010.05.010.

[4] G. Agakichiev et al. "The high-acceptance dielectron spectrometer HADES". In: *The European Physical Journal A* 41.2 (2009), pp. 243–277. ISSN: 1434-6001. DOI: 10.1140/epja/i2009-10807-5.

[5] G Agakishiev et al. "Dielectron production in Ar + KCl collisions at 1.76A GeV". In: *Phys. Rev. C* 84 (1 July 2011), p. 014902. DOI: 10.1103/PhysRevC.84.014902.

[6] G. Agakishiev et al. "First measurement of proton-induced low-momentum dielectron radiation off cold nuclear matter". In: *Physics Letters B* 715.4–5 (2012), pp. 304 –309. ISSN: 0370-2693. DOI: 10.1016/j.physletb.2012.08.004.

[7] G. Agakishiev et al. "Inclusive dielectron spectra in p+p collisions at 3.5 GeV kinetic beam energy". In: *The European Physical Journal A* 48.5, 64 (2012). ISSN: 1434-6001. DOI: 10.1140/epja/i2012-12064-y.

[8] G. Agakishiev et al. "Study of dielectron production in collisions at". In: *Physics Letters B* 663.1–2 (2008), pp. 43 –48. ISSN: 0370-2693. DOI: 10.1016/j.physletb.2008.03.062.

[9] C. Agodi et al. "The HADES time-of-flight wall". In: *Nuclear Instruments and Methods in Physics Research Section A: Accelerators, Spectrometers, Detectors and Associated Equipment* 492.1–2 (2002), pp. 14 –25. ISSN: 0168-9002. DOI: 10.1016/S0168-9002(02)01004-5.

[10] E. Albrecht et al. "VUV absorbing vapours in n-perfluorocarbons". In: *Nuclear Instruments and Methods in Physics Research Section A: Accelerators, Spectrometers, Detectors and Associated Equipment* 510.3 (2003), pp. 262 –272. ISSN: 0168-9002. DOI: 10.1016/S0168-9002(03)01867-9.

[11] G.D. Alekseev et al. "Investigation of self-quenching streamer discharge in a wire chamber". In: *Nuclear Instruments and Methods* 177.2–3 (1980), pp. 385 –397. ISSN: 0029-554X. DOI: 10.1016/0029-554X(80)90049-X.

[12] O.V. Andreeva et al. "Forward scintillation hodoscope for nuclear fragment detection at the high acceptance dielectron spectrometer (HADES) setup". In: *Instruments and Experimental Techniques* 57.2 (2014), pp. 103–119. ISSN: 0020-4412. DOI: 10.1134/S0020441214020146.

[13] M. Atac, A.V. Tollestrup, and D. Potter. "Self-quenching streamers". In: *Nuclear Instruments and Methods in Physics Research* 200.2–3 (1982), pp. 345 –354. ISSN: 0167-5087. DOI: 10.1016/0167-5087(82)90453-7.

[14] A. Bałanda et al. "The HADES Pre-Shower detector". In: *Nuclear Instruments and Methods in Physics Research Section A: Accelerators, Spectrometers, Detectors and Associated Equipment* 531.3 (2004), pp. 445 –458. ISSN: 0168-9002. DOI: 10.1016/j.nima.2004.05.082.

[15] W. Bayer, U. Scheeler, and Petra Schütt. "Accelerator Operation Report". In: vol. 2013-1. Darmstadt: GSI Helmholtzzentrum für Schwerionenforschung, 2013, 255–p. URL: http://repository.gsi.de/record/52152.

[16] D. Belver et al. "The HADES RPC inner TOF wall". In: *Nuclear Instruments and Methods in Physics Research Section A: Accelerators, Spectrometers, Detectors and Associated Equipment* 602.3 (2009). Proceedings of the 9th International Workshop on Resistive Plate Chambers and Related Detectors RPC08, pp. 687 –690. ISSN: 0168-9002. DOI: 10.1016/j.nima.2008.12.090.

[17] J. Biernat et al. "a secondary pion beam for the hades experiment". In: (2013). URL: http://www.e12.ph.tum.de/~rlalik/HADES_Cerberos_TDR.pdf.

[18] A. Blanco et al. "In-beam measurements of the HADES-TOF RPC wall". In: *Nuclear Instruments and Methods in Physics Research Section A: Accelerators, Spectrometers, Detectors and Associated Equipment* 602.3 (2009). Proceedings of the 9th International Workshop on Resistive Plate Chambers and Related Detectors RPC08, pp. 691 –695. ISSN: 0168-9002. DOI: 10.1016/j.nima.2008.12.091.

[19] T. Bretz. "Magnetfeldeigenschaften des Spektrometers HADES". Master thesis. Technische Universität München, 1999.

[20] D. Brill. "Azimutal anisotrope Teilchenemission in relativistischen Schwerionenstössen". Dissertation. Goethe-Universitaet Frankfurt, 1993.

[21] R. Brockmann et al. *GSI Scientific Report 1983 [GSI Report 1984-1]*. Darmstadt: GSI, 1984, p. 241. URL: http://repository.gsi.de/record/53548.

[22] P. Cabanelas et al. "Performances of multi-gap timing RPCs for relativistic ions in the range Z=1-6". In: *JINST* 4 (2009), P11007. DOI: 10.1088/1748-0221/4/11/P11007. arXiv:0905.0682 [nucl-ex].

[23] Christian W. Fabjan and Fabiola Gianotti. "Calorimetry for particle physics". In: *Rev. Mod. Phys.* 75 (4 Oct. 2003), pp. 1243–1286. DOI: 10.1103/RevModPhys.75.1243.

[24] T.A Filippas et al. "Precision measurements of gas refractivity by means of a Fabry–Perot interferometer illustrated by the monitoring of radiator refractivity in the DELPHI RICH detectors". In: *Nuclear Instruments and Methods in Physics Research Section B: Beam Interactions with Materials and Atoms* 196.3–4 (2002), pp. 340 –348. ISSN: 0168-583X. DOI: 10.1016/S0168-583X(02)01291-0.

[25] J. Friese et al. "A new carbon based VUV mirror of high radiation length for the HADES RICH". In: *Nuclear Instruments and Methods in Physics Research Section A: Accelerators, Spectrometers, Detectors and Associated Equipment* 502.1 (2003), pp. 241 –245. ISSN: 0168-9002. DOI: 10.1016/S0168-9002(03)00281-X.

[26] Tetyana Galatyuk. "HADES overview". In: *Nuclear Physics A* (2014), ISSN: 0375-9474. DOI: 10.1016/j.nuclphysa.2014.10.044.

[27] J. Glatz et al. "Operational aspects of the high current upgrade at the UNILAC". In: *eConf* C000821 (2000), MOD12. arXiv:physics/0008110 [physics.acc-ph].

[28] G. Otto / GSI. "Foto: HADES Gold Targets". In: (). URL: https://www.gsi.de/forschungbeschleuniger/forschung_ein_ueberblick/hades_experiment/aufbau_des_hades_experiments.htm.

[29] J. W. Harris et al. "Pion production in high-energy nucleus-nucleus collisions". In: *Phys. Rev. Lett.* 58 (5 Feb. 1987), pp. 463–466. DOI: 10.1103/PhysRevLett.58.463.

[30] R. Hollinger, K. Tinschert, Pfister, et al. "Ion Source Operation at the GSI Accelerator Facility". In: vol. 2013-1. Darmstadt: GSI Helmholtzzentrum für Schwerionenforschung, 2013, 257–p. URL: http://repository.gsi.de/record/52153.

[31] Birgit Kindler et al. "Targets for the electron–positron pair spectrometer HADES". In: *Nuclear Instruments and Methods in Physics Research Section A: Accelerators, Spectrometers, Detectors and Associated Equipment* 655.1 (2011), pp. 95 –99. ISSN: 0168-9002. DOI: 10.1016/j.nima.2011.06.029.

[32] Erik Krebs. "Application of a Kalman filter and a Deterministic Annealing filter for track reconstruction in the HADES experiment". Diploma thesis. Goethe-Universität,Frankfurt am Main, 2012.

[33] K.O. Lapidus. "Investigation of the production of electron-positron pairs in nucleon-nucleon interactions with the HADES detector". In: *Physics of Atomic Nuclei* 73.6 (2010), pp. 985–987. ISSN: 1063-7788. DOI: 10.1134/S1063778810060128.

[34] Christian Lippmann. "Particle identification". In: *Nuclear Instruments and Methods in Physics Research Section A: Accelerators, Spectrometers, Detectors and Associated Equipment* 666 (2012). Advanced Instrumentation, pp. 148 –172. ISSN: 0168-9002. DOI: 10.1016/j.nima.2011.03.009.

[35] M. Lorenz. "Reviewing hadron production at SIS energies featuring the new HADES data". In: *Nuclear Physics A* (2014), ISSN: 0375-9474. DOI: 10.1016/j.nuclphysa.2014.09.035.

[36] Jan Michel. "Development and Implementation of a New Trigger and Data Acquisition System for the HADES Detector". Dissertation. Johann Wolfgang Goethe-Universität Frankfurt am Main, 2012.

[37] C. Müntz et al. "The HADES tracking system". In: *Nuclear Instruments and Methods in Physics Research Section A: Accelerators, Spectrometers, Detectors and Associated Equipment* 535.1–2 (2004). Proceedings of the 10th International Vienna Conference on Instrumentation, pp. 242 –246. ISSN: 0168-9002. DOI: 10.1016/j.nima.2004.07.232.

[38] J. Pietraszko. "Beam detectors in Au+Au run and future developments". In: (2013). URL: https://indico.gsi.de/materialDisplay.py?contribId=9&sessionId=4&materialId=slides&confId=2142.

[39] J. Pietraszko et al. "Diamonds as timing detectors for minimum-ionizing particles: The HADES proton-beam monitor and START signal detectors for time of flight measurements". In: *Nuclear Instruments and Methods in Physics Research Section A: Accelerators, Spectrometers, Detectors and Associated Equipment* 618.1–3 (2010), pp. 121 –123. ISSN: 0168-9002. DOI: 10.1016/j.nima.2010.02.113.

[40] J. Pietraszko et al. "Radiation damage in single crystal CVD diamond material investigated with a high current relativistic 197Au beam". In: *Nuclear Instruments and Methods in Physics Research Section A: Accelerators, Spectrometers, Detectors and Associated Equipment* 763 (2014), pp. 1 –5. ISSN: 0168-9002. DOI: 10.1016/j.nima.2014.06.006.

[41] R. J. Porter et al. "Dielectron Cross Section Measurements in Nucleus-Nucleus Reactions at 1.0*A* GeV". In: *Phys. Rev. Lett.* 79 (7 Aug. 1997), pp. 1229–1232. DOI: 10.1103/PhysRevLett.79.1229.

[42] P. Salabura et al. "HADES — A High Acceptance DiElectron Spectrometer". In: *Nuclear Physics B - Proceedings Supplements* 44.1–3 (1995), pp. 701 –707. ISSN: 0920-5632. DOI: 10.1016/S0920-5632(95)80106-5.

[43] P. Senger et al. "The kaon spectrometer at SIS". In: *Nuclear Instruments and Methods in Physics Research Section A: Accelerators, Spectrometers, Detectors and Associated Equipment* 327.2–3 (1993), pp. 393 –411. ISSN: 0168-9002. DOI: 10.1016/0168-9002(93)90706-N.

[44] Alberica Toia. "Performance of the HADES Spectrometer for Dilepton Identification in the Reaction C+C at 1-2 AGeV". Dissertation. Justus Liebig Universität Giessen, 2004.

[45] D. Schüll W. Koenig U. Kopf. "Specification of the HADES Superconducting Torus System". In: (1995). URL: http://web-docs.gsi.de/~webhades/docs/magnet/magspec.ps.gz.

[46] A. R. Wolf et al. "Multistep Production of η and Hard π^0 Mesons in Subthreshold Au-Au Collisions". In: *Phys. Rev. Lett.* 80 (24 June 1998), pp. 5281–5284. DOI: 10.1103/PhysRevLett.80.5281.

[47] K. Zeitelhack et al. "The HADES RICH detector". In: *Nuclear Instruments and Methods in Physics Research Section A: Accelerators, Spectrometers, Detectors and Associated Equipment* 433.1–2 (1999), pp. 201 –206. ISSN: 0168-9002. DOI: 10.1016/S0168-9002(99)00371-X.

Electromagnetic Calorimeter for HADES

At the planned Facility for Antiproton and Ion Research (FAIR), the HADES spectrometer will be placed in front of the Compressed Baryonic Matter (CBM) experiment, to continue its physics program at collision energies from 2 to 11 AGeV. The electromagnetic calorimeter (ECAL) will enhance the experimental scope of the HADES spectrometer by the possibility to measure inclusive photons as well as gamma pairs from neutral meson decays (π^0 and η). Also ω vector mesons can be reconstructed via their decay channel $\pi^0\gamma \rightarrow \gamma\gamma\gamma$.

The combination of photons detected in the ECAL with charged particles reconstructed in the rest of the HADES spectrometer enables furthermore the investigation of the decays of neutral mesons and neutral hyperons and resonances, like $\Lambda(1405)$ and $\Sigma(1385)$, in elementary and heavy-ion reactions. A precise knowledge of meson production cross-sections in heavy-ion reactions at this high baryon densities will allow a further interpretation of dilepton spectra and might reveal access to other possible non-trivial sources of dileptons and enables comparison to models.

The total active area of the ECAL amounts to around 8.3 m^2 and covers polar angles between 12° and 45° with almost full azimuthal coverage [15]. The calorimeter will consist of 978 modules divided into six trapezoidal sectors with a total weight of about 15 tons and is mounted on a movable support structure, shown in figure 35). Each module will be based on lead-glass and a brass case recycled from the OPAL End-Cap calorimeter at CERN [3] assembled with photomultiplier (PMT) and high voltage-divider in a housing construction.

The established method of real gamma reconstruction via electron-positron pairs produced in external conversions in the detector material [2, 11] could be used as reference for inter-calibration by the combination of one conversion gamma with one gamma measured in the ECAL to reconstruct π^0.

Meson	Decay mode	Fraction
	Neutral modes	
π^0	2γ	98.8%
η	2γ	39.3%
ω	$\pi^0\gamma \rightarrow 3\gamma$	8.28%
	Charge modes	
η	$\pi^0\pi^+\pi^-$	22.7%
ω	$\pi^0\pi^+\pi^-$	89.2%
ω	$\pi^0 e^+ e^-$	7.7×10^{-4}

Table 3: Branching ratio decay of neutral mesons [22]

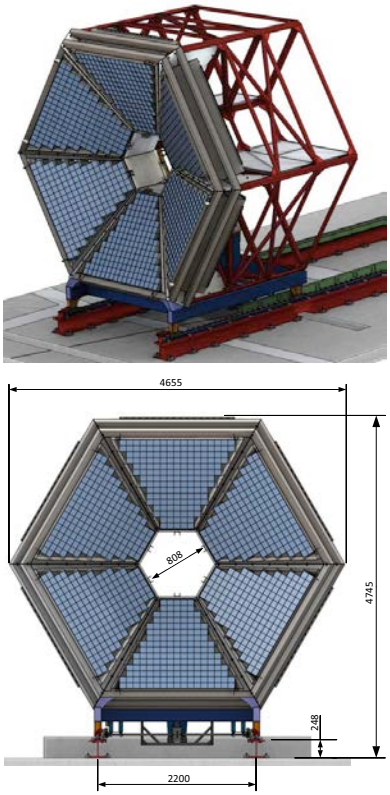

Figure 35: ECAL mechanical structure [15]

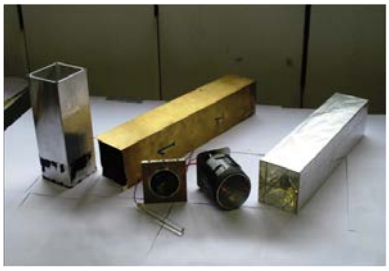

Figure 36: OPAL end cap electromagnetic calorimeter modules dissembled [3]

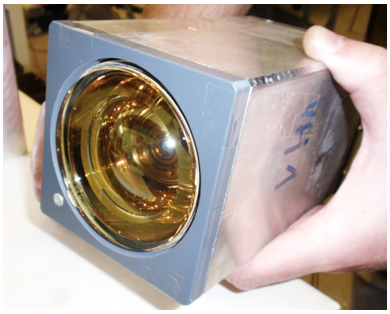

Figure 37: Housing case for the Hamamatsu 3″PMT with plastic spacer and optical connector

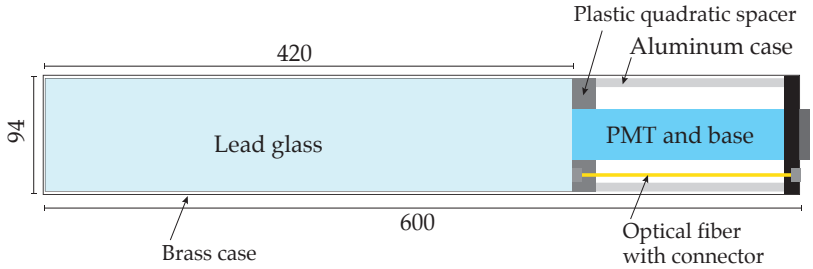

Figure 38: OPAL module with Brass case, Lead-glass, Plastic spacer, Aluminum case with the PMT and Optical fiber with connector.

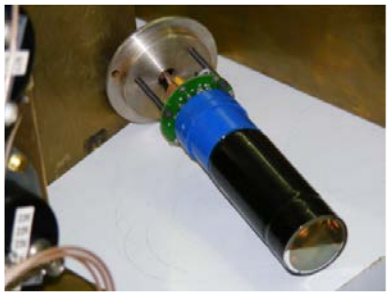

Figure 39: EMI 9903B

Module Properties

From the disassembled OPAL modules the brass container with a wall thickness of 0.45 mm and the lead-glass block are reused. To enhance the reflectivity of the lead-glass the cleaned and polished glass is wrapped within Tyvek 1060B paper containing a so called *UV stabilizer*. It was shown [24, 25] that *UV stabilized* Tyvek paper can enhance the light reflection efficiency ($80 - 90\%$) in comparison to aluminium (60%) or mylar (20%) foil.

For each of the PMT a special housing is produced including a plastic spacer between the lead-glass block and the aluminium case and an integrated optical fiber with a connector. The optical fiber, a CeramOptec multimode type with a direct optical contact with the glass on one side and a standard light connector (LC type) on the back side of the module, will be used for monitoring and calibration purposes. A light distribution system based on blue LED light sources with a pulse generating circuit is being developed. To emulating a realistic PMT-response in the lead-glass an flexible implementation on FPGA is chosen. Additionally the stability of the LED-light can be controlled hereby with an external APD-readout. This concept can be easily integrated in the general readout scheme of the ECAL based on the TRB. For the high voltage power supply the CAEN SY1527LC HV system based on the 24 channels A1535 modules providing voltage up to 3.5 kV and current up to 3 mA is foreseen.

Photomultiplier

EMI 9903B [6] is a 1.5″, ten stages green-extended tube with rubidium bialkali (RbCs) photo-cathode and BeCu dynodes with a low gain 0.2×10^6 but with extended linearity (better than 1% up to 50 mA) and a high short and long term gain stability. Two thirds of the calorimeter (~ 600) will use the 1.5″EMI 9903B photomultipliers from the MIRAC detector (WA80 and WA98) [8], which passed the tests with a small size Na(Tl) scintillator and a radioactive source [28].

Hamamatsu R6091 is a 3″, twelve stage tube with bialkali photo-cathode and a high gain of 5×10^6 with a pulse linearity of 2% up to 40 mA and 5% up to 60 mA. A better pulse linearity of 2% up to 80 mA can be achieved with a *Tapered High Voltage Divider* with the cost of reduced anode output of $30 - 50\%$ which has to be adjusted with higher supply voltage [18]. Self-developed high voltage dividers were designed and tested. They show comparable results to the original Hamamatsu HV dividers.
Hamamatsu R8619 is a 1″, ten stages PMT with a gain of 2.6×10^6 and a pulse linearity of $\pm 2\%$ up to 5 mA which is tested as a cost efficient solution.

Figure 40: Hamamatsu R6091

Figure 41: Hamamatsu R8619

	HM3 R6091	HM1 R8619	EMI1.5 9903KB
Active diameter [mm]	65	22	32
Active area [cm^2]	33.1	3.8	8.0
Quantum efficiency at peak [%]	26	29	28
Wavelength at maximum QE	390	390	–
Spectral range [nm]	$300 - 650$	$300 - 650$	$290 - 680$

Lead-glass

Lead-glass CEREN 25 is used as a Cherenkov radiator, with a density of 4.06 g/cm^3, a refractive index of 1.708 (at 410 nm), a radiation length (X_0) of 2.51 cm and a Moliere radius of 3.6 cm. The properties of lead-glass CEREN 25 or SF5 are summarized in the following table:

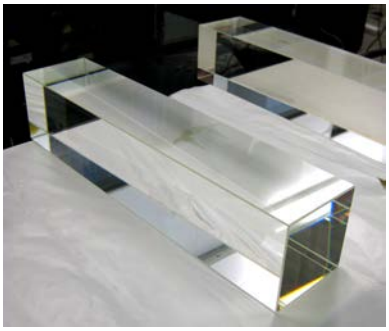

Figure 42: Lead-glass block CEREN 25 (Corning)

Density	4.06 g/cm^3
Radiation length X_0	2.51 cm
Refractive index (at 400nm)	1.708
Refractive index (at 587nm)	1.673
Moliere radius	$3.6 - 3.7$ cm
nuclear collision length	21.4 cm
critical energy	$15.5 - 15.8$ MeV
β_T threshold	0.5978
electron kinetic energy at threshold	126.5 keV

Each lead-glass block has a transverse dimensions of 92×92 mm^2, which is comparable to the transverse size of the electromagnetic showers, and a length of 420 mm corresponding to 16.7 radiation lengths. The are different nomenclatures and mixtures from different manufacturer which are comparable to CEREN 25 from Corning (see tab. [2]). The light transmission coefficient for this lead-glass length is about 0.96 at 400 nm and drops at around 350 nm (see fig. 44).

	CEREN25	SF_5	PEMG4
PbO	55	55.1	54.5
SiO_2	39	39.2	38.5
K_2O	2	3.0	5
Na_2O	3	1.8	1.0
other	–	–	1.0

Table 4: Summary of the mixture of lead-glass: Corning CEREN 25, Schott SF5 and Ohara PEMG4

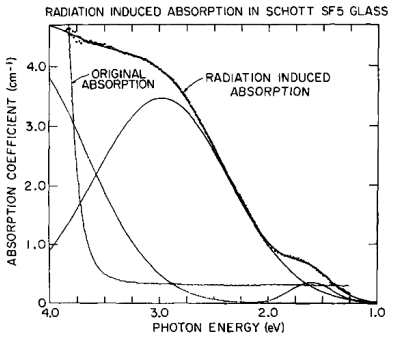

Figure 43: The absorption as a function of photon energy of SF5 before and after exposure to a total dose of 810 Gy of ^{60}Co-radiation. The absorption curve can be resolved with three Gaussian shaped bands corresponding to the *color centers* [17].

Radiation Hardness

Although lead-glass has an excellent radiation hardness in comparison to scintillators, at a certain level of absorbed radiation dose the light transmission coefficient drops and the typical ultraviolet absorption edge (at 3.5 eV photon energy) extends to visible and to the near infra-red wavelengths (see fig. 44).The radiation defects in structure of the glass corresponds to optical absorption bands, known as color centers. In the case of SF5 it is shown that the increase of the absorption coefficient by the superposition of Gaussian-shaped bands can be parametrized by the total absorbed dose in the glass (see fig. 43) [17]. FLUKA simulation show that for Ni+Ni 10 AGeV reactions with 10^5 Hz interaction rate integrated over 2 months of operation the maximal absorbed dose will not exceed 0.3 Gy in the modules with the highest occupancy.

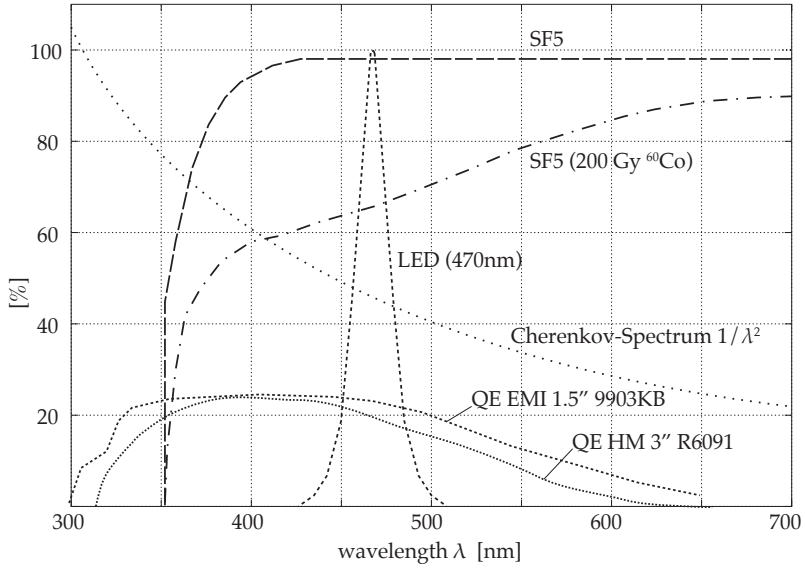

Figure 44: As a function of wavelength, the measured internal transmission of SF5 before and after absorption of a 200 Gy dose from ^{60}Co-radiation [1], the Quantum Efficiency of the 3inch Hamamatsu R6091 [5] and the 1.5inch EMI 9903B [6], the bright blue LED(470 nm) for monitoring and an estimation of a maximal Cherenkov emission spectrum $1/\lambda^2$ is shown.

Readout Scheme and Electronics

The general readout scheme is constrained by two requirements: one is the capability to perform separate time and energy measurements with high resolution in the expected dynamic range. The other is an easy and low cost integration in the existing HADES readout and DAQ infrastructure. To achieve these goals two approaches, *ADC sampling* and *PaDiWa-AMPS*, are considered. The time measurement in both approaches is done by a fast and multi-hit TDC (Time-to-Digital Converter) on the multipurpose TRB (Trigger and Readout Board) [29].

The newest version, the TRB3 (fig. 45), is equipped with several FPGA chips, where the TDCs are implemented with a Tapped Delay Line method. The board has also a high bandwidth DAQ functionality and can transfer up to several hundred MByte/s from up to 256 single edge channels. The digitizing board controls the parameters set on the Front-End (FE) boards by separate slow control lines.

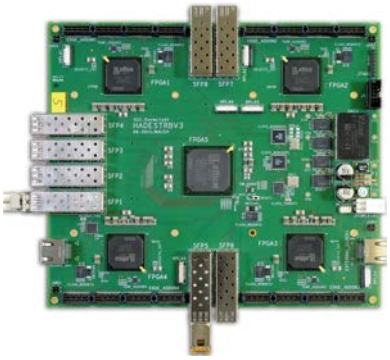

Figure 45: TRB3 multipurpose platform. Equipped with 4 FPGAs for signal digitization and one central FPGA to provide a flexible trigger, data transport and slow control functionality

ADC sampling The first option is based on a traditional ADC (Analog-to-Digital Converter) sampling chain with a dedicated analog FE board (*Cracow FE*) with fast and slow signal processing paths. The collected charge from the PMT is attenuated before splitting and send via slow integrating paths as shaped pulse to a fast sampling ADC. Up to 24 ADC channels are realized on the add-on board which is attached to the TRB3. The fast path contains a discriminator and provides the timing signal to the TRB. The test-results for the prototype *Cracow FE* (fig. 46) under different conditions are presented in the following in this work. A 10 bit 20 MHz ADC add-on-board (fig. 47) with a TRB2, as currently in use for the HADES Pre-Shower detector, was adopted for these tests. Signal processing algorithms consisting of pedestal determination, signal detection, pulse integration, evaluation of the pulse amplitude and time measurement via constant fraction method were implemented inside the FPGA.

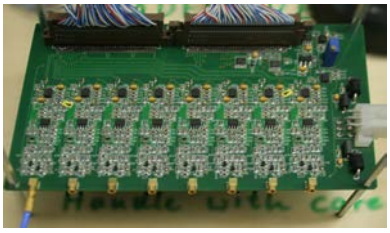

Figure 46: Prototype *Cracow FE* board with 8 channel

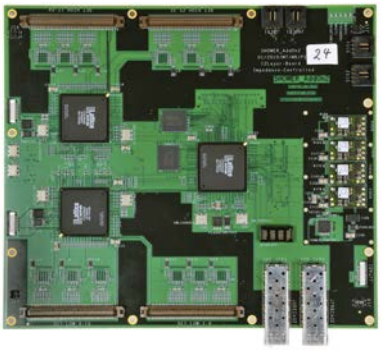

Figure 47: ADC add-on board for the HADES Pre-Shower detector

Charge-to-width conversion The other option (*PaDiWa-AMPS*) (fig. 48) uses the concept of a readout via a charge-to-width conversion based on FPGA. The charge information is extracted by a modified Wilkinson ADC circuit, where the width of the integrated and linearly discharged pulse is measured using a FPGA-TDC, delivering the time measurement of the leading edge, as well as the charge encoded in the width of the digital pulse. A proof-of-concept board and an improved version designed for the HADES ECAL and Hodoscope detector was successfully tested. It is based on the experience with the PaDiWa board and provides 8 input channels (using in total 32 FPGA-TDC channels for two leading edges and two trailing edges for each input channel) with a charge precision of 0.2% and a high dynamic range of 250 [21]. Additionally the dynamic input range can be easily increased with two integrator channels with different gains. The advantage of the new *PADIWA-AMPS* solution is its compact and low cost implementation based on FPGAs and only few additional electronic components. Detailed care in adjustment of the input properties, non-linearities and the later-on calibration has to be performed. The *Cracow FE* solution on the other side is based on nuclear electronics standards developed over decades, has an outstanding performance in terms of linearity and resolution and the ability for pulse analysis in the FPGA.

Figure 48: *PaDiWa-AMPS* board with 8 channel

Rise time	
single ph. elect.	$2.5 - 3$ ns
multi ph. elect.	$\approx 3.5 - 5$ ns
Transit time	
electron	$28 - 48$ ns
spread (FWHM)	$1.2 - 4$ ns
S/N ratio	> 12.5
Pulse amplitude	
20 MeV	50 mV
600 MeV	1.5 V

Table 5: signal parameters assumed or delivered from the manufacturer for the used PMT

Readout requirements

- Dynamic range of the signal amplitude (energy): 5 mV - 5 V
- Accuracy needed for the energy measurement: 5 mV at high amplitudes corresponding to 0.5%
- Each calorimeter sector will deliver 163 independent signals with a expected hit rate of 10 kHz per channel

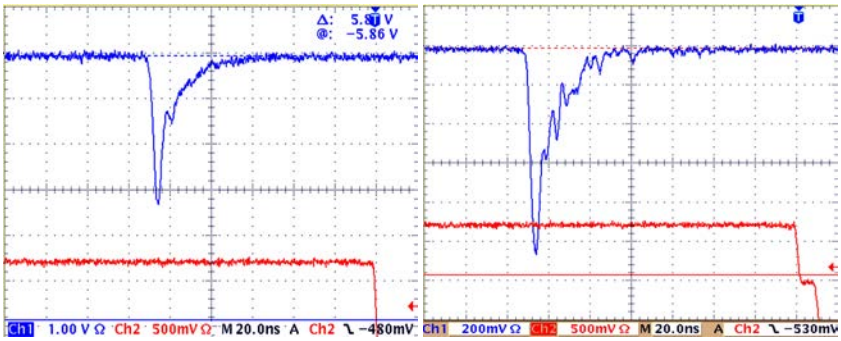

Figure 49: Oscilloscope picture of a cosmics signal (blue) and the coincidence trigger signal (red). Signal amplitude of 3″ Hamamatsu (R6091): $\sim$ 3 V(left) 1.5″ EMI (9903KB): $\sim$ 1 V (right)

Cracow FE board

Measurements with three FE boards, developed at the Smoluchowski Institute of Physics of the Jagiellonian University of Cracow, were performed at GSI Darmstadt. The final *Cracow FE* board will comprise 24 identical channels but the prototype board, used in the tests, was equipped with 8 channel. The description of one channel is given in the following. Since the PMT signal may have high amplitudes, it has to be attenuated before further processing. The FE boards were modified at GSI to optimize the energy resolution. FE1 and FE3 are after the modification identical and have a shaping time of 100 ns and an attenuation to 10% of the input signal before shaping. FE2 comes with an attenuation of the input signal of 40% and a longer shaping time of 150 ns. In fig. 50 the schematics of the FE prototypes is shown. In the slow path the signal is integrated, converted to a differential signal and sent to the ADC for the amplitude measurement.

	FE2	FE1 & FE3
Attenuation factor	~ 0.4	~ 0.1
Linear output range (mV)	$59 - 3370$	$46 - 1835$
Shaping time (ns)		$\sim 600 - 700$
Peak time (ns)		~ 125

Table 6: Parameters measured for FE2 and FE1 & FE3

The AD8099 and AD8139 amplifiers from Analog Devices are used on the prototype board. The peaking time of the integrator circuit was before modification estimated as 400 ns and afterwards measured as 100 – 125 ns (see table 6). As a fast discriminator the ADCMP604

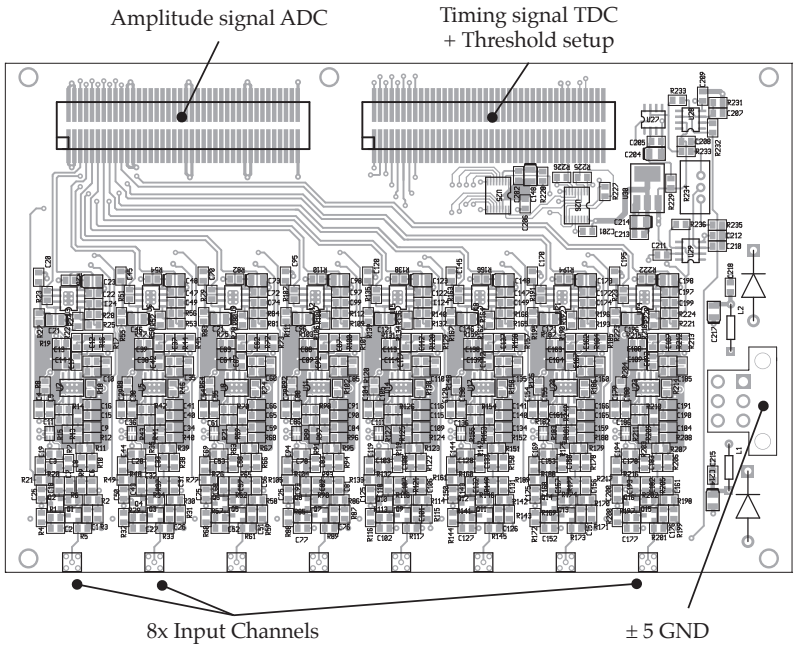

Figure 50: Schematics of the 8 channel prototype *Cracow FE* board

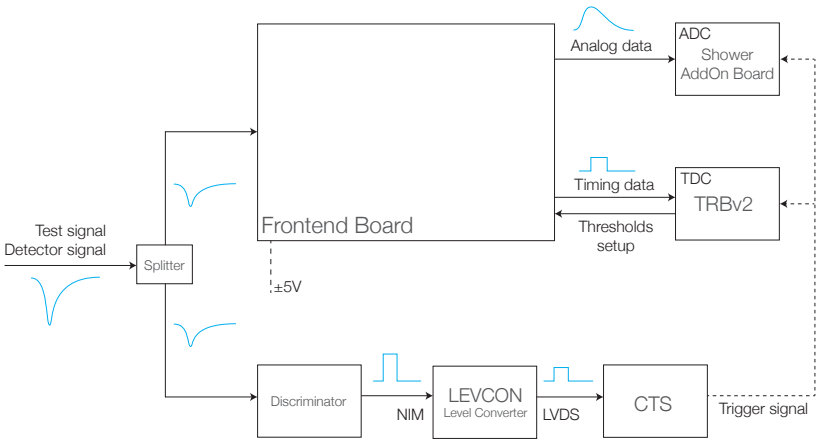

Figure 51: Signal path of the test setup which was used in the laboratory

from Analog Devices with a discriminator delay of 1.6 ns is used. The discriminator threshold is set by a 10-bit DAC and the output voltage step is 3.2 mV. A small programmable digital integrated circuit is needed as an interface for the DAC (Digital-to-Analog Converter) and

is set externally via slow control lines entering the FE board. The input signal walk is compensated off-line by using the measured amplitude level. The discriminator has a differential output working with LVDS signal levels. Two 80-channel cables are foreseen to deliver time and energy signals to the digitizing board. The front-end board is supplied with ± 5 V.

Test Results & Beam-Time

Electronics Resolution - Pulser-Test To determine the intrinsic resolution of the FE boards in combination with the test-chain, the setup was tested with a pulser signal with a width of 10 ns (FWHM) and rise and fall times of 5 ns. The pulser signal was adjusted to be similar to the signals from the detector. For each pulse signal an individual baseline level for the ADC samples was calculated and corrected for. The ADC samples were summed up in a given integration window. The electronic resolution is defined as the ratio of sigma and mean-value of the Gaussian-fit and the time resolution as the sigma-deviation with one TDC channel corresponding to 100 ps (see fig 53). Different approaches

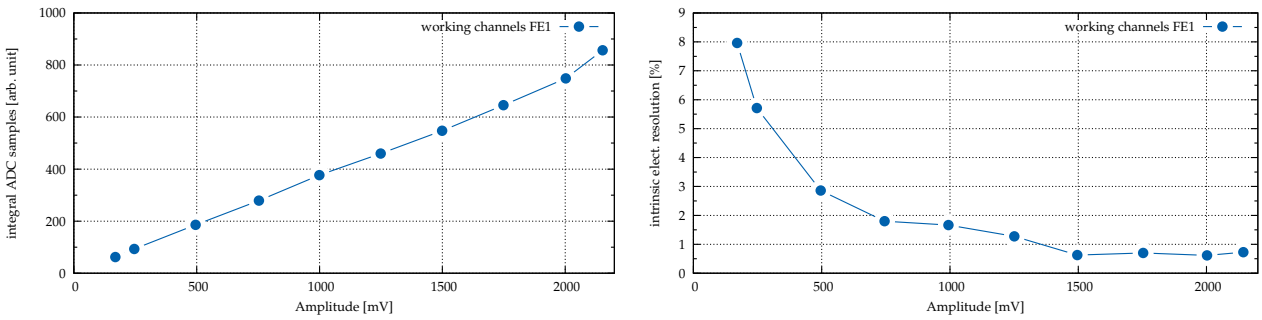

Figure 52: Gain linearity: the integrated ADC value vs. the input amplitude (left) and the intr. electronic resolution vs. input amplitude (right) in one channel of the FE1.

to correct the baseline level and to define the integration window led to comparable resolution values. To study in detail the shaped signal profile a semi Gaussian-fit was used to determine the actual parameter set of the shaping circuit. The first pulser measurements on the FE boards were superimposed with different noise sources in the lab, caused by not sufficient grounding between the components and unstable power supplies. Further investigation showed that some channels of the used FPGA on the ADC board were not working properly. A switch to the next ADC eliminated an oscillating signal in some channels. The pulser measurements also showed deviations in some channels as a consequence of the different signal amplitudes caused by variances in the components and the signal path logic on

the FE and the digitalization boards. The systematic shifts in ADC and TDC values in these channels can be corrected in a calibration procedure. The gain linearity and the electronic resolution was studied

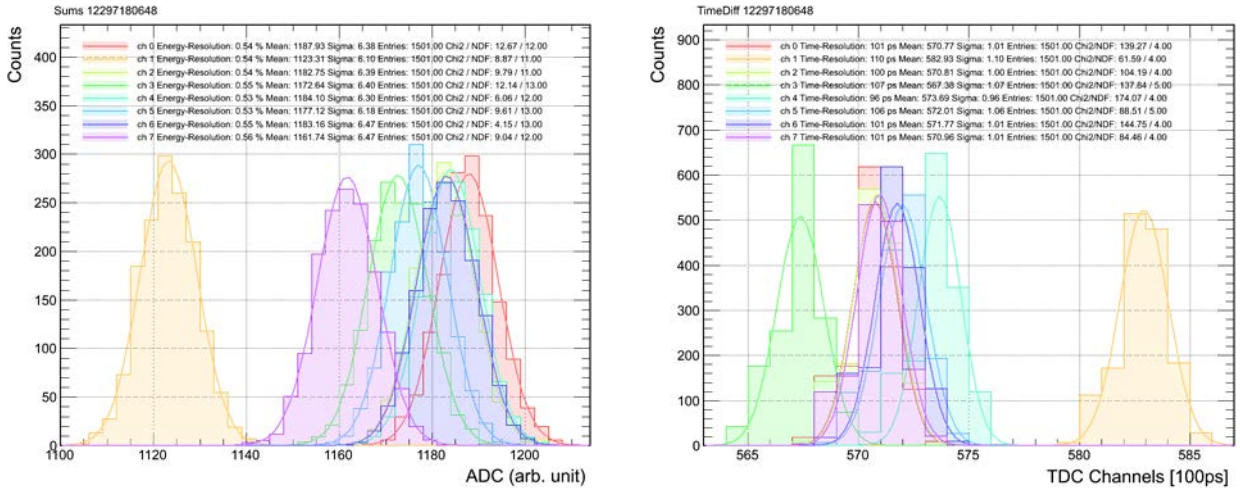

Figure 53: electronic (energy) resolution: 0.6 % (left) and time resolution 100 ps (right). The plots show the ADC sum spectrum and the TDC time difference from raw uncorrected data delivered from the digitization boards. A deviations in amplitude and timing, especially in the second channel is clearly seen.

with the FE boards in the range where the FE will be used and is shown in fig. 52. The electronic resolution is around 0.6% for high values and shows here a bad resolution at low input values due to high noise level between FE and digitization board. This was reduced in later measurements by improved grounding and the change of the power supplies. The time resolution was measured with 100 ps. (see fig. 53).

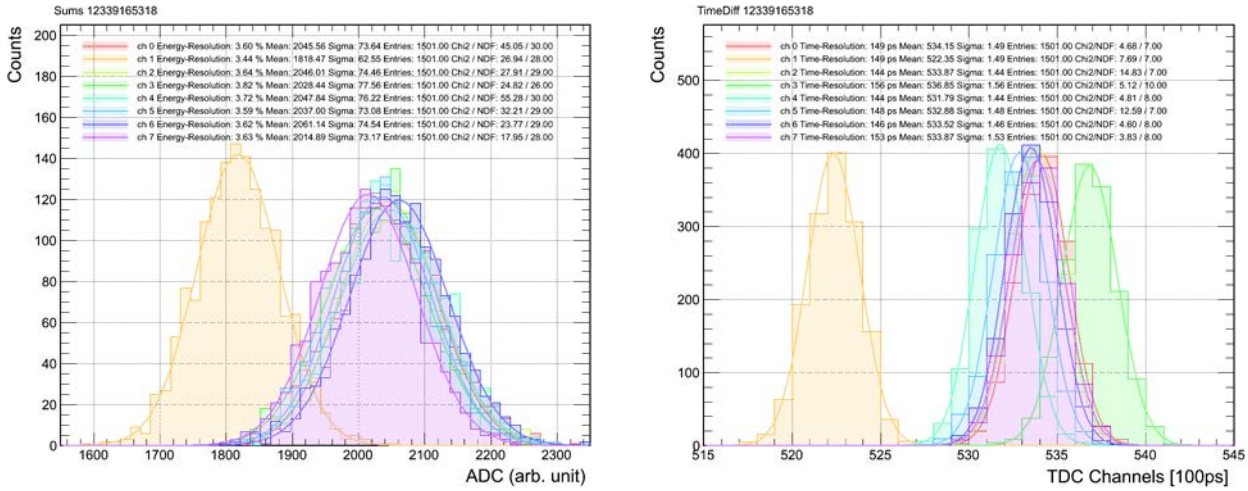

Figure 54: Energy spectrum for blue LED-light and PMT with a resolution of 3.6 % (left) and a time resolution of 150 ps (right).

Pulsed LED-Light & PMT To test the performance of the FE board with realistic signals, the response of the ECAL modules equipped

with optical fibers were tested with pulsed blue LED light. The energy

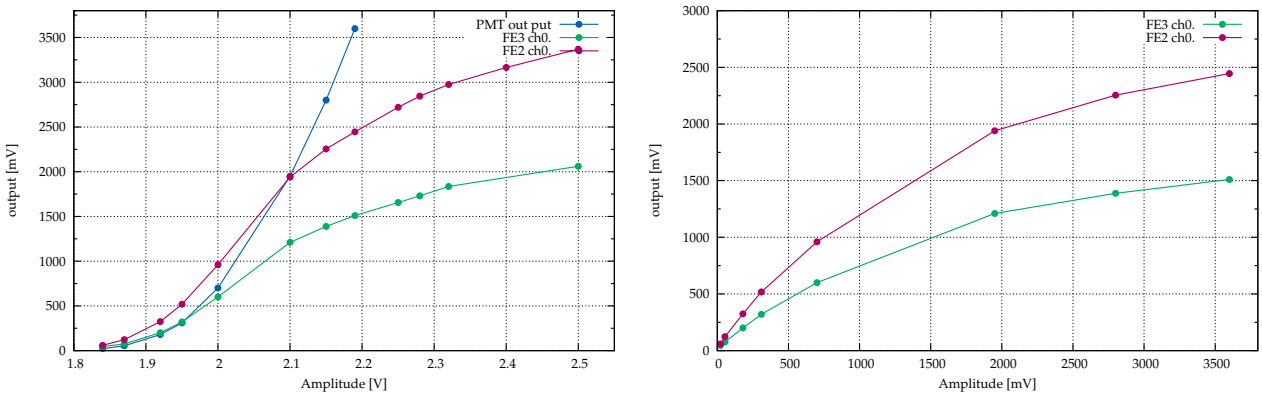

Figure 55: (left) Amplitude of the PMT-Signal as a function of driving voltage of the LED. The PMT-Signal after shaping and attenuation as the FE2 and FE3 output signal. (right) FE response as a function to the PMT signal. Saturation effect of the signal amplitude for both boards is seen.

resolution was measured to be around 3.6 % and the time resolution as 150 ps with all tested FE boards. The pulser parameters are: width: 9.6 ns; edge times: 5 ns; amplitude: 2.15 V; freq.: 400 Hz. (see Fig. 54) The response in therms of linearity to the output signal of PMT to realistic light is shown in figure 55.

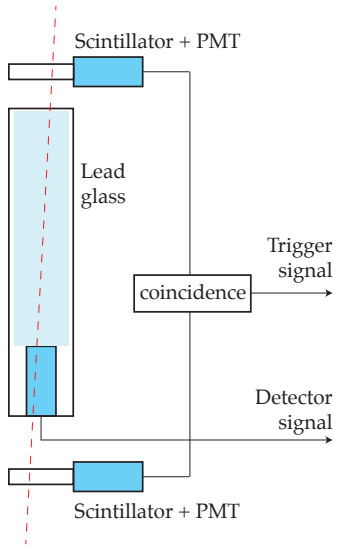

Figure 56: Schematic drawing of one module and the coincidence trigger scintillators

Resolution	HM3	EMI1.5
Energy	9.3 – 11%	13%
Time [ns]	0.82 – 1.15	0.78 – 0.82

Table 7: Cosmic results with the 3″and 1.5″ PMT measured with the *Cracow FE*.

Cosmics Measurements

To study the energy resolution of the modules together with the response of the FE boards a cosmic ray telescope setup was used, where the calorimeter modules are placed vertically between two plastic scintillators with an area of 8×8 cm^2 and 2.5 cm thickness (see fig. 56).

The cosmic ray muons have to pass within $\pm 6.5°$ relative to the axis of a lead-glass block to produce a coincidence trigger signal in the scintillators. As the muon passes through the lead-glass it emits Cherenkov light which corresponds to the equivalent signal amplitude of an electromagnetic shower. With test-beam measurements the pulse height generated by a muon can be related to an absolute energy scale. Measurements with photons at the MAMI accelerator facility showed an equivalent signal amplitude with an energy of 577 MeV. The OPAL collaboration [12] reported an equivalent signal for a 690 MeV electron beam and the WA80 collaboration about 540 MeV for a photon shower in smaller 3.5×3.5 cm^2 SF5 lead-glass blocks [9]. The cosmic muon ray flux at ground [22] is

$$I_\nu \approx 80 m^{-2} \cdot s^{-1} \cdot sr^{-1} \tag{16}$$

which results in a count rate of $\sim$ 11 muons per hour within a solid-angle of $\Omega = 0.006$ sr and a sensitive area of $A = 0.0064$ m^2. In the laboratory an average count rate of $\sim$ 12 per hour was observed.

Long-term measurements with the *Cracow FE* board with cosmic muons show energy resolutions for the different PMT equipped modules between $9.3 - 13\%$ and time resolutions of $700 - 1200$ ps. The test results show indications that the measured resolutions are dependent on the stability of the coincidence scintillator trigger signal. Further studies of the electronics logic producing the trigger signal showed a time resolution of ~ 825 ps which could be improved up to 300 ps by carefully adjusting the used Constant Fraction Discriminators (CFD) to an intrinsic time resolution of around 60 ps. The cosmic results of the same modules measured with different systems (CAMAC and Oscilloscope based DAQ) resulted in an energy resolution between $8.2 - 8.5\%$. This is not explicable by the photon statistics alone which was measured with LED-light as around $3.6 - 4\%$. Additionally, the 3 inch Hamamatsu PMT were not significantly better than the smaller 1 and 1.5 inch PMT as one would expected due to the larger active surface. One explanation could be that the readout-geometry of the cosmic ray telescope is not selective enough in excluding low energy cosmic events. The original cosmic setup of OPAL collaboration [12] consisted of four scintillators constraining the path of the muon and additionally a layer of lead requiring that the minimum energy of the muon exceeds 200 MeV as it passes through the lead-glass.

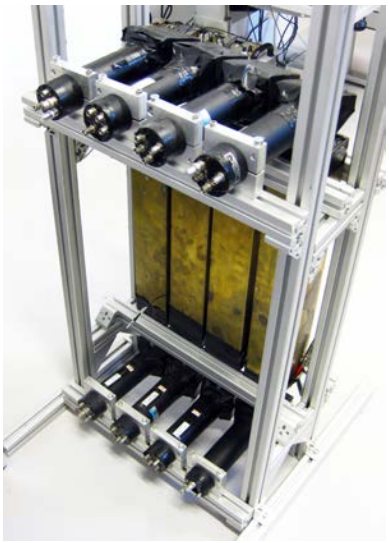

Figure 57: 4 ECAL-modules in the cosmics test-setup with 8 coincidence scintillator triggers up and down

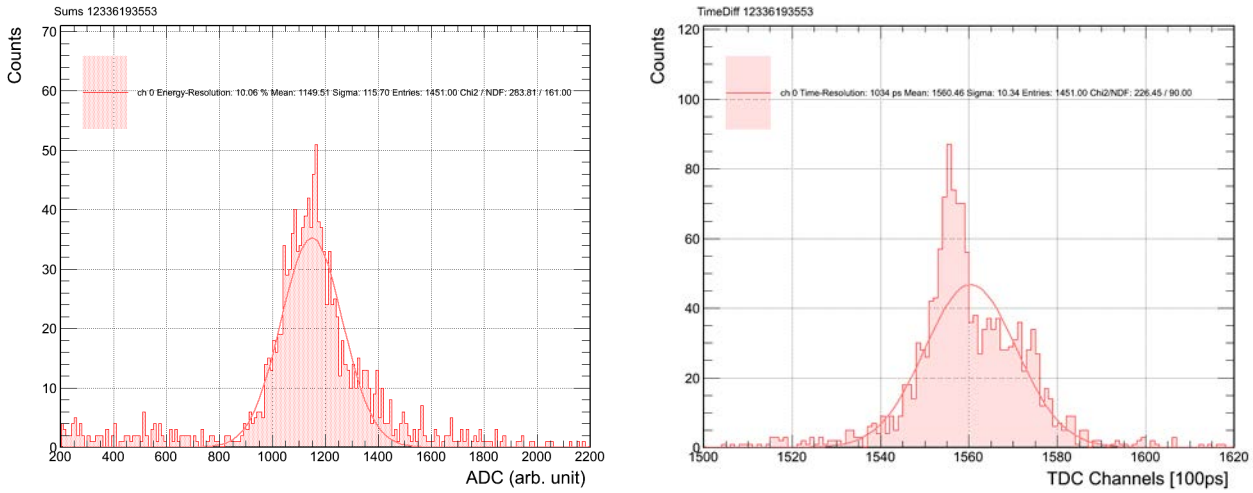

Figure 58: Energy spectrum measured with the cosmics test-setup with a resolution of 10% (left). The plot of TDC time-difference (right) shows a time-resolution of 1 ns. Further tests show that the trigger signal of the coincidence scintillator signal has a time resolution around 825 ps and has also an influence on the measurement of energy resolution.

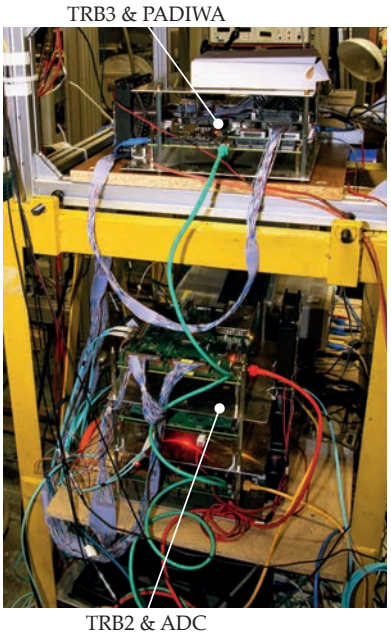

Figure 59: The readout setup with the *PaDiWa-AMPS* & TRB3 and *Cracow FE*, ADC Add-on board & TRB2

Trigger ch.	Tagger ch.	$E_{\gamma Mean}$
0	2	1399.325
1	66	1217.769
2	121	1032.433
3	170	843.379
4	210	678.081
5	261	461.309
6	306	270.894
7	352	81.369

Table 8: Selected channels of the electron tagger, the corresponding mean photon energy and the trigger channel used in the setup.

In Beam tests at the MAMI accelerator (Mainz)

Four calorimeter modules were tested in the A2 hall of the MAMI-C facility in Mainz.

One ECAL module was equipped with a 1.5″ PMT and was already tested in previous beam times at MAMI and CERN, two modules had 3″ PMTs and one contained a 1″ PMT. The high voltage settings of the PMT were adjusted to correspond to the signal amplitude of measured cosmic muons [26].

The detectors were positioned on a movable platform 1 m behind the tagger. The secondary gamma beam, produced via Bremsstrahlung in a copper target from primary electrons, was focused with a 2 mm diameter collimator onto a beam spot of $\approx$ 6 mm on the module front side. The resolution for the MAMI electron beam [20] is quoted with $2-3$ MeV and the time resolution with $\sigma_t = 117$ ps. The energy of each produced photons was determined with the electron taggering method, where the deflected electrons are bend in a magnetic field of 1.83 T and dependent of their energy, are detected by an array of 352 scintillation detectors. Each scintillator tile corresponds to a certain gamma energy with an step size of $2-4.7$ MeV. Eight different triggers were used ranging from 81 to 1399 MeV (see tab. 8). The goal of the beam time was to measure the energy resolution of the three PMT types in combination with the *Cracow FE* and the *PaDiWa-AMPS* readout solution (see fig. 59). As reference readout system a *CAEN DT5742* digitizer with a pulses shaper (MA8000) and a high resolution Rhode&Schwarz oscilloscope (RTO 1044) were used in the beam time.

Measurements of energy resolution

The comparison of the response of the *Cracow FE*, the *PaDiWa-AMPS* and the *CAEN ADC* readout in therms energy resolution are comparable in the full energy range (see fig 61) [26]. In therms of energy resolution

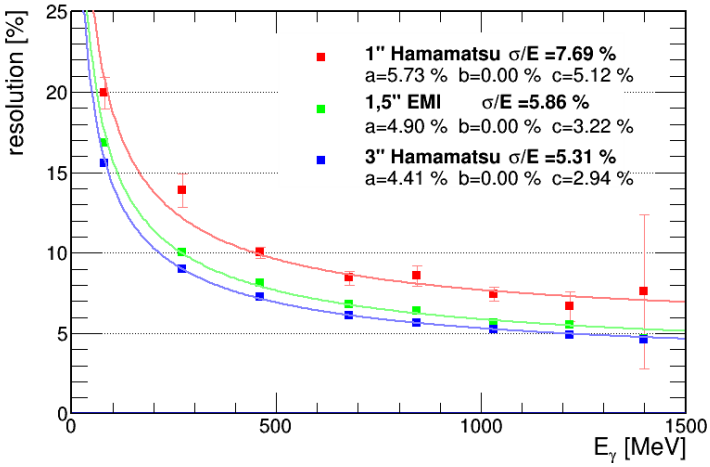

Figure 60: Energy resolution ADC of the PMT with 3-term parameterization

the modules with 1.5″ PMT (5.9% at 1 GeV photon energy) and with 3″ PMT (5.3%) showed comparable response. The module with 1″ PMT was measured with 7.7% and a non-linear behavior due to the increased high-voltage to compensate the smaller output amplitudes. In figure 60 the energy resolution of the three PMTs measured with the *Cracow FE* readout in the 3-term parameterization is shown. In the left figure 62

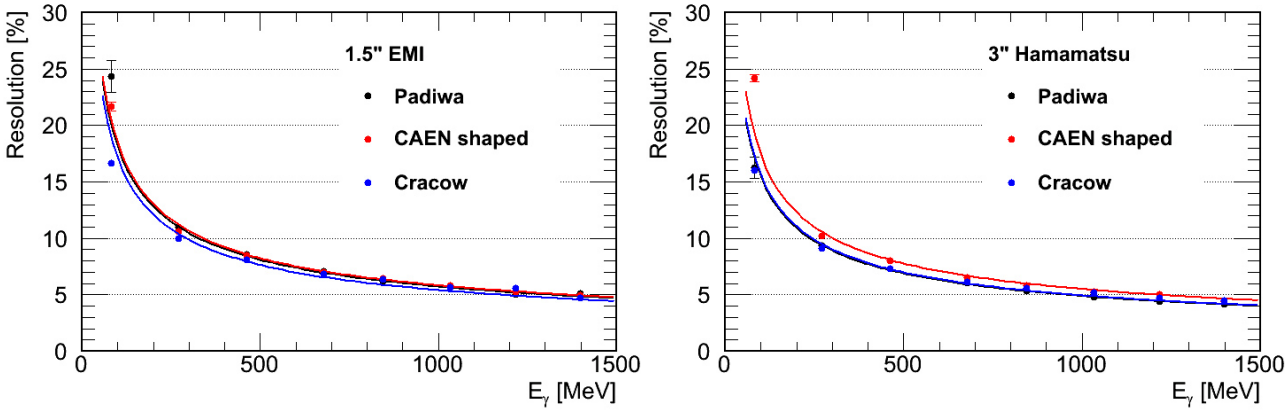

Figure 61: The energy resolution measured with the *CAEN ADC*, the *Cracow FE*, the *PaDiWa-AMPS* readout in combination with 1.5″ PMT EMI (left) and 3″ PMT Hamamatsu (right) [26].

the energy spectrum of the eight different gamma energies (tab. 8) measured with the *Cracow FE* and 3″ PMT Hamamatsu are shown. The values are calculated by the *ADC sum* method, where the ADC values of the PMT pulses are integrated in a certain time window after baseline correction. The mean values and the width for each photon energy

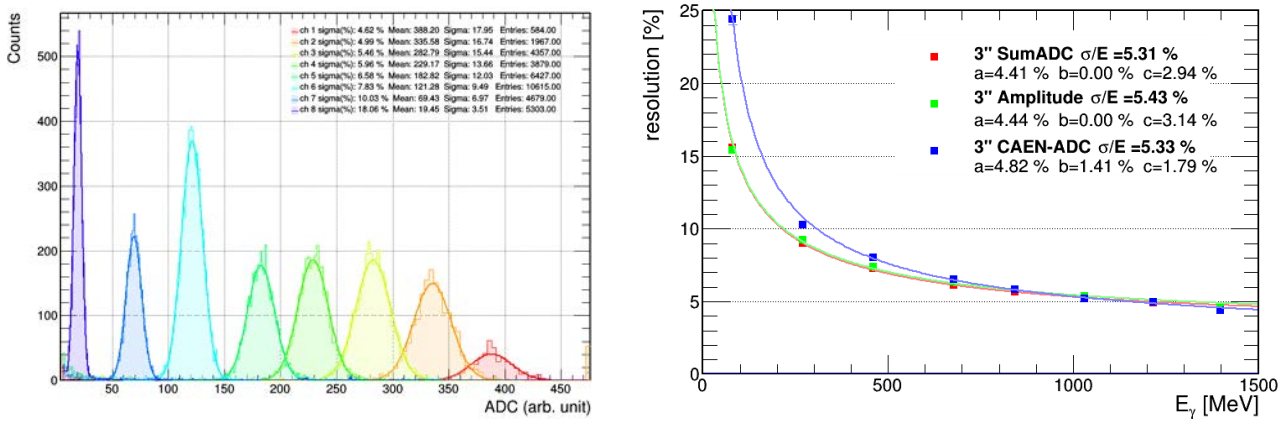

Figure 62: (left) Energy spectrum with the *ADC sum* method measured with the *Cracow FE* and 3″ PMT Hamamatsu. The colors correspond to the eight different energy triggers (tab. 8) and are fitted by Gaussian functions. (right) Comparison between the simple *ADC sum*, the *pulse shape reconstruction* method and the *CAEN ADC* measurement.

is extracted by a Gaussian-fit. In the comparison to the *pulse shape reconstruction* method (see right fig. 62), where the pulse amplitude is reconstructed by a full pulse shape fit, a further improvement due to the method was not observable. The reference *CAEN ADC* measurement

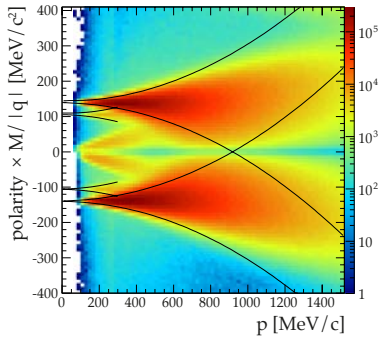

Figure 63: Mass vs. momentoum distribution UrQMD+HGeant FullSimulation Au+Au 4 AGeV (RPC Region) $M/|q|$ times polarity as a function of particle momentum p reconstructed with the RPC detector.

shows a small deterioration to lower energies compared to the *Cracow FE* measurement. The *Cracow FE* and *PaDiWa-AMPS* are optimized with PMT pulses in the lab to provide also sufficient energy resolution in the lower energy spectrum.

Performance & Simulation

The type of the lead-glass, its dimensions and the geometrical arrangement determine the basic physical properties of the calorimeter. An intrinsic energy resolution of $\sigma_E/E \approx 5\%/\sqrt{E}$, an intrinsic spacial resolution of 11 mm at 6 GeV and a pion rejection of $\sim 10^{-3}$ for an electron identification efficiency of $80-90\%$ was achieved in the OPAL experiment [27, 3].

For the HADES ECAL an energy resolution of $\sigma_E/E \approx 6\%/\sqrt{E}$ was chosen as a target value, although simulations show that an energy resolution of $\sigma_E/E \approx 9\%/\sqrt{E}$ would still be acceptable to reconstruct an η-meson in C+C reaction at 8 AGeV[15]. An additional advantage of the upgrade would be the improved electron/pion separation at large momenta ($p > 400\,\mathrm{MeV/c}$). The limit for the *energy resolution* of a calorimeter is determined by fluctuations in the absorption and detection process. The common 3-term parameterization:

$$\sigma_E/E = \frac{a}{\sqrt{E}} \oplus \frac{b}{E} \oplus c \tag{17}$$

allows to distinguish the contribution of different processes with a *stochastic term* ($\sim 1/\sqrt{E}$), an energy dependent *noise term* $\sim 1/E$ and an energy independent *constant term* $\approx const$. The results of the three PMTs measured with the *Cracow FE* readout in the 3-term parameterization and the compilation of other experiments with comparable lead-glass and readout solutions:

Table 9: Comparison to the compilation of results of other experiments with comparable lead-glass and readout solutions.

a[%]	b[%]	c[%]	Material	Reference
4.41	0.0	2.94	CEREN 25	3″ HM *Cracow FE*
4.90	0.0	3.22	CEREN 25	1.5″ EMI *Cracow FE*
5.73	0.0	5.12	CEREN 25	1″ HM *Cracow FE*
~ 5			CEREN 25	OPAL [27]
4	0.5	2.7	SF-5	FOREST [23]
4.2			SF-5	[13]
4.6			SF-5	[16]
4.2		0.64	SF-5	[4]
$4.2-4.8$			SF-5	[19]
4.3		0.43	SF-5	[10]
4.9			SF-5	[14]
6		0.4	SF-5	SAPHIR (WA80) [9]
5.1		1.5	F101	HERMES [7]

Bibliography

[1] P. Achenbach et al. "Radiation resistance and optical properties of lead fluoride Cherenkov crystals". In: *Nuclear Instruments and Methods in Physics Research Section A: Accelerators, Spectrometers, Detectors and Associated Equipment* 416.2–3 (1998), pp. 357 –363. ISSN: 0168-9002. DOI: 10.1016/S0168-9002(98)00748-7.

[2] G. Agakishiev et al. "Inclusive pion and η production in p+Nb collisions at 3.5 GeV beam energy". In: *Phys. Rev. C* 88 (2 Aug. 2013), p. 024904. DOI: 10.1103/PhysRevC.88.024904.

[3] M. Akrawy et al. "Development studies for the OPAL end cap electromagnetic calorimeter using vacuum photo triode instrumented leadglass". In: *Nuclear Instruments and Methods in Physics Research Section A: Accelerators, Spectrometers, Detectors and Associated Equipment* 290.1 (1990), pp. 76 –94. ISSN: 0168-9002. DOI: 10.1016/0168-9002(90)90346-8.

[4] J.A. Appel et al. "Performance of a lead-glass electromagnetic shower detector at fermilab". In: *Nuclear Instruments and Methods* 127.4 (1975), pp. 495 –505. ISSN: 0029-554X. DOI: 10.1016/0029-554X(75)90653-9.

[5] J. Argyriades et al. "Spectral modeling of scintillator for the NEMO-3 and SuperNEMO detectors". In: *Nuclear Instruments and Methods in Physics Research Section A: Accelerators, Spectrometers, Detectors and Associated Equipment* 625.1 (2011), pp. 20 –28. ISSN: 0168-9002. DOI: 10.1016/j.nima.2010.09.027.

[6] G.S. Atoian et al. "Development of Shashlyk calorimeter for KOPIO". In: *Nuclear Instruments and Methods in Physics Research Section A: Accelerators, Spectrometers, Detectors and Associated Equipment* 531.3 (2004), pp. 467 –480. ISSN: 0168-9002. DOI: 10.1016/j.nima.2004.05.094.

[7] H. Avakian et al. "Performance of F101 radiation resistant lead glass shower counters". In: *Nuclear Instruments and Methods in Physics Research Section A: Accelerators, Spectrometers, Detectors and Associated Equipment* 378.1–2 (1996), pp. 155 –161. ISSN: 0168-9002. DOI: 10.1016/0168-9002(96)00443-3.

[8] T.C. Awes et al. "The Midrapidity calorimeter for the relativistic heavy ion experiment WA80 at CERN". In: *Nucl.Instrum.Meth.* A279 (1989), pp. 479–502. DOI: 10.1016/0168-9002(89)91295-3.

[9] H. Baumeister et al. "Design and performance of the saphir lead-glass calorimeter". In: *Nuclear Instruments and Methods in Physics Research Section A: Accelerators, Spectrometers, Detectors and Associated Equipment* 292.1 (1990), pp. 81 –96. ISSN: 0168-9002. DOI: 10.1016/0168-9002(90)91736-U.

[10] J.S. Beale et al. "A lead-glass Cherenkov detector for electrons and photons". In: *Nuclear Instruments and Methods* 117.2 (1974), pp. 501 –508. ISSN: 0029-554X. DOI: 10.1016/0029-554X(74)90298-5.

[11] C. Behnke. "Reconstruction of π^0 and η mesons via conversion method in Au+Au at 1.23AGeV with HADES". In: *J.Phys.Conf.Ser.* 503 (2014), p. 012015. DOI: 10.1088/1742-6596/503/1/012015.

[12] R. M. Brown et al. "An Electromagnetic Calorimeter for Use in a Strong Magnetic Field at LEP Based on CEREN 25 Lead Glass and Vacuum Photo-Triodes". In: *Nuclear Science, IEEE Transactions on* 32.1 (Feb. 1985), pp. 736–740. ISSN: 0018-9499. DOI: 10.1109/TNS.1985.4336933.

[13] U. Buchner et al. "Performance of a scintillating glass calorimeter for electromagnetic showers". In: *Nuclear Instruments and Methods in Physics Research Section A: Accelerators, Spectrometers, Detectors and Associated Equipment* 272.3 (1988), pp. 695 –706. ISSN: 0168-9002. DOI: 10.1016/0168-9002(88)90750-4.

[14] Gerhard Czapek et al. "A lead-glass Cherenkov detector for electrons in the 100 MeV region". In: *Nuclear Instruments and Methods* 125.1 (1975), pp. 41 –44. ISSN: 0029-554X. DOI: 10.1016/0029-554X(75)90550-9.

[15] W. Czyzycki et al. "Electromagnetic Calorimeter for HADES". In: (2011). arXiv:1109.5550 [nucl-ex].

[16] F. Dydak et al. "Performance of a lead-glass detector for high-energy -rays". In: *Nuclear Instruments and Methods* 137.3 (1976), pp. 427 –434. ISSN: 0029-554X. DOI: 10.1016/0029-554X(76)90463-8.

[17] M. Goldberg et al. "Radiation induced coloring of Cherenkov counter glasses". In: *Nuclear Instruments and Methods* 108.1 (1973), pp. 119 –123. ISSN: 0029-554X. DOI: 10.1016/0029-554X(73)90644-7.

[18] HAMAMATSU. "HAMAMATSU PMT Handbook - PHOTOMULTIPLIER TUBES – Basics and Applications". In: (). URL: http://www.hamamatsu.com/resources/pdf/etd/PMT_handbook_v3aE.pdf.

[19] M. Holder et al. "A high-resolution total absorption spectrometer for simultaneous detection of several high-energy $\gamma - rays$". In: *Nuclear Instruments and Methods* 108.3 (1973), pp. 541 –550. ISSN: 0029-554X. DOI: 10.1016/0029-554X(73)90536-3.

[20] J.C. McGeorge et al. "Upgrade of the Glasgow photon tagging spectrometer for Mainz MAMI-C". In: *Eur.Phys.J.* A37 (2008), pp. 129–137. DOI: 10.1140/epja/i2007-10606-0. arXiv:0711.3443 [nucl-ex].

[21] A Neiser et al. "TRB3: a 264 channel high precision TDC platform and its applications". In: *Journal of Instrumentation* 8.12 (2013), p. C12043. URL: http://stacks.iop.org/1748-0221/8/i=12/a=C12043.

[22] K.A. Olive et al. "Review of Particle Physics". In: *Chin.Phys.* C38 (2014), p. 090001. DOI: 10.1088/1674-1137/38/9/090001.

[23] M. Sato et al. "Energy Resolution of an SF-5 Lead Glass Cerenkov Counter". In: *Research Report of Laboratory of Nuclear Science, Tohoku University* 41 (2008). URL: http://www.lns.tohoku.ac.jp/fy2011/research/report/2008/01-06.pdf.

[24] S. P. Stoll. "An Investigation of the Reflective Properties of Tyvek Papers and Tetrates PTFE Film". In: (1996). PHENIX Note No.245. URL: https://www.phenix.bnl.gov/WWW/emcal/papertrail/phenix_notes/reflect.ps.

[25] S. P. Stoll. "Comparison of New and Old Tyvek Style 1055B". In: (1997). Addendum to PHENIX Tech. Note 245. URL: https://www.phenix.bnl.gov/WWW/emcal/papertrail/phenix_notes/refle_ad.ps.

[26] O Svoboda et al. "Verification of Electromagnetic Calorimeter Concept for the HADES spectrometer". In: *Journal of Physics: Conference Series* 599.1 (2015), p. 012026. URL: http://stacks.iop.org/1742-6596/599/i=1/a=012026.

[27] "The OPAL detector at LEP". In: *Nuclear Instruments and Methods in Physics Research Section A: Accelerators, Spectrometers, Detectors and Associated Equipment* 305.2 (1991), pp. 275 –319. ISSN: 0168-9002. DOI: 10.1016/0168-9002(91)90547-4.

[28] P. Tlusty et al. "Development of the HADES Electromagnetic Calorimeter". In: *Scientific Report 2012*. Vol. 2013-1. GSI Report. 06fy9001i, 06fy7114. Darmstadt: GSI Helmholtzzentrum für Schwerionenforschung, 2013, 37 p. URL: http://repository.gsi.de/record/51943.

[29] C Ugur et al. "A 16 channel high resolution (<11 ps RMS) Time-to-Digital Converter in a Field Programmable Gate Array". In: *Journal of Instrumentation* 7.02 (2012), p. C02004. URL: http://stacks.iop.org/1748-0221/7/i=02/a=C02004.

Glauber Model Framework

In his original lectures in 1958, Roy J. Glauber [77, 76] summarizes the mathematical methods and approximations for treating the quantum mechanical problem of multiple nuclear scattering at high energies with purely quantum mechanical eikonal wavefunctions. Although some of the techniques were known before, nor derived by Glauber himself, the name *Glauber model* is generally used to denote this type of models. Glauber pointed out that his theory is based on work by Molière (1947) [65] on the elastic scattering of fast charged particles.

The approximation used by Glauber belongs to the family of so-called *eikonal approximations*, which were studied by many others before[3]. It turns out that from the many possible quantum mechanical approximations, the version by Glauber is one of the simplest formulation with the feature of simplifying the evaluation of eikonal scattering amplitudes for more complicated collisions.

[3] Some of earlier origins of an equivalent formulation can be found in the footnote of [82]

Two different approaches for the description of nuclear multiple scattering are summarized under the term *Glauber Model*. The general one, derived from the quantum mechanical treatment based on eikonal wavefunctions, can only be derived analytically for very light systems ($A \leqslant 4$) and for medium sized systems ($A \approx 12$) in next-to-leading-order expansions [39]. The second, the semi-classical approximation of the first, is the interpretation in terms of survival probabilities for the scattered nucleons in forward direction. It is called the *Optical Glauber Model* and uses the optical-limit approximation to simplify the highly multidimensional integrals, particularly for heavy nuclei, and makes numerical calculations possible. Despite being a simplification of the complex dynamics in a many-body nuclear reaction, it has turned out to be a fairly accurate and practical formulation.

Originally, the *Glauber Model* was formulated to describe the cross section in a deuteron-nucleus reaction (1955) [45, 40] using a *shadow or eclipse correction*. It was further developed to understand the elastic scattering peaks in nucleon-nucleus (1967) [35] and in nucleus-nucleus collisions (1969) [32]. The success motivated many authors [42, 61, 50, 38] to formulate the Glauber approach for inelastic nucleus-nucleus collisions (1968-69).

To describe the fragmentation process, the *abrasion and ablation model* by Swiatecki et al. (1973) [21, 57] pictured the nuclear collision as a sequential process. The two nuclei, who are passing each other closely, cut off an overlapping volume in a *abrasion* process. The scraped-off volume is proportional to the number of participating nucleons and the remaining spectator nucleons outside of the overlap region do not experience any violent interaction.

The *wounded-nucleon model* by Bialas et al. (1976) [19] introduced the idea that the multiplicity distribution of produced particles in a nucleus-nucleus collision can be described as the incoherent superposition of the multiplicity distributions of each wounded nucleon, *i.e.* all nucleons which undergo at least one inelastic collision. On the base of probability arguments the number of collisions (N_{coll}) and the number of wounded, or also called participating, nucleons (N_{part}) can be calculated[4].

[4] Although the therms *wounded* and *participating* nucleons have different origins and meanings, it is common, at least for recent Glauber MC studies, to use them synonymously. In the following the term number of *participating* nucleons N_{part} is used as the probabilistic scaling value described in the *wounded-nucleon model* [46].

One of the first predecessors of the modern and commonly used *Glauber Monte Carlo Models* [64] was the *rows-on-rows model* from Hüfner and Knoll (1977) [56]. With the emergence of most of the modern event-based generators (see tab. 10) at the beginning of the 90's, the *Glauber Monte Carlo* was a practical chose for the initial state, where specific production points were needed in the models. It is the reduction of the concept to two ingredients: the frozen configuration of nucleons in two colliding nuclei and the modeling of the individual nucleon-nucleon collisions according to a profile function and elementary cross sections. The most striking feature of the Monte Carlo implementation is the possibility of event-by-event calculations, where not only averaged quantities are computed as in the general *Glauber Model* approach, but also the underlying fluctuation and correlation between these quantities can be easily studied. Two specialized Monte Carlo Packages *TGlauberMC* [8, 63] and *GLISSANDO 2* [81] were used in this work.

DIAGEN	[84]	'89
HIJET	[85]	'89
VENUS	[98]	'89
RQMD	[88]	'89
HIJING	[97]	'91
FRITIOF	[71]	'92
LUND	[33]	'93

Table 10: *Glauber Monte Carlo* based event generator and year of publishing

Limitation of the Glauber Model at low energies

The study of nuclear reactions has been done mainly in two complementary versions of the multiple scattering theory. The *optical potential model* of Kerman, McManus and Thaler [60], often been used to analyze experiments at low energies, and the *Glauber Model* motivated by high energies experiments, where nucleon-nucleon cross sections are more forward peaked. The comparison of the results from both models was often used as a verification [36]. It was shown that with appropriate corrections of the order of 15% the validity of the *eikonal Glauber Model* can be extended down to energies as low as about 45 MeV [27].

The *Glauber Model* assumes that at sufficiently high energy the nucleons in the nuclei will essentially pass through each other nearly undeflected on straight lines as excited objects. This semi-classical de-

scription requires that the reduced de Broglie's wavelength, $\lambda\!\!\!^{-}_B = \hbar/p$, where p is the characteristic momentum of the particle, is small relative to the size of the nucleus. This condition is satisfied in the region

$$\lambda\!\!\!^{-}_B \approx 0.2\text{fm} \ll R \approx 5.4\text{fm}. \tag{18}$$

with a nucleon of 1.955 GeV/c momentum traversing a gold nucleus.

Geometrical picture of nucleus-nucleus collision

One of the important values to characterize nuclear reactions is the *total reaction cross section*[5] (σ_R), which is defined as the *total* (σ_{tot}) minus the *elastic cross section* (σ_{el}):

$$\sigma_R = \sigma_{tot} - \sigma_{el} \tag{19}$$

[5] In the following the term *total reaction* and *total inelastic cross section* is used synonymously. In the common definition a nuclear reaction occurs, if at least one nucleon is scattered inelasticly.

The *total reaction cross section* has been studied systematically for both, theory and experiment, and several empirical parameterizations have been developed. It was shown [48], that for various collision systems at beam energies above 1 AGeV the experimental data can been described by parameterizations within $5-10\%$ w.r.t. the *total cross section* and within $10-20\%$ w.r.t. the *reaction cross section*. Experimentally, it is challenging in heavy-ion reactions to distinguish between elastic and inelastic reactions with a high accuracy.

In a geometrical picture, where two colliding nuclei are considered as black disks, one can assume, due to the short range of the strong force and neglecting electromagnetic interactions, that the nuclei will interact when their sharp edges touch. This *reaction cross section* corresponds to the *geometrical cross section*:

$$\sigma_{geom} = \pi(R_{proj} + R_{targ})^2 = \pi b_c^2 \tag{20}$$

where b_c is the maximal critical impact-parameter, inside which nuclear reactions will occur with high probability (see fig. 64). By using the relation between the nuclear radius R and the mass number A, parametrized as $R = r_0 A^{1/3}$, one can describe the cross section in terms of the atomic weight:

$$\sigma_{geom} = \pi r_0^2 (A_{proj}^{1/3} + A_{targ}^{1/3})^2 \tag{21}$$

This parameterization is also referred to as *sharp cut* with a radius parameter around $r_0 = 1.15 - 1.27$ fm. From the analysis of interactions of cosmic rays in emulsions, Bradt and Peters [22] formulated the following parametrization:

$$\sigma_{geom} = \pi r_0^2 (A_{proj}^{1/3} + A_{targ}^{1/3} - c)^2 \tag{22}$$

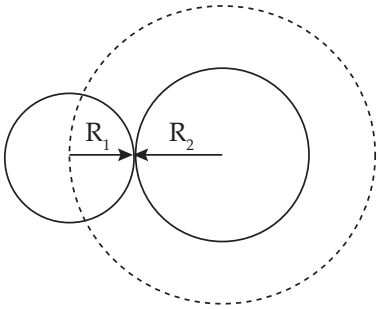

Figure 64: Definition of the geometrical cross section (adapted from [15]).

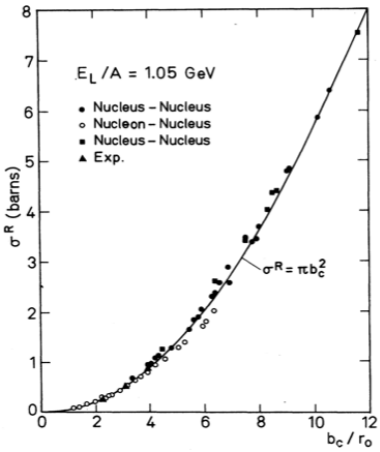

Figure 65: Total reaction cross section for nucleon-nucleus and nucleus-nucleus interactions at 1.05 GeV/nucleon as a function of b_c/r_0 from Glauber calculations in comparison to data [58] (taken from [17])

where c is the *overlap parameter* describing the diffuseness and partial transparency of the surfaces of the nucleus. To describe large size nuclei, the *overlap parameter* can been adjusted proportional to the surface of the nuclei:

$$c = b_0(A_{proj}^{-1/3} + A_{targ}^{-1/3}) \tag{23}$$

This results in the following energy-independent formulation by Vary et al. [14, 17]:

$$\sigma_{geom} = \pi r_0^2 (A_{proj}^{1/3} + A_{targ}^{1/3} - b_0(A_{proj}^{-1/3} + A_{targ}^{-1/3}))^2 \tag{24}$$

In figure 65 data from the Bevalac [58] in comparison with Glauber

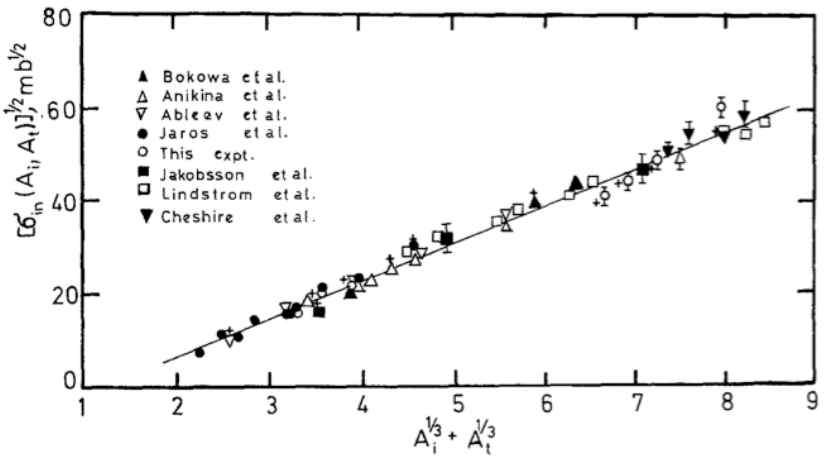

Figure 66: Inelastic nucleus-nucleus cross-sections as a function of the atomic weight of the projectile nucleus A_{proj} and of the target nucleus A_{targ}. Crosses in the plot show results from the *soft-sphare model* calculation [59] (taken from [2])

calculations are shown and in figure 66 data from the Bevalac and the Dubna Synchrophasotron are compared to calculations of the *soft-sphere model* [59]. The resulting parameters from the fits to the data are listed in table 11.

Table 11: Total reaction cross section for Au+Au reactions with $A = 197$ calculated with the parameterization by Vary et al. (eq. 24) using parameters and errors taken from the indicated references.

r_0 [fm]	b_0	cross section [mb]	beam energy [AGeV]	reference
1.34	0.75	7305	$1.05 - 2.1$	Vary et al. [17]
1.36	1.11 ± 0.05	7362 ± 16	2.1	Heckman et al. [52]
1.33 ± 0.04	0.85 ± 0.1	7153 ± 335	$0.5 - 4.2$	Abdrahmanov et al. [2]

There are further formulations with additional terms to account for deviations to experimental data over a broad energy range and system sizes. Some popular parameterizations are from Sihver [87], Kox [62, 92], Shen [83] and Tripathi [30]. In the GEANT4 package a parameterization based on a simplified Glauber approach is included [48].

In table 12 a comparison of estimations for the total reaction cross section of Au+Au based on the sharp-cut approximation used by the FOPI and KaoS experiments, the parametrization from Vary et al. (equation 24) and calculations with the microscopic *soft-sphare model* by Karol [59] for at 1.23 AGeV are shown.

method & reference	parameter	cross section
Sharp-cut approximation (eq. 21)		
FOPI [74]	$r_0 = 1.17$ fm	5.9 barn
FOPI [75]	$r_0 = 1.15$ fm	5.6 barn
KaoS [95]	$r_0 = 1.27$ fm	6.9 barn
KaoS [89]	$r_0 = 1.2$ fm	6.1 barn
Parameterization (eq. 24)	$r_0 = 1.33 \pm 0.04$ fm $b_0 = 0.85 \pm 0.1$	7153 ± 335 mb
Karol [59]	$\sigma_{tot}^{pp} = 47.4 \pm 2$ mb	6899 ± 40 mb
	$\sigma_{tot}^{np} = 39.35 \pm 2$ mb	

Table 12: Compilation of the total reaction cross section for Au+Au estimated by the sharp-cut approximation used by the FOPI [74, 75] and KaoS [95, 89] experiments, the parametrization from Vary et al. (equation 24 with parameters from [2]) and calculations with the microscopic *soft-sphare model* by Karol [59] with modification from [24] (code taken from here [29]).

Glauber Monte Carlo

The *Glauber Monte Carlo* calculation has the feature of easy implementation and proceeds event-by-event as follows [7]:

1. **Impact parameter selection:** The two nuclei are separated in the x-direction by an impact parameter (b), chosen randomly according to the probability distribution $P(b) \propto bdb$ (up to $b_{\max} \simeq 20\,\text{fm} > 2R_A$). The center of nucleus A is positioned in the x-direction at $x_A = -b/2$ in the transverse plane, while nucleus B is centered at $x_B = +b/2$. By definition the reaction plane is oriented along the impact parameter and the beam direction and are defined here by the x- and z-axes. The transverse plane is given by the x- and y-axes.

2. **Generation of nuclei:** For each nucleus, we loop over the number of nucleons (N_A and N_B) and choose randomly for each nucleon position, azimuthal ($cos\theta$) and polar (ϕ) angles (both uniformly distributed in spherical nuclei), as well as a radius (r) which is sampled according to the radial density distribution ($r^2\rho(r)$). Additionally,

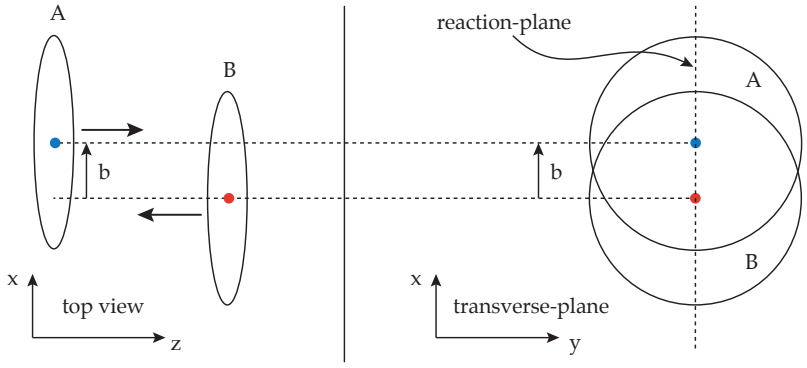

Figure 68: Schematic picture of the orientation of two nuclei in the *Glauber Monte Carlo* reference frame (adapted from [64]).

a minimum inter-nucleon separation distance ($d_{\min}$) between the nucleon centers of all nucleons in the nucleus is required. Each time

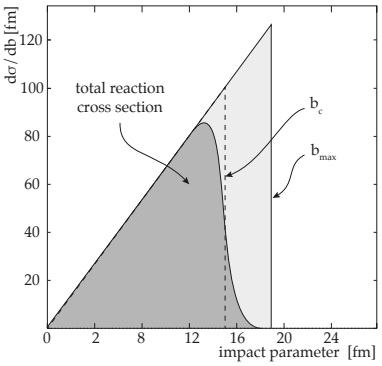

Figure 67: Schematic illustration of the impact parameter distribution. b_c is the maximal critical impact-parameter and b_{max} the maximum of the parameter range.

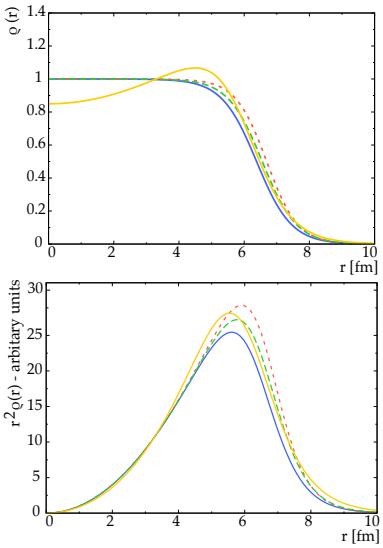

Figure 69: Density distributions $\rho(r)$ (top) and $r^2\rho(r)$ (bottom) of the two- or three-parameter Fermi parametrization.
2pF $R = 6.38$fm $a = 0.534$fm
2pF $R = 6.69$fm $a = 0.476$fm
2pF $R = 6.55$fm $a = 0.523$fm
3pF $R = 6.07$fm $a = 0.613$fm $w = 0.64$

Figure 70: Schematic picture of a collision with an impact parameter of $b = 6$ fm (adapted from [64]).

the distance between the newly generated and any existing nucleon nearby falls below this criteria, a new position is chosen. This introduces a geometrical correlation among the nucleon positions [25, 79, 9], and also affects the volume of the nucleus. The nucleus starts to *swell* above the given radial density distribution and the boundary of the nucleus becomes more diffuse. To compensate this effect the parameters of the input distribution have to be appropriately adjusted [63, 53, 86]. In this work a method is implemented, where the RMS-radius of the generated nucleus is calculated and constrained to the precise measured value.

Due to fluctuations in the positions of the nucleons, the center-of-mass of the generated nuclei also fluctuates around the center of the reference frame. To ensure that the nuclear reaction is exactly performed each time with the initially chosen impact parameter, the generated nuclei are correctly re-positioned by shifting all nucleon centers by the average offset determined after the positions of all nucleons in the nucleus have been determined.

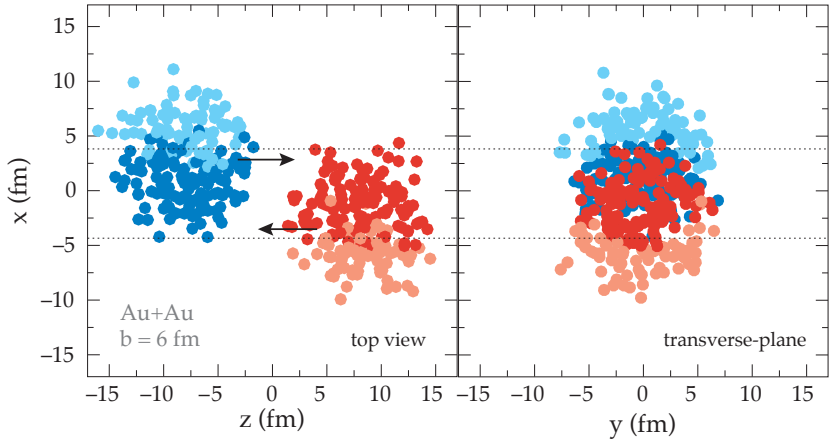

3. **Collision process:** For each nucleon i in nucleus A, we loop over the nucleons j in nucleus B. There a several methods to decide whether a collision between each individual nucleons from A and B occur. In the *black disk approximation* one assumes that the nucleons interact inelasticly with the probability of one, if the 2-dimensional transverse distance $d_{ij} = \sqrt{\Delta x^2 + \Delta y^2}$ between the nucleons is less than the radius defined by the inelastic NN cross section σ_{NN}^{inel}:

$$(\Delta x)^2 + (\Delta y)^2 \leq \sigma_{NN}^{inel}/\pi \tag{25}$$

The *grey disk approximation* differs from the *black disk* with the condition, that a collision occurs with a reduced probability by the ratio $\sigma_{NN}^{inel}/\sigma_{NN}^{tot}$ in a radius defined by the total NN cross section σ_{NN}^{tot}.

In the *profile function approach* [11, 78, 80], the probability of an interaction between the nucleons i and j is given by

$$P(d_{ij}) \;=\; 1 \;-\; \left|1 - \Gamma(d_{ij})\right|^2 , \tag{26}$$

where the profile function Γ in the general *eikonal-form* is expressed in terms of the total and elastic NN cross sections as follows:

$$\Gamma(d_{ij}) \;=\; \frac{\sigma_{NN}^{tot} \cdot (1 - i\alpha)}{4\pi B}\, e^{-d_{ij}^2/(2\,B)} , \tag{27}$$

with α the ratio of real/imaginary parts of elastic amplitude and B the slope parameter of the differential elastic cross section (at $t = 0$):

$$B = \frac{1 + \alpha_{NN}^2}{16\pi} \cdot (\sigma_{NN}^{tot})^2 / \sigma_{NN}^{el} . \tag{28}$$

This profile function Γ can be modeled with a gamma or Gaussian function according to the elastic and total NN cross section [71] (see fig. 71).

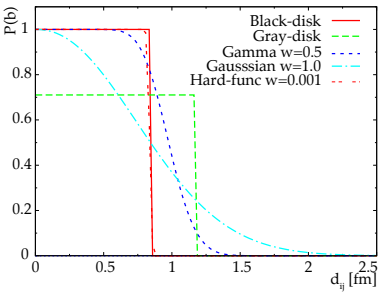

Figure 71: The interaction probability as a function of the nucleon-nucleon transverse distance d_{ij}. The black- and grey-disk is shown in comparison to parametrization with a gamma and Gaussian function, modeled according to the total and elastic NN cross section.

4. The nucleons are tagged as wounded (participating) if they suffer at least one collision. Otherwise, they are listed as spectator. Event counters for the determination of the total reaction cross section are updated accordingly.

5. For the A + B collision one can then calculate the geometrical properties, e.g. eccentricity, plane axes, number of participating nucleons and binary collisions, etc.

Parameter range and systematic errors

Extensive studies of the systematics of the Glauber MC calculations are done in the high energy range of RHIC [4, 64], LHC [3] and also at SPS energies [80]. Mainly caused due to the great interest in the effect of the anisotropic behavior of the initial state fluctuations on collective flow observables. Systematic analyses of the initial condition in the low relativistic energy regime (1 AGeV) are mostly done as part of nuclear transport models [96] and not independently studied by the Glauber MC approach. In order to estimate the systematic errors of the Glauber MC calculation, the different model parameters are varied in suitable ranges, which are constrained by available data or by conservative uncertainties (following [41, 72]). The model parameter can be divided into energy dependent parameters (see tab. 13), used in the modeling of the individual nucleon-nucleon collision, and the energy independent parameters (see tab. 14), used for the configuration of the nuclei, and are discussed in the following. Since the main focus of this work is the centrality estimation, we only consider the error estimation of the total

NN inelastic cross section	
σ_{NN}^{inel}	23.8 ± 2 mb
isospin NN total cross section	
σ_{NN}	43.6 ± 0.7 mb
Ratio of real/imaginary parts of elastic amplitude (at $t = 0$)	
α	-0.2 ± 0.2 mb
Slope of elastic cross section (at $t = 0$)	
B	$5.97 \pm 0.25\ (GeV/c)^{-2}$

Table 13: Parameters used in the modeling of the nucleon-nucleon collisions for beam energy 1.23 AGeV [68, 28, 41, 72].

radius parameter	
R	6.554 ± 0.2 fm
diffuseness parameter	
a	0.523 ± 0.1 fm
inter-nucleon exclusion distance	
d_{min}	0.9 ± 0.9 fm
deformation parameters	
β_2	-0.13 ± 0.06 fm
β_4	-0.03 ± 0.03 fm

Table 14: Parameters used in the generation of the gold nuclei.

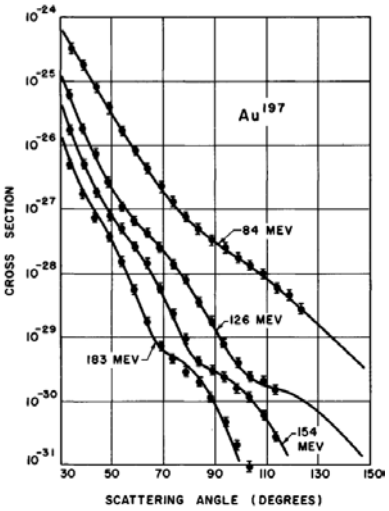

Figure 72: Differential cross section for elastic electron scattering in ^{197}Au and results from fits obtained by Hofstadter et al. [49].

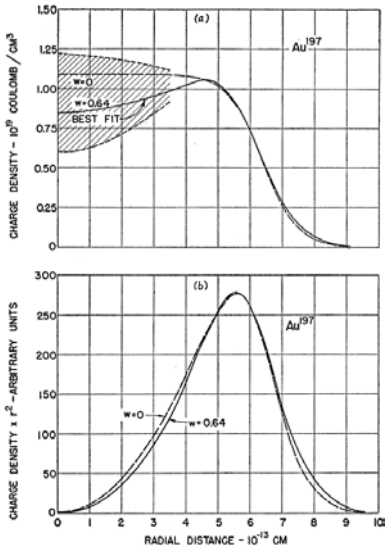

Figure 73: Charge distributions in gold obtained using the three-parameter Fermi shape, which allows variations in the charge density near the center. [49]

reaction cross section, the systematics of the N_{part} distribution and the error due to the modeling of the multiplicity distribution.

Nuclei configuration

The radial charge density distributions of nuclei are deduced from measured differential cross sections in low-energy electron-nucleus elastic scattering [49, 55]. It is also referred to as *electromagnetic size* of the nuclei and usually parameterized by a three-parameter Fermi distribution (3pF):

$$\rho(r) = \rho_0 \cdot \frac{1 + w(r/R)^2}{1 + \exp\left(\frac{r-R}{a}\right)} \tag{29}$$

where ρ_0 describes the nucleon density in the center of the nucleus, R is the radius parameter, a the diffuseness parameter and w characterizes the variation of the central charge density. The surface thickness t, where the density changes from 90% to 10% of the center density ρ_0, is related to the diffuseness parameter a by the relation $t = 4a \ln 3$ for the Fermi shape. An alternative form is the three-parameter Gaussian distribution (3pG):

$$\rho(r) = \rho_0 \cdot \frac{1 + w(r/R)^2}{1 + \exp\left(\frac{r^2-R^2}{a^2}\right)} \tag{30}$$

In both parametrizations a two-parameter form can be used with $w = 0$ (2pF and 2pG). Although the two-parameter Fermi, or Woods–Saxon, charge distribution modeled from electron scattering fits many nuclei well, the errors for R and a for the gold nucleus are quoted to be of the order of $\pm 1\%$. In comparison to very precise x-ray measurements of the transition energies in muonic atoms, the size of the gold nucleus in electron scattering experiments is underestimated by about 2%. In a systematic survey of nuclei radii [12] the RMS-radius of a gold nucleus was determined precisely with $\langle r^2 \rangle^{1/2} = 5.4358 \pm 0.0037$ fm.

The theoretical calculation based on Hartree-Fock (Density-Matrix Expansion) by Negele et al. [67, 73] and also by Lenske et al. [54] (included in GiBUU [26]) are also in agreement with muonic measurement and further on allow to calculate the neutron density distribution. The neutron density distribution measured with antiprotonic atoms [93] is quoted as the difference of the radii between the neutron and the proton distribution:

$$\Delta r_{pn} = 0.04 + 1.01 \cdot (N - Z)/A \tag{31}$$

In the Glauber MC calculations the neutron and proton weighted average is used as nuclear density distribution.

A compilation of all quoted parameters is summarized in table 15.

	shape	$\langle r^2\rangle^{1/2}$	ρ_0	t	R (fm)	a (fm)	w
Electron	2pF	5.33	1.09	2.35	6.38	0.535	–
Scattering [49]	2pG	5.31	1.13	2.61	6.36	2.72	–
	3pF	5.36	0.85	–	6.07	0.613	0.64
Muonic atom [43]	2pF	5.437		2.30	6.5541	0.523	–
DME calculation							
charge dist.	2pF	5.423			6.443	–	–
matter dist.	2pF	5.502			6.495	–	–
GiBUU [26]							
proton dist.	2pF	5.352			6.538	0.465	
neutron dist.	2pF	5.561			6.794	0.483	–
weighted average	2pF	5.527			6.691	0.476	–

Table 15: Fermi distribution parameters for ^{197}Au from electron scattering experiments. The errors are quoted for the radial parameters R and a to be around $\pm 1\%$ and for the surface thickness parameter t to be $\pm 5\%$ [49]. Theoretical calculations: Hartree-Fock calculations (Density-Matrix Expansion) by Negele et al. [67] taken from [73] and by Lenske et al. [54] included in GiBUU [26].

To model the correlation between the individual nucleons in the nuclei, a *hard-sphere exclusion* distance between the nucleons with $d_{min} = 0.9$ fm is used. In recent studies [9, 10] it was shown that a more realistic method based on a Metropolis random search to generate nuclei configuration constrained by their nuclear wave function gives comparable correlations in the nuclei.

To take also deformations of nuclei into account, the following modification of the two-parameter Fermi parameterization can be used

$$\rho(r,\theta) = \rho_0 \cdot \frac{1}{1+\exp\left(\frac{r-R_\theta}{a}\right)} \tag{32}$$

$$\text{with } R_\theta = R \cdot (1 + \beta_2 Y_{20}(\theta) + \beta_4 Y_{40}(\theta))\,, \tag{33}$$

where $Y_{20}(\theta)$ and $Y_{40}(\theta)$ are the spherical harmonics with the deformation parameters β_2 and β_4. The calculation [81] of the radial density distribution ($r^2\rho(r)$), with the parameter set given in table 14 for the spherical part and using in addition the parameters $\beta_2 = -0.131, \beta_4 = -0.031$ [66, 37] for the deformed gold nucleus, are shown in figure 74.

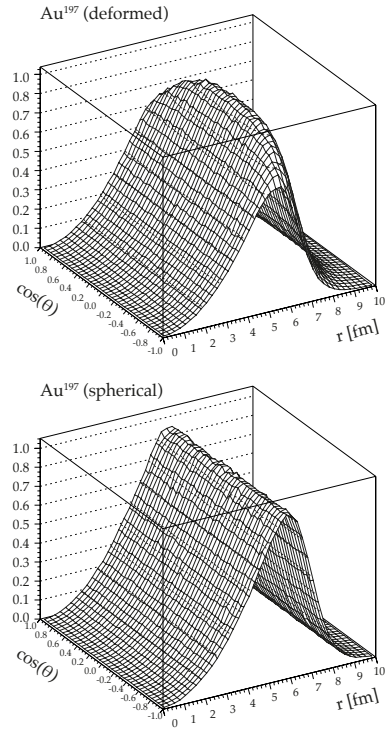

Figure 74: Calculation [81] of the radial density distribution ($r^2\rho(r)$) for the deformed and the spherical gold nucleus.

Nucleon-nucleon collision profile

In comparison to the high energy regime, where the contribution of inelastic process is the dominant part of the total nucleon-nucleon cross section and only weakly energy dependent, in the low energy range the total, elastic and inelastic cross section have rapidly changing excitation functions. A summary of the estimated proton-proton and neutron-proton cross sections at the beam energy of 1.23 GeV are listed in table 16. The values are obtained from the PDG [68], the ref. [28] and from GiBUU [26] (modified parameterization of Cugnon et al. [31] and refitted to the world data). With the assumption that nucleon-nucleon scatterings are isospin symmetric, the cross section for pp and nn and

cross sections (mb)			
σ_{tot}^{pp}	σ_{tot}^{np}	σ_{tot}^{NN}	
47.4	39.4	43.6	[68]
σ_{el}^{pp}	σ_{el}^{np}		
22.3	22.2		[26]
σ_{inel}^{pp}	σ_{inel}^{np}	σ_{inel}^{NN}	
25 ± 1	18 ± 3	21.6 ± 3	[26]
26.4 ± 0.2	21 ± 1	23.8 ± 2	[28]

Table 16: The total, elastic and inelastic pp, np and NN cross sections for 1.955 GeV/c nucleon momentum

as well for np and pn collisions can be treated to be equal.

$$\sigma^{pp} = \sigma^{nn}\,,\ \sigma^{np} = \sigma^{pn} \tag{34}$$

The isospin averaged nucleon-nucleon cross section can then be calculated by weighting over the number of protons and neutrons in the nuclei[6]:

$$\sigma^{NN} = (Z_p Z_t \sigma^{pp} + N_p N_t \sigma^{nn} + (Z_p N_t + N_p Z_t)\sigma^{np})/(A_p A_t)\,. \tag{35}$$

It should be emphasized that the cross sections in the nuclei (*in-medium*)

[6] for gold with $Z = 79$ $N = 118$ and $A = 197$ the formula simplifies to:

$$\sigma^{NN} = 0.52 \cdot \sigma^{pp} + 0.48 \cdot \sigma^{np}$$

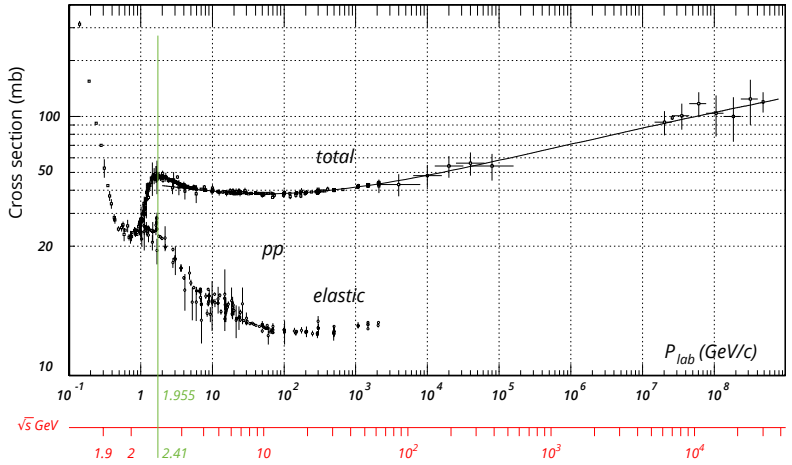

Figure 75: The proton-proton total and elastic cross section [68].

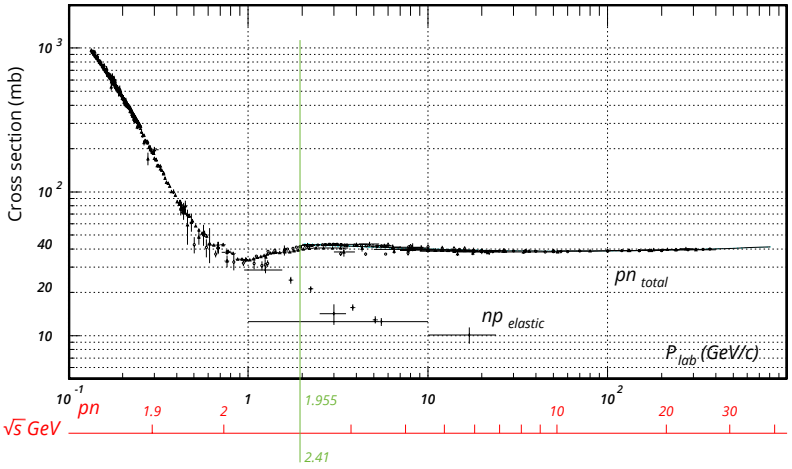

Figure 76: The neutron-proton total and elastic cross section [68].

may differ from the free space cross section due to density dependencies and further on may be modified due to the internal Fermi motion and the Pauli exclusion principle (*Pauli blocking*) [18]. In the following, this effects are neglected and the nucleons in the nucleus are treated as free particles. In the energy regime of 1.23 GeV the inelastic and elastic

cross section are nearly similar. In the picture of successive nucleon scatterings in the nuclei (*cascade model*) it would be questionable to use the same cross section for all inelastic collisions. The traversing nucleons could lose their momentum due to initial elastic scattering and would thus have in a subsequent inelastic scattering a much smaller inelastic cross section. To account for this, the effective interaction cross section between colliding nucleons can be modeled with the *profile function approach*, were the probability and range of an effective nucleon-nucleon interaction can be adjusted in terms of the inelastic and total cross section.

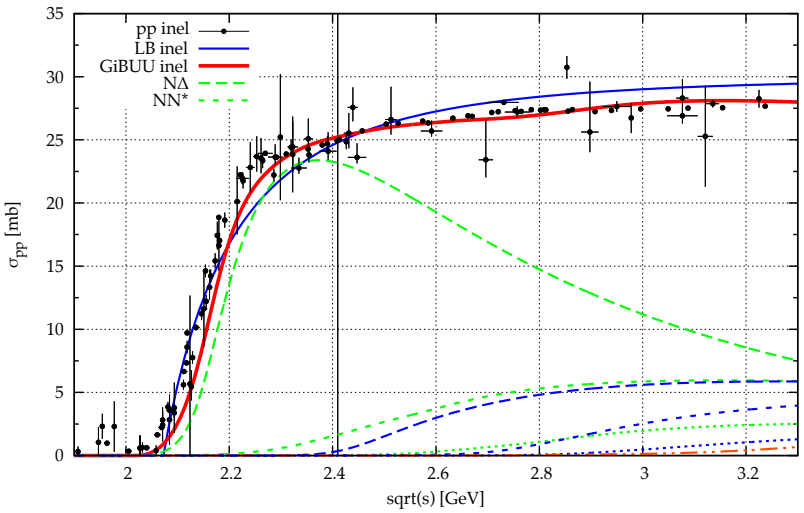

Figure 77: The proton-proton inelastic cross section obtained from PDG data [68] compared to a parameterization by GiBUU [26] and Landolt-Börnstein [13].

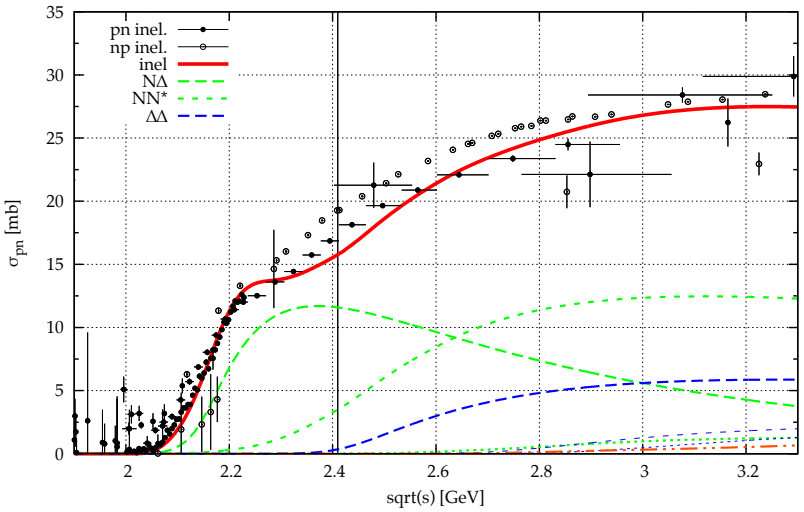

Figure 78: The neutron-proton and proton-neutron inelastic cross section obtained from PDG data [68] compared to a parameterization by GiBUU [26].

Calculated quantities

In the standard approach the centrality of a collision, defined by the impact parameter, is estimated via the relation of geometrical quantities, calculable by the Glauber Model, and measurable observables. And since neither the impact parameter nor geometrical quantities, such as the number of participating nucleons N_{part} or binary collision N_{coll}, shown in figure 79, are directly measurable, they are called *pseudo-observables* [44]. Their connection to experimental observables is made

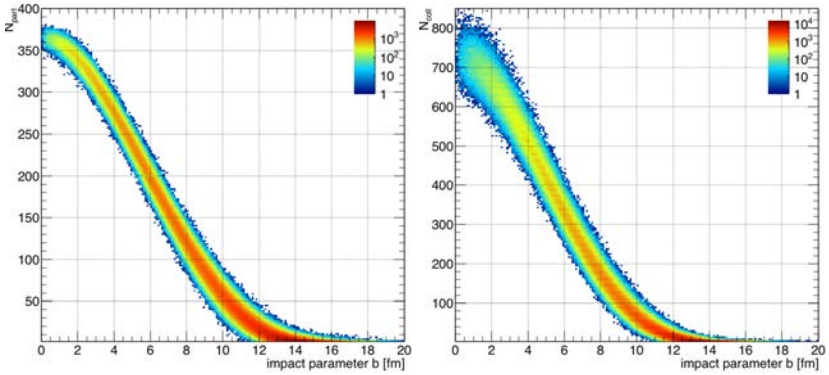

Figure 79: The correlation plot of between the impact-parameter b and the N_{part} distribution (left) and the N_{coll} distribution from Glauber MC.

using the assumption that particle production in heavy-ion collisions scales monotonically. Therefore observables, like the average charged-particle multiplicity N_{ch} and the transverse Energy E_T are increasing towards more central collisions, corresponding to decreasing impact parameter. For the most central events with a zero impact parameter,

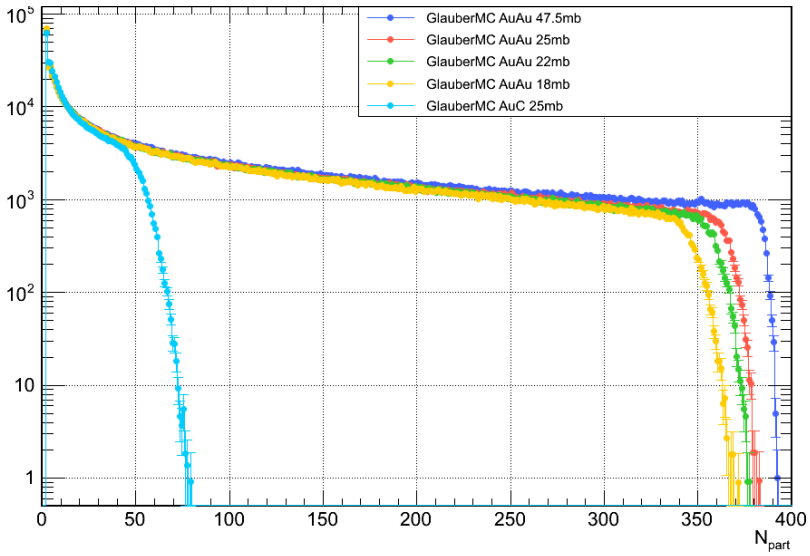

Figure 80: N_{part} distribution in AuAu reaction with an NN cross section σ_{NN} of (■) 47.5 fm (■) 25 fm (■) 22 fm (■) 18 fm, in comparison to the collision system Gold-Carbon (■) AuC with 25 fm.

the maximum of particle production is reached. In the geometrical picture, the volume of the initial overlap region scales by the number of

participating nucleons N_{part}. Following this view, the emission spectra and particle production is directly related in the *fireball model* [47, 99] to the available kinetic energy per participating nucleon in a certain reaction volume. In the *wounded-nucleon model* [19] it is assumed that the multiplicity distribution of produced particles is the incoherent superposition of the multiplicity distributions of each individual initial wounded nucleon, also scaling with the number of participating nucleons. Using the number of participating nucleons, as shown in

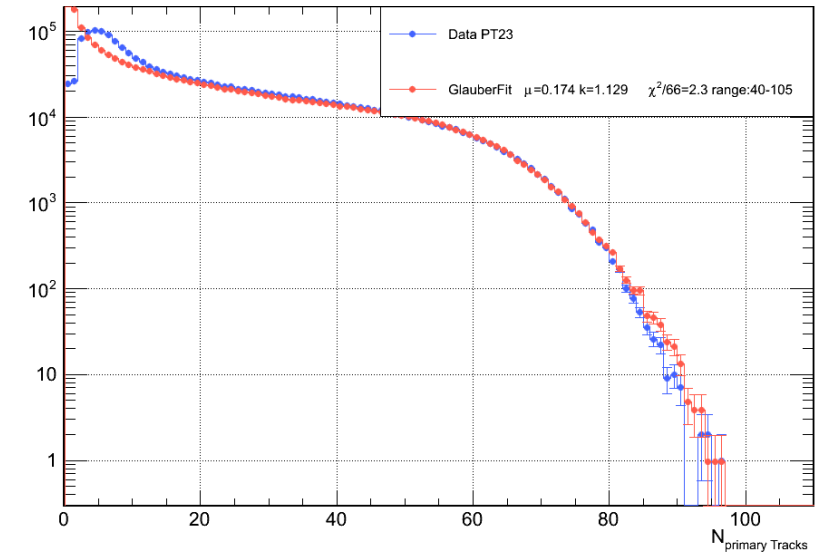

Figure 81: The uncorrected N_{ch} multiplicity-distribution determinated by the number of *primary tracks*. Shown are (■) minimum-bias data and the (■) Glauber-fit with $\mu = 0.174$ $k = 1.129$.

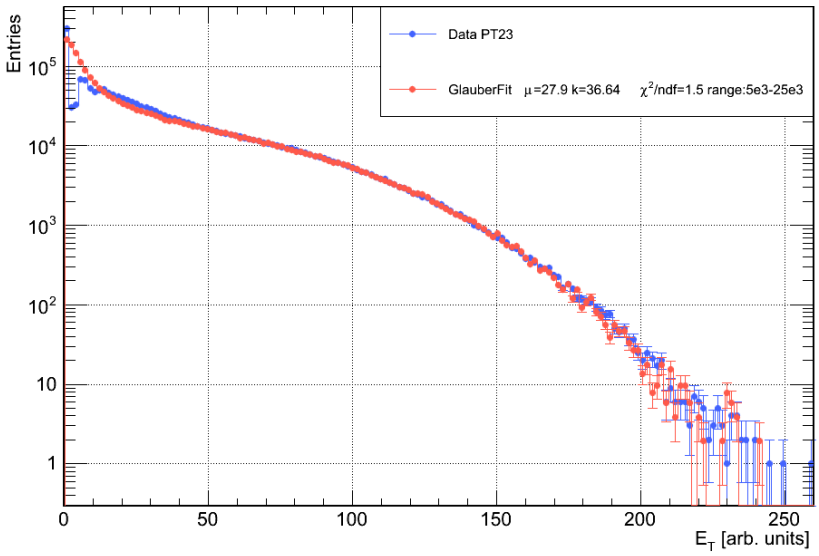

Figure 82: The uncorrected E_t distribution. Shown are (■) minimum-bias data and the (■) Glauber-fit with $mu = 27.9$ $k = 36.6$.

figure 80, as scaling factor with a convolution of a simple model for particle production, the multiplicity distribution can be calculated. As a model for particle production the negative binomial distribution (NBD) is commonly used in the high energy regime [1, 90, 5], but for the

beam energies considered here the Gaussian distribution gave sufficient results. In the Glauber MC calculation N_{ch} or E_T is calculated for each event by sampling from a Gaussian distribution with a mean and sigma of:

$$N_{mean} = \mu \cdot N_{part} \ , \ \sigma = k \cdot \sqrt{\mu \cdot N_{part}} \tag{36}$$

The parameters μ and k are determined by a minimization procedure, which compares an ensemble of various simulated multiplicity distributions with the measured one, called *Glauber-Fit*. Using this fit method the efficiency, the acceptance and the fluctuations of the detector response are also taken into account. In figure 81 the uncorrected N_{ch}-spectra is shown, determinated by the number of *primary tracks*, and in figure 82 the uncorrected transverse Energy E_t distribution, both with the corresponding simulated distribution by the Glauber-Fit.

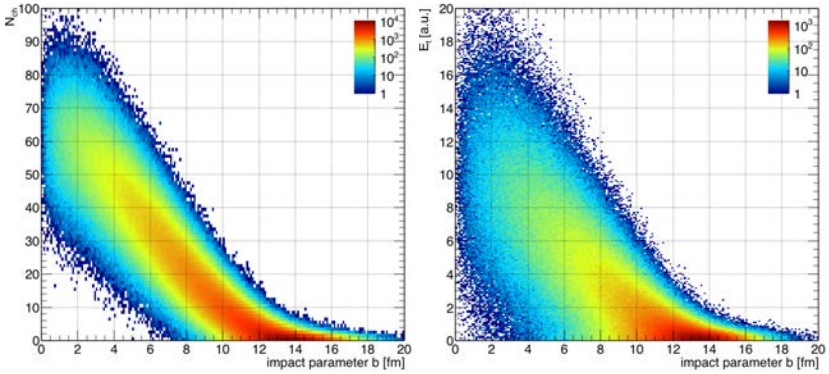

Figure 83: The correlation plot of between the estimated impact-parameter b and N_{ch} ($N_{primaryTracks}$ on the left) and E_t (right).

Going to larger impact parameters the collisions are getting more peripheral and the number of spectator nucleons, $N_{spec} = 2 \cdot A - N_{part}$, is rising. In the forward region the number of participating nucleons can be estimated with:

$$N_{part} = 2 \cdot A \left(1 - Z_{spec}/Z\right) \ , \tag{37}$$

where Z and A are the nuclear charge and mass of a symmetric collision system and Z_{spec} is the measured total charge of the projectile spectators [51, 23]. Due to the fragmentation process of the spectator nucleons the multiplicity of spectators in peripheral reactions is not directly connected to the centrality anymore, whereas their charge is a conserved quantity. The other method used in the forward region is the measurement of the deposited energy of spectators near zero-degree to the beam direction by a *zero-degree calorimeter* (ZDC). The *total reaction cross section* is calculated by the Glauber MC with the maximal geometrical cross section of the initially used impact parameter range (b_{max}), corrected by the fraction of events with at least one nucleon-nucleon

collision to the total number of events:

$$\sigma_{tot} = \frac{N_{reaction}(N_{coll} \geq 1)}{N_{total}(N_{coll} \geq 0)} \times \pi b_{max}^2 \,, \tag{38}$$

The correlation between the impact-parameter b, respectivly N_{part}, and the obtained multiplicity distribution is used in the following to obtain centrality classes. By taking fractions of the total cross section, defined as centrality percentiles, the corresponding centrality classes with their averaged values for impact parameter $\langle b \rangle$ and $\langle N_{part} \rangle$ are determined. In the data analysis events are sorted into N_{ch} or E_T intervals, estimated for each centrality class. The centrality estimation has, due to the fluctuating nature of event multiplicities, its limitation. Its accuracy and resolution can be checked by simulation and comparison between different estimator. Beside the pseudo-observables N_{part} and N_{coll} other derived quantities can be calculated:

- $T_{AB} = \langle N_{coll} \rangle / \sigma_{NN}$ - the nuclear overlap function [34] is used to calculate the nuclear modification factor by the scaling of elementary pp reaction to pA and AA reaction with the number of binary collision. The idea is to quantify *in-medium modifications* in comparison to elementary reaction in terms of the superposition of individual elementary binary collisions.

- $v_{coll}(t)$ - the frequency of binary collision, calculated from the collision time of each binary collision $t = |z_1 - z_2| / (2v_0)$ with z_1 and z_2 being the longitudinal coordinates of the participant nucleons with $t = 0$ in the center-of-mass frame [94]

- $dN_{ch}/d\eta$ and $dE_T/d\eta$ - estimation for the centrality dependent multiplicity density and transverse energy density within a phenomenological approach

In ref [6] the first observation of higher-order collective flow is described by the anisotropic and fluctuating shape of the overlap region. The approach to map *flow observables*, like elliptic or triangular flow, to their corresponding *pseudo-observable*, calculated from Glauber MC, like eccentricity, can reveal the response of the nuclear medium to initial anisotropies. In figure 84 the shape and orientation of the overlap region is characterized by the overlap area S, the participant eccentricity ϵ_{part} and plane angle ψ_{pp} using the spatial distribution of all participating nucleons. With the mean $\langle x \rangle, \langle y \rangle$ and the variance σ_x^2, σ_y^2 of the spatial distribution in x- and y-direction and their covariance $\sigma_{xy}^2 = \langle xy \rangle - \langle x \rangle \cdot \langle y \rangle$ following the notation of the ref. [7, 91] the reaction plane eccentricity ϵ_{RP} and the participant eccentricity ϵ_{part} with

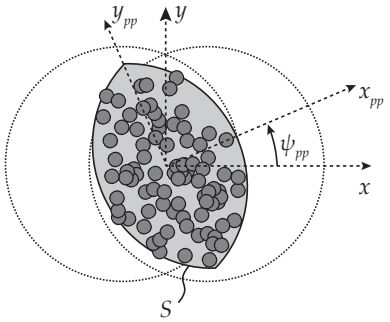

Figure 84: The overlap area S of the participating nucleons, the participant eccentricity ϵ_{part} and plane angle ψ_{pp} calculated with the Glauber MC.

the corresponding area of overlap in the transverse plane are:

$$\epsilon_{RP} = \frac{\sigma_y^2 - \sigma_x^2}{\sigma_y^2 + \sigma_x^2} \, , \; \epsilon_{part} = \frac{\sqrt{(\sigma_y^2 - \sigma_x^2)^2 + 4\sigma_{xy}^2}}{\sigma_y^2 + \sigma_x^2} \, , \; S = \pi \sqrt{\sigma_x^2 \sigma_y^2 - \sigma_{xy}^2}$$

The reaction plane eccentricity ϵ_{RP} is fixed in the reference frame and participant eccentricity ϵ_{part} tilted by the participant-plane angle w.r.t. the reaction plane (see fig. 85):

$$\psi_{pp} = -\frac{\sigma_{xy}}{\frac{1}{2}\left(\sigma_y^2 - \sigma_x^2\right) + \sqrt{(\sigma_y^2 - \sigma_x^2)^2 + 4\sigma_{xy}^2}}$$

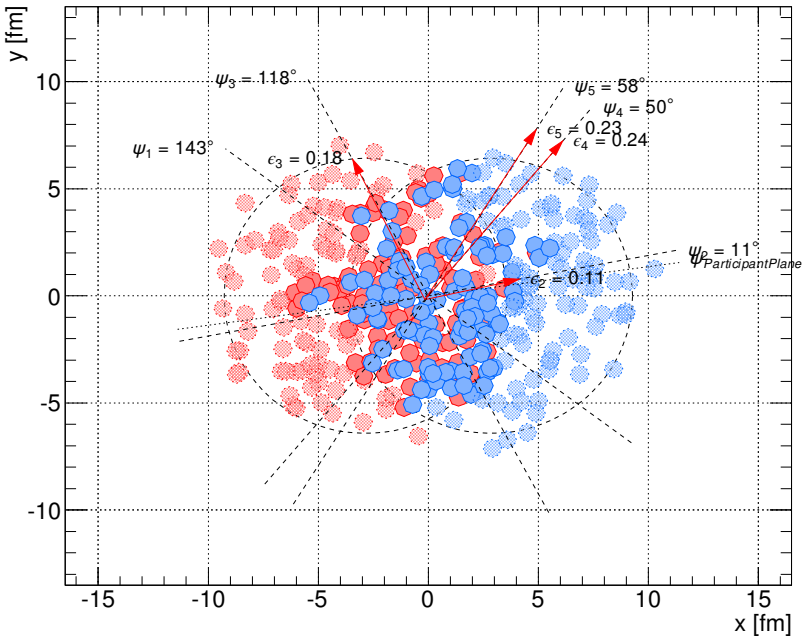

Figure 85: Event display of one Glauber MC event with an impact parameter $b = 5.7$ fm. The anisotropic shape of the overlapping region of two gold nuclei is shown, where the dashed circles indicates the radius parameter R. The participating nucleons are plotted as full colored dots, the spectators as light colored dots and their size corresponds to the nucleon-nucleon cross section σ_{NN}. The participant plane ψ_{pp} and its harmonic decompositions into high-order phase angles ψ_n is shown, also the corresponding moments ϵ_n of the initial participant eccentricity.

For a harmonic decomposition of the spatial fluctuations, the high-order moments of the initial participant eccentricity ϵ_n:

$$\epsilon_n \equiv -\frac{\langle r^n \cos n(\phi - \psi_n) \rangle}{\langle r^n \rangle} \tag{39}$$

and their phase angles ψ_n are described in the following way:

$$\psi_n \equiv \text{atan2}(\langle r^n \sin n\phi \rangle, \langle r^n \cos n\phi \rangle) + \frac{\pi}{n} \, . \tag{40}$$

Total reaction cross section

For reference, the values for the total reaction cross sections from various models are listed in table 17. The values are obtained from the sharp-cut approximation and the Vary et al.-parameterization. The analytical soft-sphere model by Karol [59, 24] and two Glauber Model calculation are shown as well. The *GSI Overlap* [70] uses the analytical optical-limit version of the Glauber Model scattering formula to obtain the reaction cross section by integrating over a smooth nuclear density distribution. The *DIAGEN Glauber* [84, 69] is comparable with our Glauber MC with the difference that here the *profile function approach* is used for the nucleon-nucleon interaction. All models are comparable within their systematic errors, as quoted in the references or obtained by variating the model parameter range. Additionally, the reaction

method & reference	parameter	total cross section (mb)
Sharp-cut (eq. 21) KaoS [95]	$r_0 = 1.27$ fm	6862
Parameterization (eq. 24) [2]	$r_0 = 1.33 \pm 0.04$ fm $b_0 = 0.85 \pm 0.1$	7153 ± 335
Karol [59, 24] code: [29]	$\sigma_{tot}^{pp} = 47.4 \pm 2$ mb $\sigma_{tot}^{np} = 39.35 \pm 2$ mb	6899 ± 40
GSI Overlap [70] modified	$\sigma_{inel}^{NN} = 23.8 \pm 2$ mb	6758 ± 70
DIAGEN Glauber [84, 69]	$\sigma_{tot}^{NN} = 43.6 \pm 2$ mb $\alpha = -0.2 \pm 0.2$ $B = 5.97 \pm 2$ (GeV/c)$^{-2}$	6950 ± 148
UrQMD 3.4 [16, 20]		6947 ± 56 (stat)

Table 17: The total reaction cross section for Au+Au collisions at 1.23 AGeV, calculated from the sharp-cut approximation (eq. 21) with values used by KaoS [95], the Vary et al.-parameterization (eq. 24) with parameters and errors from [2], the analytical soft-sphere model by Karol [59, 24] and two Glauber Model calculations are listed. The *GSI Overlap* [70] and the *DIAGEN Glauber* [84, 69] are modified to have a similar radius parameter R as in the Glauber MC calculation. The results of the transport model *UrQMD* in the cascade mode [16, 20] were obtained with the maximal impact parameter range of $b_{max} = 20$ fm. The UrQMD-code was modified to calculate for each event a new nuclei configuration.

cross section is calculated from the transport model *UrQMD* [16, 20] by extending the implemented impact parameter range up to $b_{max} = 20$ fm and correcting the geometrical cross section by the fraction of events with at least one nucleon-nucleon collision (see figure 67):

$$\sigma_{tot} = N_{reaction} / N_{total} \times \pi b_{max}^2 \, . \tag{41}$$

To estimate the systematic error of the total reaction cross section σ_{tot}^{AuAu} for Au+Au at 1.23 AGeV with the Glauber MC approach, the energy-dependent parameter, the nucleon-nucleon cross section, and the parameters for the generation of the nuclei are varied independently. In figure 86 the effect of changing the nucleon-nucleon cross section σ_{NN} on the calculated σ_{tot}^{AuAu} is shown. Above 20 mb a linear dependence is visible, where a variation of $\pm 20\%$ of σ_{NN} results in an error of $1 - 2\%$ for σ_{tot}^{AuAu}. Below 20 mb the borders of the nuclei start to get transparent, leading to a rapid decrease of σ_{tot}^{AuAu} towards smaller σ_{NN}. In figure 87 the dependence of σ_{tot}^{AuAu} on the relative change of the parameters used

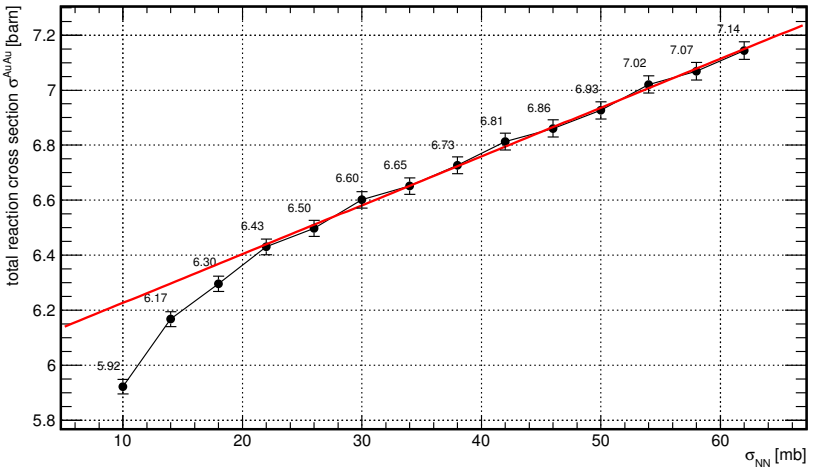

Figure 86: The total reaction cross-sections as a function of the nucleon-nucleon cross section σ_{NN} with the parameter $R = 6.554$ fm, $a = 0.523$ fm and $d = 0$. Above 20 mb a linear dependence and below a rapid decrease of σ_{tot}^{AuAu} is visible. An error of $1 - 2\%$ for σ_{tot}^{AuAu} is estimated for a variation of $\pm 20\%$ of σ_{NN}.

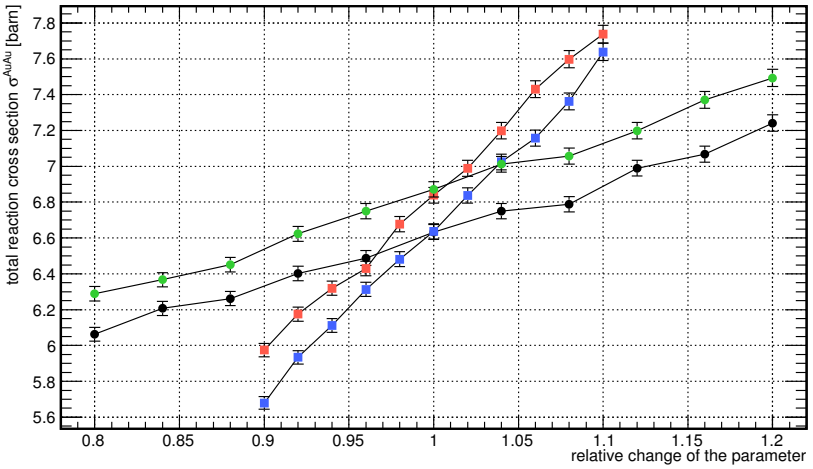

Figure 87: The total reaction cross-sections σ_{tot}^{AuAu} as a function of the relative change of the parameter $R = 6.554$ fm and $a = 0.523$ fm, with a fixed $\sigma_{NN} = 23.8$ mb.
(●) $a \pm 20\%$ with $d = 0.0$
(●) $a \pm 20\%$ with $d = 0.9$
(■) $R \pm 10\%$ with $d = 0.0$
(■) $R \pm 10\%$ with $d = 0.9$

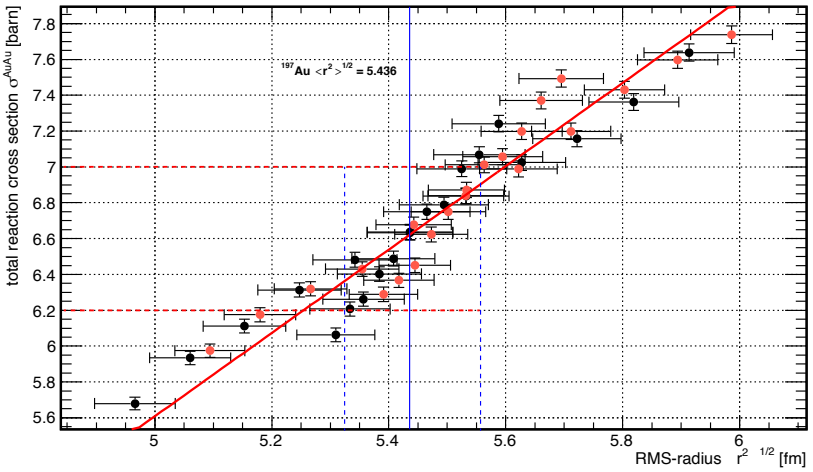

Figure 88: The total reaction cross-sections as a function of the RMS-radius of the generated nuclei, calculated with fixed $\sigma_{NN} = 23.8$ mb (●) $d = 0.0$ and (●) $d = 0.9$. The mean-values of the RMS-radius distributions of all generated nuclei and the one sigma deviation (shown as error bars) are plotted. The error of the total reaction cross-sections is only the statistical one. The RMS-radius of ^{197}Au $\langle r^2 \rangle^{1/2} = 5.436$ fm is also shown as blue line. Accounting only calculations constrained by the RMS-radius with an maximal deviation of 2% (shown by the dashed blue lines) the uncertainty is estimated to be 6%.

in the creation of the nuclei, R and a, and additionally the influence of two assumptions on the inter-nuclear distance-parameter $d = 0$ fm and $d = 0.9$ fm are shown. As previously discussed, the increase of the distance-parameter d results in a growth of the nuclei and gives an error of around $3 - 4\%$ for σ_{tot}^{AuAu}. Although the used parameter-range of $R \pm 10\%$ and $a \pm 20\%$ are extreme, the resulting systematic error is only around 6%, if the result is constrained by the calculation of the RMS-radius of all generated nuclei, shown in figure 88. For each calculation shown in figure 87, the mean-value and the one sigma deviation of the RMS-radius distribution of all generated nuclei are plotted. With the condition that the RMS-radius of ^{197}Au is measured with $\langle r^2 \rangle^{1/2} = 5.436$ fm and taking only calculation into account with an maximal deviation of 2% around the RMS-radius, an uncertainty of 6% can be estimated. The σ_{tot}^{AuAu} is than estimated to be 6650 mb for the inelastic case of $\sigma_{NN} = 23.8$ mb and 7016 mb for the total nucleon-nucleon cross section of $\sigma_{NN} = 43.6$ mb. For a realistic scenario and in agreement with the reference values for the total reaction cross section given in table 17, an effective nucleon-nucleon cross section of around $\sim 25 - 30$ mb seems to be a robust approximation. Taking in to account the systematic uncertainties, summed up in table 18, an estimate for the total reaction cross section and its error is:

$$\sigma_{tot}^{AuAu} = (6833 \pm 430) \text{ mb} .$$

Parameter	Variation	Error
$\Delta\sigma_{NN}$	$\pm 20\%$	$1 - 2\%$
Δd_{min}	$\pm 100\%$	$(3 - 4\%)$
ΔR	$\pm 10\%$	
Δa	$\pm 20\%$	
constrained by RMS-radius		$\sim 6\%$
Quadratic addition		$\sim 6.3\%$

Table 18: The systematic error of the total reaction cross section obtained by variation of the model parameters.

Centrality classes

There are three contributions to the systematic error of the determination of *centrality classes*, which have to be considered. Since centrality

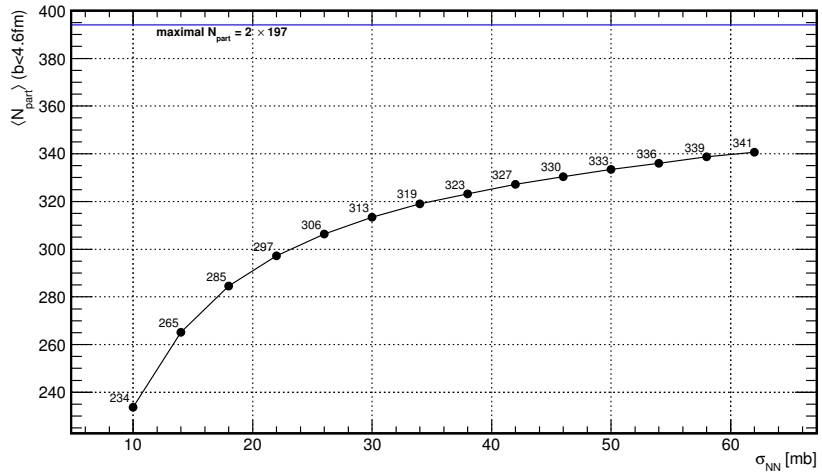

Figure 89: The mean $\langle N_{part} \rangle$ for the most central bin ($b < 4.6$ fm, $\sim 10\%$) as a function of the nucleon-nucleon cross section of σ_{NN}.

classes are defined as the fraction of total cross section, an uncertainty of the total reaction cross section contributes as a systematic shift of

the centrality class intervals. The second uncertainty has its origin in the uncertainty of the model parameters, resulting into an spread of differed N_{part} distributions w.r.t. the default distribution. For the most central 10% bin ($b < 4.6$ fm), the systematic change of $\langle N_{part} \rangle$ due to the increase of the nucleon-nucleon cross section is shown in figure 89.

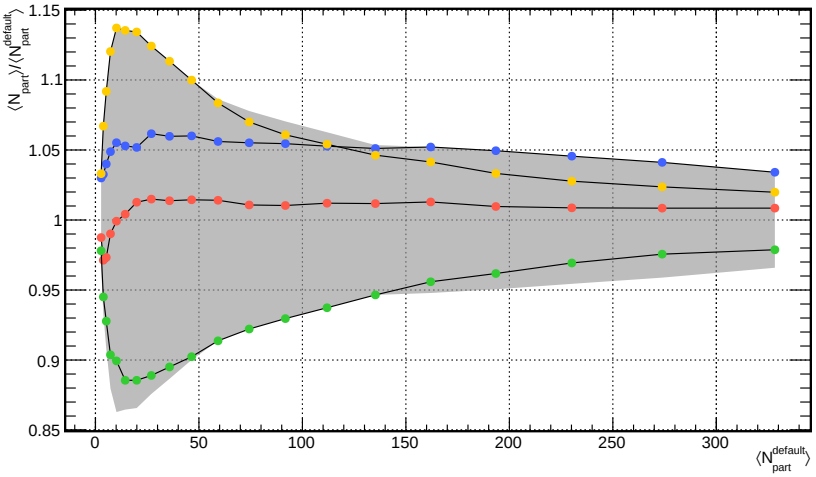

Figure 90: The radio of the mean $\langle N_{part} \rangle$ to the value of the default calculation as function of the default N_{part}, with four different variation of the model parameters: (●) $\sigma_{NN} = 30$ mb (●) $d = 0.9$ (●) $R = 6.75, a = 0.623$ (●) $R = 6.35, a = 0.423$. The gray band indicates the maximum deviation to the default result.

In figure 90 the radio of the mean $\langle N_{part} \rangle$ to the value of the default calculation as function of default $\langle N_{part} \rangle$ per centrality percentile is shown and in figure 91 the same as a function of the centrality percentile.

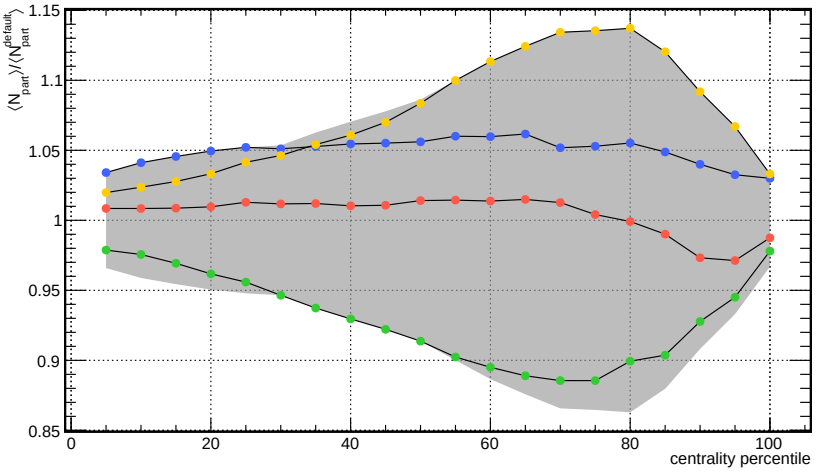

Figure 91: Same plot as in 90, but sorted as function of centrality percentile. The gray band indicates the maximum deviation to the default result in each centrality percentile.

The maximal deviation from the default result at each centrality percentile is used as the estimated error for $\langle N_{part} \rangle$, shown as grey band in figure 90 and 91 and can be parameterized as:

$$\Delta N_{part}^{max} / N_{part} = 0.03 + 3.4 / N_{part} \ .$$

The uncertainty on N_{part} rises from 3.4% in the most central collisions up to 14% in peripheral ($70 - 80\%$) and for minimum bias ($0 - 100\%$)

collisions it is calculated to be 5% (see tab. 19). A third error arises due to the event-by-event fluctuation of the N_{part} values w.r.t. to a certain centrality and can be described as the dispersion for each centrality percentile, shown as $\sigma(N_{part})$ in table 19. This error is accounted for after the MC simulation of the detector response N_{ch}, where the dispersion of N_{part} is preserved, while due to the sampling process an additional dispersion is introduced in the N_{ch} distribution.

class	b_{min}	–	b_{max}	$\langle N_{part} \rangle$	*syst.error*	(%)	$\sigma(N_{part})$	(%)
$0-100$	0.00	–	17.93	91.7	$\pm$4.4	4.7	96.7	105.5
$0-10$	0.00	–	4.60	301.1	$\pm$11.2	3.7	32.6	10.8
$10-20$	4.60	–	6.50	211.8	$\pm$10.1	4.8	23.1	10.9
$20-30$	6.50	–	7.95	148.5	$\pm$7.8	5.3	18.2	12.3
$30-40$	7.95	–	9.18	101.7	$\pm$6.3	6.2	15.2	15.0
$40-50$	9.18	–	10.27	66.6	$\pm$5.4	8.1	12.9	19.3
$0-5$	0.00	–	3.25	328.3	$\pm$11.2	3.4	19.4	5.9
$5-10$	3.25	–	4.60	273.8	$\pm$11.3	4.1	16.4	6.0
$10-15$	4.60	–	5.62	230.2	$\pm$10.5	4.6	14.6	6.3
$15-20$	5.62	–	6.50	193.5	$\pm$9.6	4.9	13.4	7.0
$20-25$	6.50	–	7.26	162.0	$\pm$8.4	5.2	12.6	7.8
$25-30$	7.26	–	7.95	135.3	$\pm$7.2	5.4	12.0	8.9
$30-35$	7.95	–	8.58	111.9	$\pm$7.0	6.3	11.6	10.4
$35-40$	8.58	–	9.17	91.8	$\pm$6.5	7.0	11.2	12.2
$40-45$	9.17	–	9.73	74.3	$\pm$5.8	7.8	10.7	14.4
$45-50$	9.73	–	10.26	59.2	$\pm$5.1	8.6	10.2	17.3
$50-55$	10.26	–	10.76	46.5	$\pm$4.6	10.0	9.6	20.7
$55-60$	10.76	–	11.24	35.8	$\pm$4.1	11.3	8.9	24.8
$60-65$	11.24	–	11.70	27.0	$\pm$3.4	12.4	8.1	29.9
$65-70$	11.70	–	12.14	19.9	$\pm$2.7	13.4	7.2	36.0
$70-75$	12.14	–	12.57	14.4	$\pm$1.9	13.5	6.2	43.1
$75-80$	12.57	–	13.00	10.2	$\pm$1.4	13.7	5.1	50.4

Table 19: Results of the Glauber MC calculation for Au+Au collisions at 1.23 AGeV, with the impact-parameter intervals $b_{min} - b_{max}$ (in fm), the mean $\langle N_{part} \rangle$ and its systematic uncertainty, and the one sigma deviation $\sigma(N_{part})$ in each centrality bins.

Bibliography

[1] T. Abbott et al. "Measurement of energy emission from O+A and p+A collisions at 14.5 GeV/c per nucleon with a lead-glass array". In: *Physics Letters B* 197.1–2 (1987), pp. 285 –290. ISSN: 0370-2693. DOI: 10.1016/0370-2693(87)90385-6.

[2] E.O. Abdrahmanov et al. "Interaction cross sections and negative pion multiplicities in nucleus-nucleus collisions at 4.2 GeV/c per nucleon". In: *Zeitschrift für Physik C Particles and Fields* 5.1 (1980), pp. 1–8. ISSN: 0170-9739. DOI: 10.1007/BF01546951. URL: http://dx.doi.org/10.1007/BF01546951.

[3] B. Abelev and other. "Centrality determination of Pb-Pb collisions at $\sqrt{s_{NN}} = 2.76$ TeV with ALICE". In: *Phys. Rev. C* 88 (4 Oct. 2013), p. 044909. DOI: 10.1103/PhysRevC.88.044909.

[4] S. S. Adler and other. "Systematic studies of the centrality and $\sqrt{s_{NN}}$ dependence of the $dE_T/d\eta$ and $dN_{\mathrm{ch}}/d\eta$ in heavy ion collisions at midrapidity". In: *Phys. Rev. C* 71 (3 Mar. 2005), p. 034908. DOI: 10.1103/PhysRevC.71.034908.

[5] S. S. Adler et al. "Measurement of density correlations in pseudorapidity via charged particle multiplicity fluctuations in Au+Au collisions at $\sqrt{s_{NN}} = 200$ GeV". In: *Phys. Rev. C* 76 (3 Sept. 2007), p. 034903. DOI: 10.1103/PhysRevC.76.034903.

[6] B. Alver and G. Roland. "Collision-geometry fluctuations and triangular flow in heavy-ion collisions". In: *Phys. Rev. C* 81 (5 May 2010), p. 054905. DOI: 10.1103/PhysRevC.81.054905.

[7] B. Alver et al. "Importance of correlations and fluctuations on the initial source eccentricity in high-energy nucleus-nucleus collisions". In: *Phys. Rev. C* 77 (1 Jan. 2008), p. 014906. DOI: 10.1103/PhysRevC.77.014906.

[8] B. Alver et al. "The PHOBOS Glauber Monte Carlo". In: (2008). arXiv:0805.4411 [nucl-ex]. URL: http://tglaubermc.hepforge.org/.

[9] M. Alvioli, H.J. Drescher, and M. Strikman. "A Monte Carlo generator of nucleon configurations in complex nuclei including nucleon–nucleon correlations". In: *Physics Letters B* 680.3 (2009), pp. 225 –230. ISSN: 0370-2693. DOI: 10.1016/j.physletb.2009.08.067.

[10] M. Alvioli et al. "Initial-state anisotropies and their uncertainties in ultrarelativistic heavy-ion collisions from the Monte Carlo Glauber model". In: *Phys. Rev. C* 85 (3 Mar. 2012), p. 034902. DOI: 10.1103/PhysRevC.85.034902.

[11] M. Alvioli et al. "Initial state anisotropies in ultrarelativistic heavy-ion collisions from the Monte Carlo Glauber model". In: *PoS* QNP2012 (2012), p. 172. arXiv:1206.5720 [hep-ph].

[12] I. Angeli. "A consistent set of nuclear rms charge radii: properties of the radius surface R(N,Z)". In: *Atomic Data and Nuclear Data Tables* 87.2 (2004), pp. 185 –206. ISSN: 0092-640X. DOI: 10.1016/j.adt.2004.04.002.

[13] A. Baldini et al. *Subvolume B*. SpringerMaterials - The Landolt-Börnstein Database. DOI: 10.1007/10367917_14. URL: http://materials.springer.com/lb/docs/sm_lbs_978-3-540-47956-7_14.

[14] Saul Barshay, C. B. Dover, and J. P. Vary. "Nucleus-nucleus cross sections and the validity of the factorization hypothesis at intermediate and high energies". In: *Phys. Rev. C* 11 (2 Feb. 1975), pp. 360–369. DOI: 10.1103/PhysRevC.11.360.

[15] J. Bartke. *Introduction to Relativistic Heavy Ion Physics*. World Scientific, 2009. ISBN: 9789810212315. URL: http://books.google.de/books?id=WMGZngEACAAJ.

[16] S.A. Bass et al. "Microscopic models for ultrarelativistic heavy ion collisions". In: *Progress in Particle and Nuclear Physics* 41 (1998), pp. 255 –369. ISSN: 0146-6410. DOI: 10.1016/S0146-6410(98)00058-1.

[17] C. J. Benesh, B. C. Cook, and J. P. Vary. "Single nucleon removal in relativistic nuclear collisions". In: *Phys. Rev. C* 40 (3 Sept. 1989), pp. 1198–1206. DOI: 10.1103/PhysRevC.40.1198.

[18] C. A. Bertulani and C. De Conti. "Pauli blocking and medium effects in nucleon knockout reactions". In: *Phys. Rev. C* 81 (6 June 2010), p. 064603. DOI: 10.1103/PhysRevC.81.064603.

[19] A. Białas, M. Bleszyński, and W. Czyż. "Multiplicity distributions in nucleus-nucleus collisions at high energies". In: *Nuclear Physics B* 111.3 (1976), pp. 461 –476. ISSN: 0550-3213. DOI: 10.1016/0550-3213(76)90329-1.

[20] M Bleicher et al. "Relativistic hadron-hadron collisions in the ultra-relativistic quantum molecular dynamics model". In: *Journal of Physics G: Nuclear and Particle Physics* 25.9 (1999), p. 1859. URL: http://stacks.iop.org/0954-3899/25/i=9/a=308.

[21] J.D. Bowman, W.J. Swiatecki, and C.F. Tsang. "Abrasion and Ablation of Heavy Ions". In: (1973). URL: http://escholarship.org/uc/item/8nm3b276.

[22] H. L. Bradt and B. Peters. "The Heavy Nuclei of the Primary Cosmic Radiation". In: *Phys. Rev.* 77 (1 Jan. 1950), pp. 54–70. DOI: 10.1103/PhysRev.77.54.

[23] D. Brill. "Azimutal anisotrope Teilchenemission in relativistischen Schwerionenstössen". Dissertation. Goethe-Universitaet Frankfurt, 1993.

[24] T. Brohm and K.-H. Schmidt. "Statistical abrasion of nucleons from realistic nuclear-matter distributions". In: *Nuclear Physics A* 569.4 (1994), pp. 821 –832. ISSN: 0375-9474. DOI: 10.1016/0375-9474(94)90386-7.

[25] Wojciech Broniowski and Maciej Rybczy ński. "Two-body nucleon-nucleon correlations in Glauber models of relativistic heavy-ion collisions". In: *Phys. Rev. C* 81 (6 June 2010), p. 064909. DOI: 10.1103/PhysRevC.81.064909.

[26] O. Buss et al. "Transport-theoretical description of nuclear reactions". In: *Physics Reports* 512.1–2 (2012). Transport-theoretical Description of Nuclear Reactions, pp. 1 –124. ISSN: 0370-1573. DOI: 10.1016/j.physrep.2011.12.001.

[27] Micah Buuck and Gerald A. Miller. "Corrections to the eikonal approximation for nuclear scattering at medium energies". In: *Phys. Rev. C* 90 (2 Aug. 2014), p. 024606. DOI: 10.1103/PhysRevC.90.024606.

[28] Bystricky, J. et al. "Energy dependence of nucleon-nucleon inelastic total cross-sections". In: *J. Phys. France* 48.11 (1987), pp. 1901–1924. DOI: 10.1051/jphys:0198700480110190100.

[29] "Code for calculating the total nuclear cross sections in the Karol Model". In: (). URL: http://www-win.gsi.de/charms/karol.htm.

[30] Francis A. Cucinotta, John W. Wilson, and R. K. Tripathi. "NASA Technical Paper 3621". In: (1997). URL: http://ntrs.nasa.gov/archive/nasa/casi.ntrs.nasa.gov/19970011098.pdf.

[31] J. Cugnon, D. L'Hôte, and J. Vandermeulen. "Simple parametrization of cross-sections for nuclear transport studies up to the GeV range". In: *Nuclear Instruments and Methods in Physics Research Section B: Beam Interactions with Materials and Atoms* 111.3–4 (1996), pp. 215 –220. ISSN: 0168-583X. DOI: 10.1016/0168-583X(95)01384-9.

[32] W. Czyż and L.C. Maximon. "High energy, small angle elastic scattering of strongly interacting composite particles". In: *Annals of Physics* 52.1 (1969), pp. 59 –121. ISSN: 0003-4916. DOI: 10.1016/0003-4916(69)90321-2.

[33] Linkai Ding and Evert Stenlund. "A Monte Carlo program for nuclear collision geometry". In: *Computer Physics Communications* 59.2 (1990), pp. 313 –318. ISSN: 0010-4655. DOI: 10.1016/0010-4655(90)90180-9.

[34] K.J. Eskola, R. Vogt, and X.N. Wang. "Nuclear overlap functions". In: *Int.J.Mod.Phys.* A10 (1995), pp. 3087–3090. DOI: 10.1142/S0217751X95001467.

[35] S. Fernbach, R. Serber, and T. B. Taylor. "The Scattering of High Energy Neutrons by Nuclei". In: *Phys. Rev.* 75 (9 May 1949), pp. 1352–1355. DOI: 10.1103/PhysRev.75.1352.

[36] H Feshbach and J Hüfner. "On scattering by nuclei at high energies". In: *Annals of Physics* 56.1 (1970), pp. 268 –294. ISSN: 0003-4916. DOI: 10.1016/0003-4916(70)90013-8.

[37] Peter Filip et al. "Initial eccentricity in deformed ^{197}Au $+^{197}$ Au and ^{238}U $+^{238}$ U collisions at $\sqrt{s_{NN}} = 200$ GeV at the BNL Relativistic Heavy Ion Collider". In: *Phys. Rev. C* 80 (5 Nov. 2009), p. 054903. DOI: 10.1103/PhysRevC.80.054903.

[38] J. Formánek. "High energy scattering of composite particles". In: *Nuclear Physics B* 12.2 (1969), pp. 441 –459. ISSN: 0550-3213. DOI: 10.1016/0550-3213(69)90183-7.

[39] V. Franco. "Optical limits of the Glauber approximation for nucleus-nucleus collisions". In: *Physics Letters B* 64.1 (1976), pp. 13 –16. ISSN: 0370-2693. DOI: 10.1016/0370-2693(76)90344-0.

[40] V. Franco and R. J. Glauber. "High-Energy Deuteron Cross Sections". In: *Phys. Rev.* 142 (4 Feb. 1966), pp. 1195–1214. DOI: 10.1103/PhysRev.142.1195.

[41] Victor Franco. "High-Energy Neutron-Nuclei Total Cross Sections". In: *Phys. Rev. C* 6 (3 Sept. 1972), pp. 748–757. DOI: 10.1103/PhysRevC.6.748.

[42] Victor Franco. "High-Energy Nucleus-Nucleus Collisions. I. General Theory and Applications to Deuteron-Deuteron Scattering". In: *Phys. Rev.* 175 (4 Nov. 1968), pp. 1376–1393. DOI: 10.1103/PhysRev.175.1376.

[43] G. Fricke and K. Heilig. "79-Au Gold". In: *Nuclear Charge Radii*. Ed. by H. Schopper. Vol. 20. Landolt-Börnstein - Group I Elementary Particles, Nuclei and Atoms. Springer Berlin Heidelberg, 2004, pp. 1–4. ISBN: 978-3-540-42829-9. DOI: 10.1007/10856314_81.

[44] Erwin M. Friedlander and Harry H. Heckman. "Relativistic Heavy-Ion Collisions: Experiment". English. In: *Treatise on Heavy-Ion Science*. Ed. by D.Allan Bromley. Springer US, 1985, pp. 401–562. ISBN: 978-1-4615-8099-7. DOI: 10.1007/978-1-4615-8097-3_4.

[45] R. J. Glauber. "Cross Sections in Deuterium at High Energies". In: *Phys. Rev.* 100 (1 Oct. 1955), pp. 242–248. DOI: 10.1103/PhysRev.100.242.

[46] Roy J. Glauber. "Quantum Optics and Heavy Ion Physics". In: *Nucl.Phys.* A774 (2006), pp. 3–13. DOI: 10.1016/j.nuclphysa.2006.06.009. arXiv:nucl-th/0604021 [nucl-th].

[47] J. Gosset et al. "Central collisions of relativistic heavy ions". In: *Phys. Rev. C* 16 (2 Aug. 1977), pp. 629–657. DOI: 10.1103/PhysRevC.16.629.

[48] V.M. Grichine. "A simple model for integral hadron–nucleus and nucleus–nucleus cross-sections". In: *Nuclear Instruments and Methods in Physics Research Section B: Beam Interactions with Materials and Atoms* 267.14 (2009), pp. 2460 –2462. ISSN: 0168-583X. DOI: 10.1016/j.nimb.2009.05.020.

[49] Beat Hahn, D. G. Ravenhall, and Robert Hofstadter. "High-Energy Electron Scattering and the Charge Distributions of Selected Nuclei". In: *Phys. Rev.* 101 (3 Feb. 1956), pp. 1131–1142. DOI: 10.1103/PhysRev.101.1131.

[50] David R. Harrington and Antonio Pagnamenta. "Comparison of Finitely and Infinitely Composite Models for High-Energy Proton-Proton Scattering". In: *Phys. Rev.* 184 (5 Aug. 1969), pp. 1908–1914. DOI: 10.1103/PhysRev.184.1908.

[51] J. W. Harris et al. "Pion production in high-energy nucleus-nucleus collisions". In: *Phys. Rev. Lett.* 58 (5 Feb. 1987), pp. 463–466. DOI: 10.1103/PhysRevLett.58.463.

[52] H. H. Heckman et al. "Fragmentation of He4, C12, N14, and O16 nuclei in nuclear emulsion at 2.1 GeV/nucleon". In: *Phys. Rev. C* 17 (5 May 1978), pp. 1735–1747. DOI: 10.1103/PhysRevC.17.1735.

[53] Tetsufumi Hirano and Yasushi Nara. "Eccentricity fluctuation effects on elliptic flow in relativistic heavy ion collisions". In: *Phys. Rev. C* 79 (6 June 2009), p. 064904. DOI: 10.1103/PhysRevC.79.064904.

[54] F. Hofmann and H. Lenske. "Hartree-Fock calculations in the density matrix expansion approach". In: *Phys. Rev. C* 57 (5 May 1998), pp. 2281–2293. DOI: 10.1103/PhysRevC.57.2281.

[55] R Hofstadter. "Nuclear and Nucleon Scattering of High-Energy Electrons". In: *Annual Review of Nuclear Science* 7.1 (1957), pp. 231–316. DOI: 10.1146/annurev.ns.07.120157.001311.

[56] J. Hüfner and J. Knoll. "Rows on rows — A theory for collisions between heavy ions at high energy". In: *Nuclear Physics A* 290.2 (1977), pp. 460 –492. ISSN: 0375-9474. DOI: 10.1016/0375-9474(77)90448-1.

[57] J. Hüfner, K. Schäfer, and B. Schürmann. "Abrasion-ablation in reactions between relativistic heavy ions". In: *Phys. Rev. C* 12 (6 Dec. 1975), pp. 1888–1898. DOI: 10.1103/PhysRevC.12.1888.

[58] J. Jaros et al. "Nucleus-nucleus total cross sections for light nuclei at 1.55 and 2.89 GeV/c per nucleon". In: *Phys. Rev. C* 18 (5 Nov. 1978), pp. 2273–2292. DOI: 10.1103/PhysRevC.18.2273.

[59] Paul J. Karol. "Nucleus-nucleus reaction cross sections at high energies: Soft-spheres model". In: *Phys. Rev. C* 11 (4 Apr. 1975), pp. 1203–1209. DOI: 10.1103/PhysRevC.11.1203.

[60] A.K Kerman, H McManus, and R.M Thaler. "The scattering of fast nucleons from nuclei". In: *Annals of Physics* 8.4 (1959), pp. 551 –635. ISSN: 0003-4916. DOI: 10.1016/0003-4916(59)90076-4.

[61] O. Kofoed-Hansen. "On the Glauber series interpretation of scattering data". In: *Il Nuovo Cimento A Series 10* 60.4 (1969), pp. 621–632. ISSN: 0369-3546. DOI: 10.1007/BF02757293. URL: http://dx.doi.org/10.1007/BF02757293.

[62] S. Kox et al. "Trends of total reaction cross sections for heavy ion collisions in the intermediate energy range". In: *Phys. Rev. C* 35 (5 May 1987), pp. 1678–1691. DOI: 10.1103/PhysRevC.35.1678.

[63] C. Loizides, J. Nagle, and P. Steinberg. "Improved version of the PHOBOS Glauber Monte Carlo". In: (2014). arXiv:1408.2549 [nucl-ex].

[64] Michael L. Miller et al. "Glauber modeling in high energy nuclear collisions". In: *Ann.Rev.Nucl.Part.Sci.* 57 (2007), pp. 205–243. DOI: 10.1146/annurev.nucl.57.090506.123020. arXiv:nucl-ex/0701025 [nucl-ex].

[65] G. Moliere. "Theorie der Streuung schneller geladener Teilchen I; Einzelstreuungam abbgeschirmten Coulomb-Feld". In: *Z. f. Naturforschung* A2 (1947), p. 133. URL: http://zfn.mpdl.mpg.de/data/Reihe_A/2/ZNA-1947-2a-0133.pdf.

[66] P. Moller et al. "Nuclear Ground-State Masses and Deformations". In: *Atomic Data and Nuclear Data Tables* 59.2 (1995), pp. 185 –381. ISSN: 0092-640X. DOI: 10.1006/adnd.1995.1002.

[67] J. W. Negele and D. Vautherin. "Density-Matrix Expansion for an Effective Nuclear Hamiltonian". In: *Phys. Rev. C* 5 (5 May 1972), pp. 1472–1493. DOI: 10.1103/PhysRevC.5.1472.

[68] K.A. Olive et al. "Review of Particle Physics". In: *Chin.Phys.* C38 (2014), p. 090001. DOI: 10.1088/1674-1137/38/9/090001.

[69] "Online calculator - DIAGEN - Generator of Inelastic Nucleus-Nucleus Interactions Diagrams". In: (). URL: http://hepweb.jinr.ru/glauber/glauber.html.

[70] "Online calculator - Nuclear Overlap Calculation". In: (). URL: http://web-docs.gsi.de/~misko/overlap/.

[71] Hong Pi. "An event generator for interactions between hadrons and nuclei — FRITIOF version 7.0". In: *Computer Physics Communications* 71.1–2 (1992), pp. 173 –192. ISSN: 0010-4655. DOI: 10.1016/0010-4655(92)90082-A.

[72] L. Ray. "Proton-nucleus total cross sections in the intermediate energy range". In: *Phys. Rev. C* 20 (5 Nov. 1979), pp. 1857–1872. DOI: 10.1103/PhysRevC.20.1857.

[73] R L Ray and M S Daugherity. "Applicability of Monte Carlo Glauber models to relativistic heavy-ion collision data". In: *Journal of Physics G: Nuclear and Particle Physics* 35.12 (2008), p. 125106. URL: http://stacks.iop.org/0954-3899/35/i=12/a=125106.

[74] W. Reisdorf et al. "Central collisions of Au on Au at 150, 250 and 400 A·MeV". In: *Nuclear Physics A* 612.3–4 (1997), pp. 493 –556. ISSN: 0375-9474. DOI: 10.1016/S0375-9474(96)00388-0.

[75] W. Reisdorf et al. "Systematics of central heavy ion collisions in the regime". In: *Nuclear Physics A* 848.3–4 (2010), pp. 366 –427. ISSN: 0375-9474. DOI: 10.1016/j.nuclphysa.2010.09.008.

[76] "REPRINTS Two Body Scattering Processes". In: *Geometrical Pictures in Hadronic Collisions*. Chap. 10, pp. 79–304. DOI: 10.1142/9789814415293_others01.

[77] "R. J. Glauber, in Lectures in Theoretical Physics, edited by W. E. Brittain and L. G. Dunham (Interscience, New York, 1959), Vol. I, p. 315; in High-Energy Physics and Nuclear Structure, edited by S. Devons (Plenum, New York, 1970), p. 207." In:

[78] Maciej Rybczy ński and Wojciech Broniowski. "Wounded-nucleon model with realistic nucleon-nucleon collision profile and observables in relativistic heavy-ion collisions". In: *Phys. Rev. C* 84 (6 Dec. 2011), p. 064913. DOI: 10.1103/PhysRevC.84.064913.

[79] Maciej Rybczyński and Wojciech Broniowski. "Two-body nucleon-nucleon correlations in Glauber-like models". In: *Physics of Particles and Nuclei Letters* 8.9 (2011), pp. 992–994. ISSN: 1547-4771. DOI: 10.1134/S1547477111090299.

[80] Maciej Rybczyński and Zbigniew Włodarczyk. "The nucleon–nucleon collision profile and cross section fluctuations". In: *Journal of Physics G: Nuclear and Particle Physics* 41.1 (2014), p. 015106. URL: http://stacks.iop.org/0954-3899/41/i=1/a=015106.

[81] Maciej Rybczynski et al. "GLISSANDO 2: GLauber Initial-State Simulation AND mOre..., ver. 2". In: *Comput.Phys.Commun.* 185 (2014), pp. 1759–1772. DOI: 10.1016/j.cpc.2014.02.016. arXiv:1310.5475 [nucl-th]. URL: http://www.ujk.edu.pl/homepages/mryb/GLISSANDO/index.html.

[82] L. I. Schiff. "Approximation Method for High-Energy Potential Scattering". In: *Phys. Rev.* 103 (2 July 1956), pp. 443–453. DOI: 10.1103/PhysRev.103.443.

[83] Wen-qing Shen et al. "Total reaction cross section for heavy-ion collisions and its relation to the neutron excess degree of freedom". In: *Nuclear Physics A* 491.1 (1989), pp. 130 –146. ISSN: 0375-9474. DOI: 10.1016/0375-9474(89)90209-1.

[84] S.Yu. Shmakov, V.V. Uzhinskii, and A.M. Zadorozhny. "DIAGEN — Generator of inelastic nucleus-nucleus interaction diagrams". In: *Computer Physics Communications* 54.1 (1989), pp. 125 –135. ISSN: 0010-4655. DOI: 10.1016/0010-4655(89)90038-6.

[85] Asher Shor and Ronald Longacre. "Effects of secondary interactions in proton-nucleus and nucleus-nucleus collisions using the HIJET event generator". In: *Physics Letters B* 218.1 (1989), pp. 100 –104. ISSN: 0370-2693. DOI: 10.1016/0370-2693(89)90483-8.

[86] Q.Y. Shou et al. "Parameterization of Deformed Nuclei for Glauber Modeling in Relativistic Heavy Ion Collisions". In: (2014). arXiv: 1409.8375 [nucl-th].

[87] L. Sihver et al. "Total reaction and partial cross section calculations in proton-nucleus ($Z_t \leq 26$) and nucleus-nucleus reactions (Z_p and $Z_t \leq 26$)". In: *Phys. Rev. C* 47 (3 Mar. 1993), pp. 1225–1236. DOI: 10.1103/PhysRevC.47.1225.

[88] Heinz Sorge, Horst Stöcker, and Walter Greiner. "Relativistic quantum molecular dynamics approach to nuclear collisions at ultrarelativistic energies". In: *Nuclear Physics A* 498 (1989), pp. 567 –576. ISSN: 0375-9474. DOI: 10.1016/0375-9474(89)90641-6.

[89] C. Sturm et al. "Evidence for a Soft Nuclear Equation-of-State from Kaon Production in Heavy-Ion Collisions". In: *Phys. Rev. Lett.* 86 (1 Jan. 2001), pp. 39–42. DOI: 10.1103/PhysRevLett.86.39.

[90] M.J. Tannenbaum. "Negative Binomial Fits to Multiplicity Distributions from Central Collisions of 16O+Cu at 14.6A GeV/c and Intermittency". English. In: *Hot Hadronic Matter*. Vol. 346. Springer US, 1995, pp. 263–276. DOI: 10.1007/978-1-4615-1945-4_30.

[91] Derek Teaney and Li Yan. "Triangularity and dipole asymmetry in relativistic heavy ion collisions". In: *Phys. Rev. C* 83 (6 June 2011), p. 064904. DOI: 10.1103/PhysRevC.83.064904.

[92] L. W. Townsend and J. W. Wilson. "Comment on "Trends of total reaction cross sections for heavy ion collisions in the intermediate energy range"". In: *Phys. Rev. C* 37 (2 Feb. 1988), pp. 892–893. DOI: 10.1103/PhysRevC.37.892.

[93] A. Trzci ńska et al. "Neutron Density Distributions Deduced from Antiprotonic Atoms". In: *Phys. Rev. Lett.* 87 (8 Aug. 2001), p. 082501. DOI: 10.1103/PhysRevLett.87.082501.

[94] V. Vovchenko, D. Anchishkin, and L. P. Csernai. "Time dependence of partition into spectators and participants in relativistic heavy-ion collisions". In: *Phys. Rev. C* 90 (4 Oct. 2014), p. 044907. DOI: 10.1103/PhysRevC.90.044907.

[95] A. Wagner. "Systematische Untersuchung symmetrischer Schwerionenreaktionen: Pionen als Sonden der Reaktionsdynamik". Dissertation. Technische Hochschule Darmstadt, 1996.

[96] J. Wang et al. "Effect of initial fluctuations on the collective flow in intermediate-energy heavy ion collisions". In: *Phys. Rev. C* 90 (5 Nov. 2014), p. 054601. DOI: 10.1103/PhysRevC.90.054601.

[97] Xin-Nian Wang and Miklos Gyulassy. "hijing: A Monte Carlo model for multiple jet production in pp, pA, and AA collisions". In: *Phys. Rev. D* 44 (11 Dec. 1991), pp. 3501–3516. DOI: 10.1103/PhysRevD.44.3501.

[98] K. Werner. "Analysis of proton-nucleus and nucleus-nucleus scattering at 200 A GeV by the multistring model Venus". In: *Physics Letters B* 208.3–4 (1988), pp. 520 –524. ISSN: 0370-2693. DOI: 10.1016/0370-2693(88)90660-0.

[99] G. D. Westfall et al. "Nuclear Fireball Model for Proton Inclusive Spectra from Relativistic Heavy-Ion Collisions". In: *Phys. Rev. Lett.* 37 (18 Nov. 1976), pp. 1202–1205. DOI: 10.1103/PhysRevLett.37.1202.

Methods of Event Characterization

The Gold-Gold production beamtime was scheduled from April 5^{th} to May 7^{th} 2012. Within the 5 weeks of beamtime the SIS18 delivered 684 hours of Au^{69+} ions beam to the HADES cave [3] with an intensity of $1.2 - 2.2 \times 10^6$ ions per sec. The overall total data volume recorded on disc is 140 Tbyte, including calibration and cosmic runs. The data-taking, summarized in table 20, amounts to a total of 558.3 hours, with a total event count of 7.31×10^9. This includes 3% calibration and CTS (Central Trigger System) events and the fraction of recorded central PT3-events is 80%, corresponding to 5.85×10^9 events. Due to the reduction of the peripheral PT2-event class by a factor of 8, the fraction of recorded PT2-events is 17%. The analysis sample used for this thesis, summarized in table 21, is taken from day108 with 8 hours of data-taking. This sample was chosen as the reference for a day-by-day calibration, due to the fact that in this run the MDCs in all six sectors were working most efficiently. If not explicitly mentioned, the 7^{th} data-production generation (gen7) was used.

First day	5.4.2012 – 22h
Last day	7.5.2012 – 07h
Data taking	558.3 hours
Number of days	33
Number of runs	12046
Number of files	95041
Total file size	138 T
Number of events	7312.6 M
Mean event rate	3.6 KHz

Table 20: Statistics of the total Gold-Gold production beamtime 2012.

Data taking	7.79 hours
Start & end	16h – 24h
Number of runs	174
Number of files	1382
Total file size	2003.0 G
Number of events	101.5 M
PT3 events	80%
PT2 events	17%
CTS & other	3%

Table 21: Statistics of day108 (17.4.2012).

Centrality Estimators

To determine the percentage of selected central events with respect to the total cross section, three complementary methods can be used. The first one is based on the trigger cross section, as calculated from the recorded beam and trigger rates.

The second, as discussed in the previous chapter, is based on quantities, which are correlated to the *violence* of the collision and thus characterize the centrality of an event, like the event multiplicity, and are called *centrality estimators*. The main centrality estimator used in this analysis is the distribution of the number of primary tracks $N_{primaryTracks}$. To study the behavior of the different estimators, shown in table 22, in addition the number of selected Tracks $N_{selectedTracks}$, the number of identified *protons* and *pions*, and the hit based estimator using the TOF-hits N_{TOF} and RPC-hits N_{RPC}, with and without time-cuts, are compared. Due to the geometrical properties of heavy-ion collisions, the most central events should have a high azimuthal symmetry in the

Track based
selected and primary tracks
Hit based
TOF-hits and TOF+RPC-hits with and w/o timecut
FW-hits and total charge
PID based
Number of *protons* and *pions*
E_t transverse Energy
Event shape
Directivity [4]
Ratio E_t/E_z (ERAT [7, 8])

Table 22: Centrality Estimators.

transverse momentum distribution and a maximum in the produced transverse energy E_t. To study the centrality dependent momentum distribution, event shape observables, like the transverse momentum *directivity* [4]:

$$D = \left. \frac{|\sum_i \vec{p_{t,i}}|}{\sum_i |\vec{p_{t,i}}|} \right|_{y_i \geq y_{c.m.}} \tag{42}$$

and the *ratio of total transverse to longitudinal kinetic energies* [7, 8]:

$$R_{Et/Ez} = \left. \frac{\sum_i E_{t,i}}{\sum_i E_{z,i}} \right|_{y_i \geq y_{c.m.}} \tag{43}$$

are often suggested. The third approach is the estimation of the centrality by the number of spectators in the forward region via the measurement of the total charge of fragment-hits in the FW in a time-of-flight window of $\beta = 0.9 \pm 0.1$.

Track and Particle Selection

In the analysis of event multiplicities no additionally track selection criteria were used, apart from the conditions implemented in the track reconstruction and sorting algorithms. From all reconstructed track candidates, only flagged tracks, called *selected tracks*, were considered, which have the best matching to the contributing hit-points and fulfill the condition that these hit-points are not shared by other track candidates. The next subset are the *primary tracks* which fallow the additional condition that each track should have a distance of closest approach to the primary vertex below $d_{min} < 10$ mm. In figure 92 the correlation

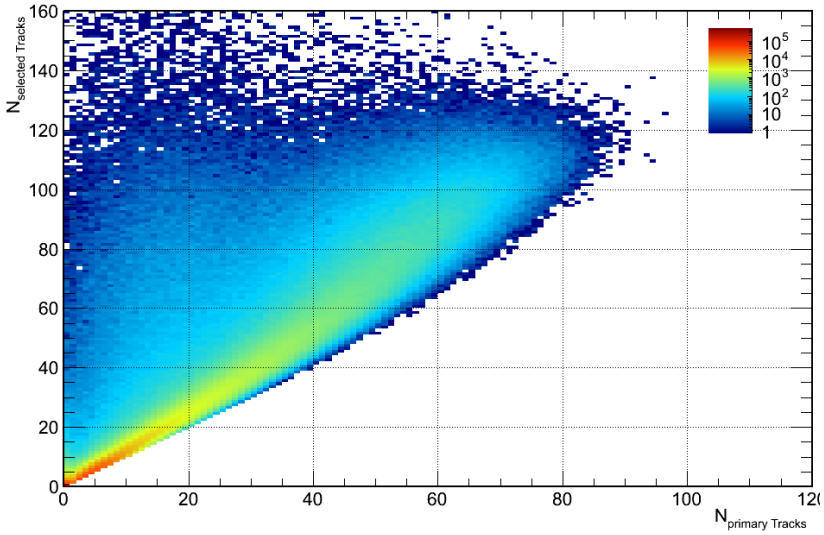

Figure 92: Correlation plot of number the selected and primary tracks per event in minimum-bias data.

between $N_{selectedTracks}$ and $N_{primaryTracks}$ per events is plotted, where events show a higher multiplicity in $N_{selectedTracks}$ either due to lose conditions in the track reconstruction or generated by pile-up events. The

advantage of the track-based estimator in comparison to the hit-based estimator are that they represent the best estimation of the number of primary charged particle N_{ch} produced in the collision. The disadvantage of these estimators are, that corrections for time dependent fluctuations have to be applied, which occur due to the efficiency of the MDC sectors. On the other hand, the hit-based estimator N_{TOF} and N_{RPC} are biased by their sensitivity to additionally secondary particles produced in the detector material and their dependence on the quality of the event timing. Particle identification of *protons* and *pions* is done

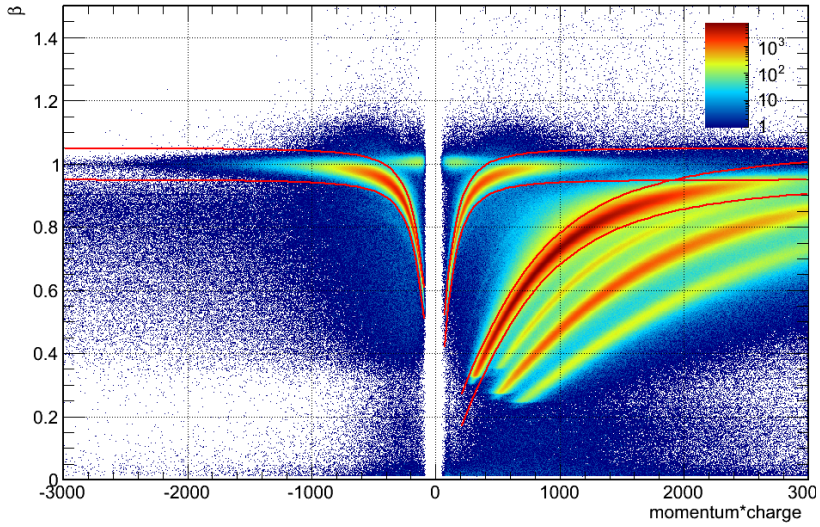

Figure 93: The correlation between beta and momentum multiplied by the charge for all reconstructed particle candidates. The red lines indicates the beta-momentum cuts for protons, π^-, and π^+.

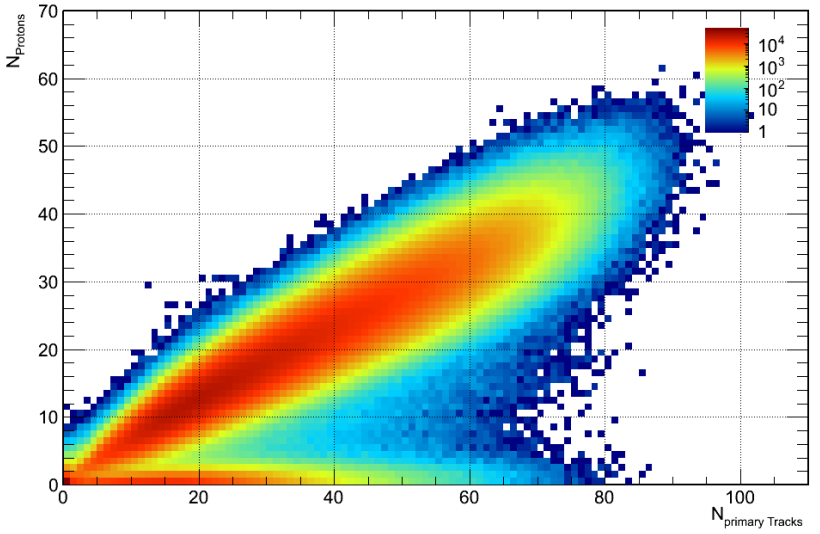

Figure 94: The correlation between the number of identified protons per event and $N_{primaryTracks}$ in PT3 data. The average number of protons scales with primary track multiplicity, beside events with low proton multiplicity $N_{part} < 7$ caused by wrong event timing.

two dimensional cuts in beta versus momentum, shown in figure 93. The number of *protons* after selection is shown in figure 94 and the sensitivity of the proton multiplicity to the event timing is also visible. A cut into events with low proton multiplicity is used to reject events

with wrong event timing. The total transverse kinetic energy E_t of i, identified protons and pions defined via the beta-momentum cut in forward rapidity, is calculated in the following way:

$$E_t = \sum_i E_i \sin\theta_i \Big|_{y_i \geqslant y_{c.m.}} , \tag{44}$$

and is shown in figure 95 as a function of $N_{primaryTracks}$. Also here a clear correlation is observable.

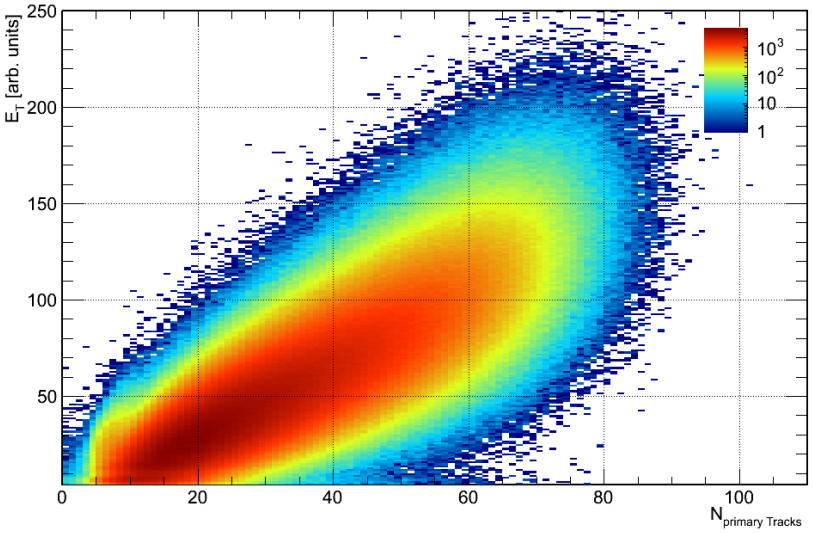

Figure 95: The uncorrected total transverse kinetic energy E_t per event in the forward rapidity in arb. units of all proton and pions, identified via the beta-momentum cut shown in figure 93, as a function of $N_{primaryTracks}$.

Cross section and trigger bias determination

The total reaction cross section includes inelastic, as well as elastic and dissociation reactions, shown in figure 96. The elastic and dissociation reactions are dominant for very peripheral events with large impact parameters, which generate low multiplicities in the HADES acceptance. Only the inelastic interactions are contributing to the particle production and can be selected by a sufficiently high multiplicity threshold. The total hadronic cross section is calculated in the previous chapter as 6.83 ± 0.43 barn. The cross section for inclusive electromagnetic and nuclear dissociations with one-, two- and three-neutron removal is measured to be around 3.89 ± 0.23 barn [2] for Au+Au at 1 AGeV.

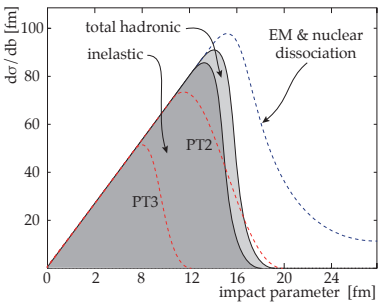

Figure 96: Schematic plot of the total cross section, the different contributions and estimates for the multiplicity trigger PT2 and PT3.

Trigger configuration

In the Au+Au beamtime two Physics Trigger (PT) were activated, which are defined as multiplicity-trigger with thresholds corresponding to around 5 (PT2) and 20 (PT3) hits in the TOF detector. These threshold-triggers were realized by the analog multiplicity signal of the TOF-array

and required a coincidence with a signal of the Start-Detector in a time window of $\sim$ 50 ns. Due to electronic noise, the trigger-edge is

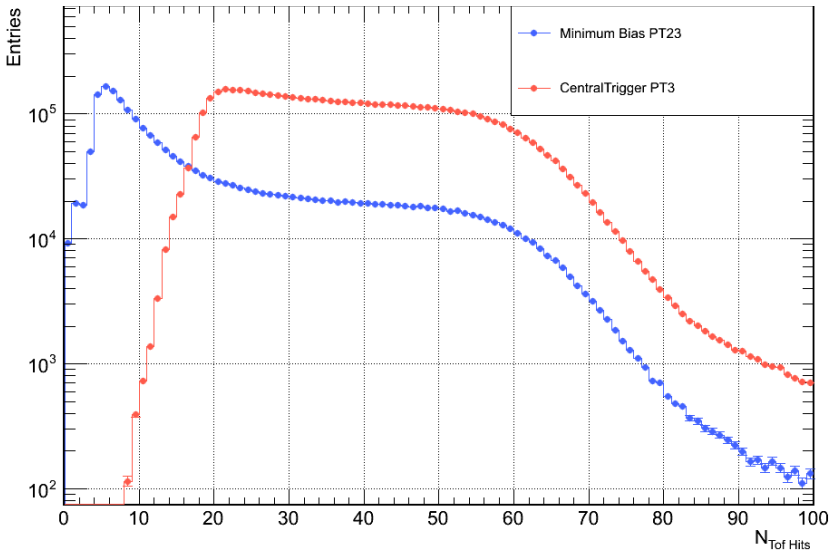

Figure 97: TOF-multiplicity-distribution as recorded during the beamtime with (■) minimum-bias reduced by a factor of 8 and (■) central trigger (PT3).

smeared out and the analog trigger-efficiency has to be calculated and included in simulations. Additionally, due to the high beam-flux of up to 2.2×10^6 particles per second and the resulting dead time, only a certain number of triggered events are accepted by the DAQ and recorded on disc. Using the information from the beam and trigger

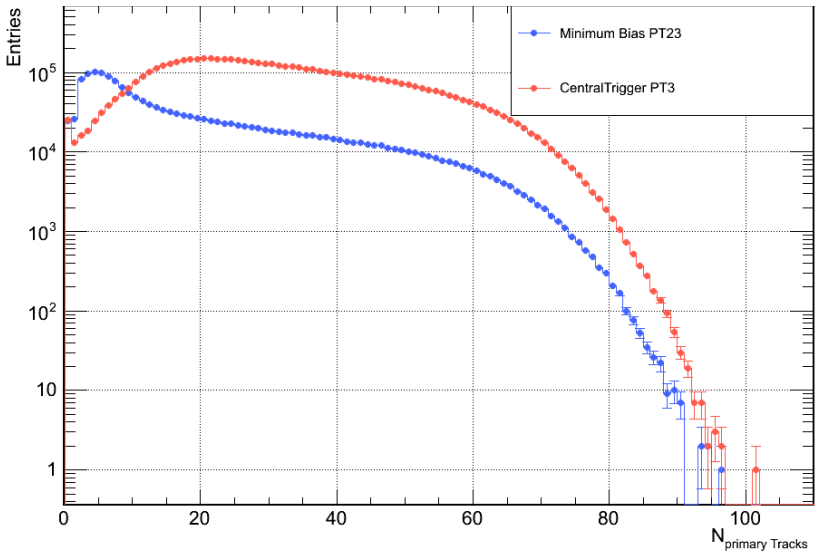

Figure 98: Multiplicity-distribution of number of selected Tracks as recorded during the beamtime with (■) minimum-bias reduced by a factor of 8 and (■) central trigger (PT3).

counters, called *scalers*, as well as the number of accepted and recorded events, this event losses can be determined and corrections can be applied in the analysis. Due to the statistical occurrence of the reactions, two or more events can appear close in time with a finite probability.

These events, called *pile-up* events, are dependent on the beam rate, the dead time and the trigger threshold [9]. The term *minimum-bias* is specific for an experimental trigger condition which includes the widest spectrum of different event centralities in an experimental setup. The minimum-bias trigger used during the Au+Au beamtime was the PT2 trigger[7], including most of the inelastic events, but also dissociation and peripheral fragmentation reactions as well as background reactions. The highest contribution from background-events originates from the material of the Start-detector (Au+C). The central trigger PT3 was adjusted to collect only central gold-gold inelastic collisions.

[7] In the recorded data, three different trigger bits were used: the downscaled PT2 and PT3-events and the unscaled PT3-events. In the following the *minimum-bias* data referrers to the distribution of recorded events with the downscaled PT2- and PT3-trigger bit and the *central* data to both PT3-trigger bit.

Beam	
energy	1.23 AGeV
particle	Au^{69+}
intensity	$1.2 - 2.2 \times 10^6$ Hz
^{197}Au-Targets	
int. prob. L_0	1.35%
thickness d	$15 \times 25\mu$m
density ρ	19.3 g/cm^3
^{12}C Start-Detector	
int. prob. L_0	0.26%
thickness d	$\sim 50\mu$m
density ρ	1.84 g/cm^3

Table 23: Beam and target specifications.

	PT2	PT3
N_{trig}/N_{beam}[%]	1.656	0.577
σ_{trig}[mb]	7684 ± 6	2608 ± 3

Table 24: Trigger cross section for day 108 with only statistical errors.

Trigger cross section

For a certain experimental trigger condition the trigger cross section can be calculated according to [6]:

$$\sigma_{trig} = \frac{N_{trig}}{N_{beam}} \cdot \left(\rho \cdot d \cdot \frac{N_A}{M}\right)^{-1} \tag{45}$$

Here, N_A is the Avogadro constant, d the thickness of the target, ρ the density and M the molar mass of the target material. The interaction probability N_{trig}/N_{beam} is calculated with the number of interactions accepted by the trigger N_{trig} and the number of beam particles N_{beam}, which are stored in CTS-events every second. The efficiency of the Start-Detector, its time-dependent efficiency loss during the beamtime and the contribution of background reactions are not taken into account in the calculation. The trigger cross section for central PT3-events amounts to 2.6 barn and corresponds to $\sigma_{PT3}/\sigma_{tot} = 38 \pm 3\%$.

Trigger Efficiency & Bias Determination

Taking only the effect of the analog trigger edge into account, the PT3 trigger efficiency as a function of the number of hits in the TOF-detector can be obtained as the ratio of the *minimum-bias* distribution (PT2 including PT3 events) and the PT3 distribution, normalized to the same integral of events in the high multiplicity part.

The parameterization of the ratio is based on a modified error-function, with the turn-on point p_0 and the slope p_1 calculated as:

$$f(x) = p_2 + (p_3 - p_2)/2 \cdot \left(1 + \mathrm{Erf}((x - p_0) \cdot \sqrt{2}/p_1)\right) \tag{46}$$

The derivative is a Gaussian with the mean p_0 and the sigma p_1, used as trigger-emulator in the HGeant detector simulation and the Glauber MC simulation. It emulates the smeared threshold of the TOF response, with the following condition:

```
TofMult >= Mean + gRandom->Gaus(0,Sigma)
```

In figure 99 the ratio and the parameterization is shown, while figure 100 displays the calculated impact-parameter distribution with a sharp cut into $N_{TOF} > 19$ and with employing the PT3 trigger emulator.

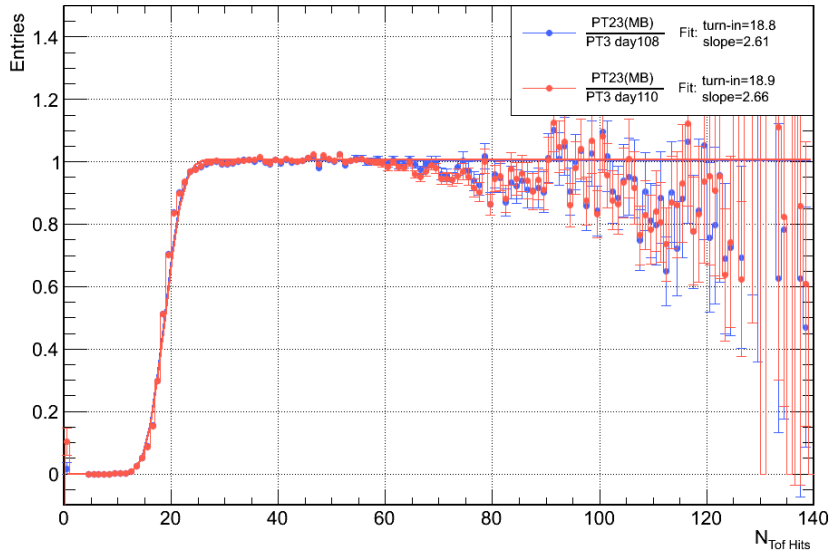

Figure 99: Trigger efficiency of PT3 triggered events for day 108 and 110 as a function of the TOF-hit multiplicity. The parameterization of the ratio is based on a modified error-function. The PT3-trigger threshold sets in at around ≈ 25, with the turn-on point $p_0 = 19$ and the slope $p_1 = 2.6$.

An estimate for the PT3 cross section would be around $\sigma/\sigma_{tot} = 30\%$ for the sharp-cut and $\sigma/\sigma_{tot} = 32\%$ for the trigger emulator. The underestimation of the PT3 cross section by around 10% in comparison

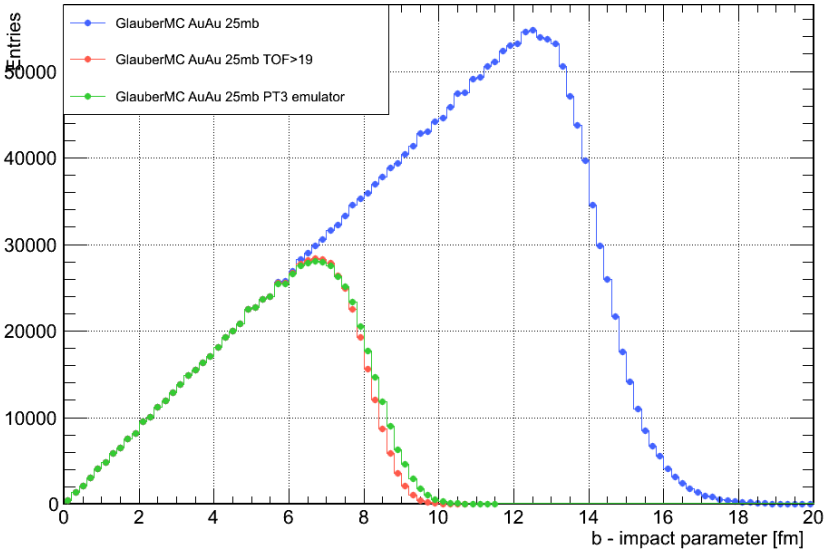

Figure 100: Impact parameter distribution from the Glauber MC simulation of the TOF-detector response (■) minimum-bias Glauber MC, the (■) sharp-cut $N_{TOF} > 19$ and the (■) PT3 emulator with $p_0 = 19$, $p_1 = 2.6$.

to the other methods, is mainly caused by the large uncertainty in the Glauber-fit to the TOF-detector response. Due to the timing-cuts, used to reject TOF-hits not directly correlated with the triggered event, more peripheral events are excluded, resulting in the underestimation of the cross section.

Event selection

The aim of the event selection in the offline analysis is to select the most central inelastic hadronic interactions as efficiently as possible and to reduce the contribution of events from background and off-target reactions with timing and vertex cuts. Additionally, *outlier-events* are rejected by cuts, where measurements in different sub-detectors can differ strongly, *e.g.* the correlation between the

- FW-hits or total spectator charge vs. TOF+RPC multiplicities
- number of primary or selected tracks vs. TOF+RPC multiplicities
- multiplicities between inner and outer reconstructed tracklets.

Special care should be taken that the event selection is not introducing a bias, which is multiplicity dependent. If this cannot be avoided a correction for the event loss has to be determined.

Event Timing

To ensure a precise time-of-flight measurement for particle identification (PID) a good event start time T_0 is essential. In the case where a good start time could not be found or reconstructed the event is flagged and can be rejected in the further analysis. Three timing methods are

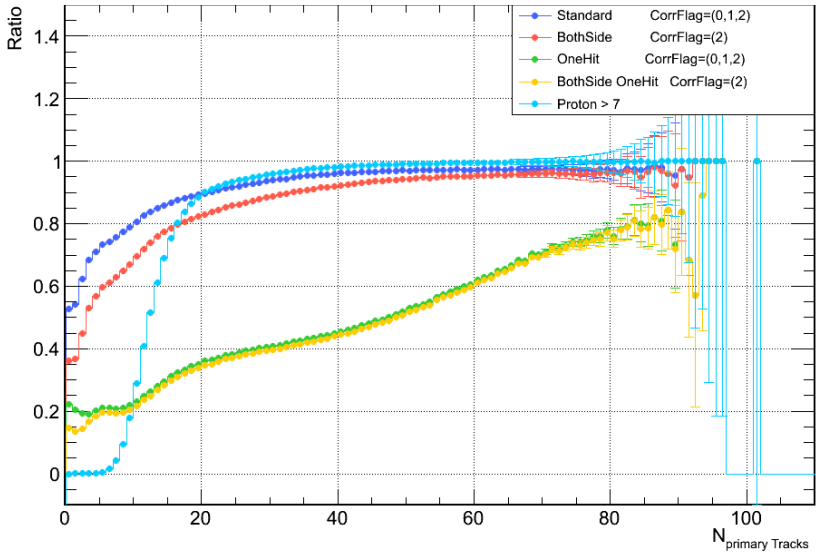

Figure 101: Selection efficiency of timing methods in PT3 triggered events as a function of the primary track multiplicity (■) correlation found (flags: 0,1,2) (■) only one Start-hit in the event window (flags: 0,1,2) (■) one hit, only correlation in Start (flag: 2) (■) only correlation in Start (flag: 2) (■) proton event multiplicity $N_{proton} > 7$.

established in the standard HADES analysis. The first one uses the timing signal of the Start-detector, the second uses the correlated hit information from the META time-of-flight detectors, and the last one is based on PID information, such as the number of reconstructed protons or pions in the event as a timing criteria. As previously discussed, a

wrong event timing results in an systematic shift of the β of protons and pions in the event. In the case of a high multiplicity event, those with low identified proton multiplicity $N_{proton} < 7$ or with no pions can be rejected. Based on the measured momenta of identified protons and pions in certain β vs momentum regions a method is implemented to improve the resolution of the event start time T_0. This method is limited to events with small deviation to the real event time only. For larger shifts a full T_0-reconstruction via an iterative χ^2-minimization method is needed, where the event time is reconstructed by a comparison of the measured TOF to an expected TOF as deduced by the measured momentum and an mass hypothesis for each used track [1].

The timing signal of the Start-detector is used as event time T_0, if a hit in the front side (X-stripes) correlates with a hit on the back side (Y-stripes) of the detector in a time window of 0.5 ns. If no correlated hits are found between the front or back side, an estimate of the event start time is calculated by the mean time-of-flight of the three fastest hits in the TOF and RPC detectors and the closest start hit time from one side of the start detector. With the assumption that the fastest hits are from particles around $\beta \approx 1$ and the normalized flight-length is 2.1 m, a search for a start hit corresponding to a flight-of-time close to 7 ns is performed. If no correlation between Start- and META-Detectors is found in the time window of 10 ns, the event is flagged.

2	both side correlate in 0.5 ns
1	back side correlates with META
0	front side correlates with META
-1	no correlation found

Table 25: T_0 Timing Correlation-Flag.

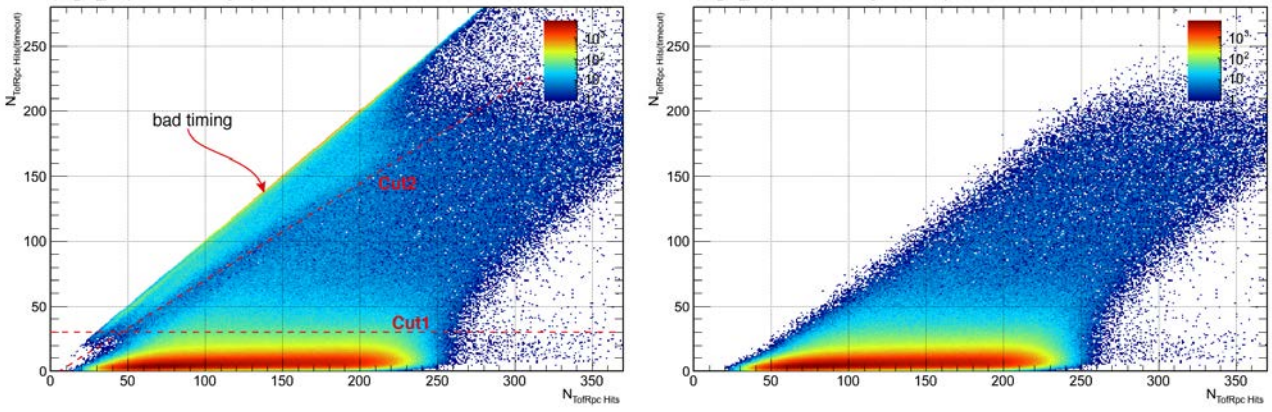

Figure 102: Multiplicity-distribution of the META detectors in the total event time window (1µs) vs. multiplicity outside the time window (25 or 21 ns). (left) PT3 events with no further selection and two proposed timing cuts. (right) Same plot with the requirement of more than 7 identified protons in the event.

The *META timing* selection method makes use of the time distribution of hits in TOF and RPC via a comparison of the multiplicity in the total event time window ($\sim$ 1 µs) and a time window after the start time, which is 35 ns long for TOF and 25 ns for RPC. This concept is based on the idea that, in the case that the start time is deviating from the real event time, a certain number of META hits will be moving out of the time window. Additionally, the ratio of the multiplicity inside to the one outside of the time window could indicate an overlap of a pile-up events or a background reaction.

Event vertex

To reduce the contamination of off-target interactions the event vertex was restricted to the 6 cm long region around the segmented target. The contribution of reactions within the start detector located 2.8 cm in front of the first and 7.8 cm of the last target segment can be rejected by a cut on the position of the reconstructed vertex in z-direction between −60 and 0 mm, shown in figure 103 and 104 (left).

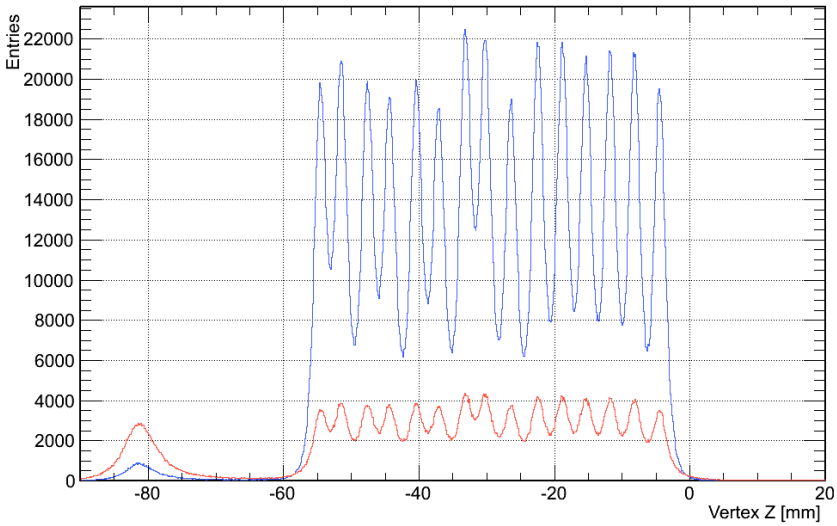

Figure 103: The distribution of the z-position of the reconstructed primary vertex in (■) minimum-bias and (■) central PT3 data.

In a dedicated *empty-target* run on day126 the beam was shifted relative to the nominal setting by about 3.5 mm and the Start-Detector by 1.25 mm, so the target segments were not illuminated by the beam spot. In figure 104 the comparison between day108 and *empty-target* run

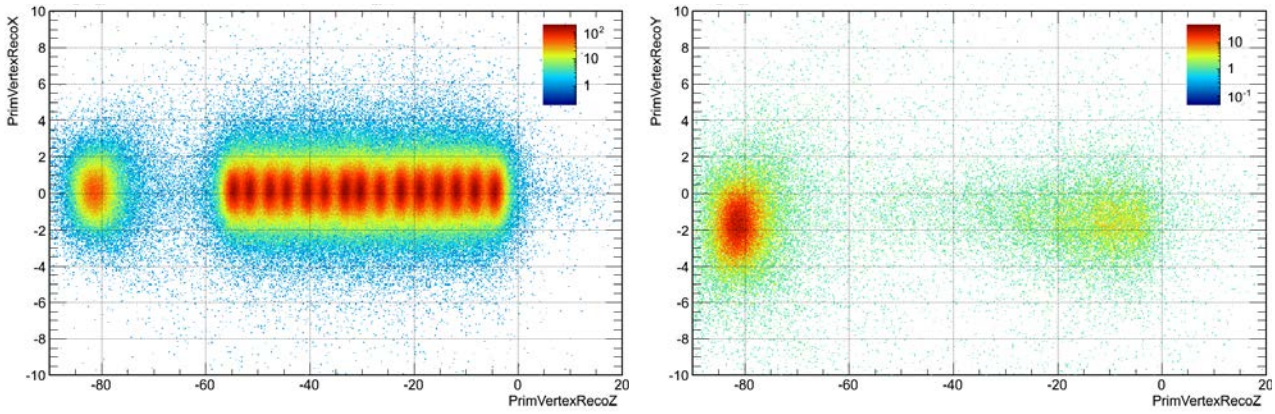

Figure 104: Comparison between the run of day108 (left) and the *empty-target* run on day126 (right) with the shifted position of the beam by 3.5 mm and of the Start-Detector by 1.25 mm.

on day126 in vertex position y-z direction is shown. In figure 105 the contribution of the Start-detector and the off-target below a multiplicity of 15 primary tracks is visible and these contribution can be excluded

by the requirement that the multiplicity should be higher than 15 for primary tracks. The comparison to Glauber MC simulations this additional contribution of background reactions is visible in the ratio between data and simulation, as shown in figure 109. The vertex

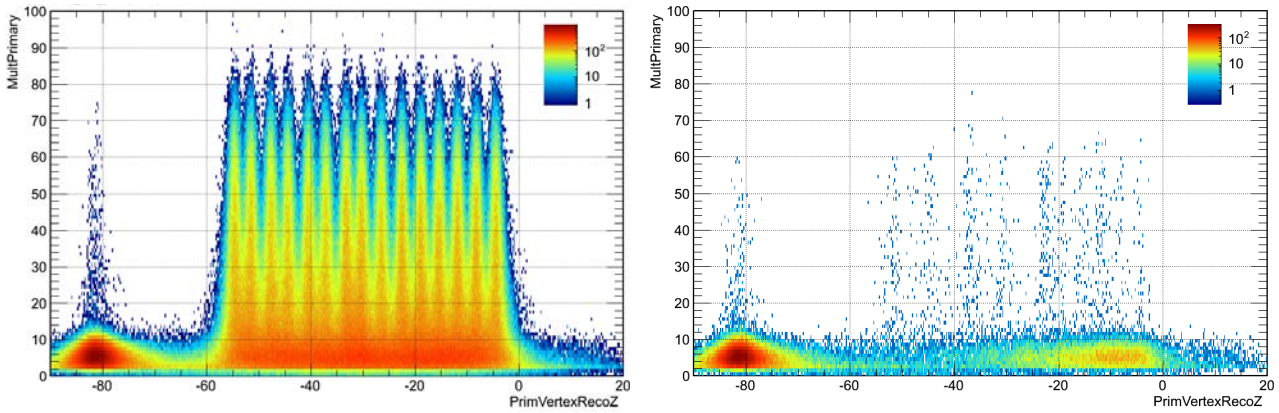

Figure 105: Comparison between the run of day108 (left) and the *empty-target* run on day126 (right). The primary track multiplicity is shown against the primary vertex z-position. The contribution of the Strart-detector and off-target is visible below a multiplicity of 15 primary tracks.

reconstruction efficiency is calculated in a full MC simulation with HGeant. The resolution of the vertex reconstruction, dependent on the number of tracks, is estimated by the deviation between initial and reconstructed z-position, to be:

$$\sigma_{\Delta Z} \approx 4.3\text{mm}/\sqrt{N_{Tracks}}\,. \tag{47}$$

The effects of multiple vertices from pile-up or background events are not taken into account in the simulation.

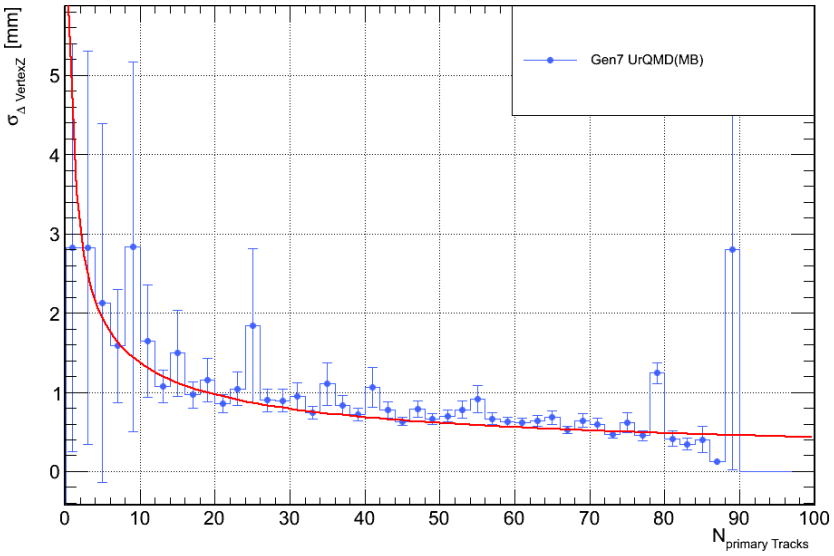

Figure 106: The vertex-reconstruction efficiency for the HGeant full detector simulation (minimum-bias) as a function of primary tracks. The deviation $\sigma_{\Delta VertexZ}$ between the initial and reconstructed vertex in z-direction, with the parametrization $\sigma_{\Delta Z} \approx 4.3\text{mm}/\sqrt{N_{Tracks}}$.

Centrality Determination via Glauber-fit

As previously discussed in Chapter 4 the particle multiplicity recorded by the detectors can be calculated by convoluting N_{part} with a simple model for the particle production, including the efficiency and fluctuations of the detector. In the following, the multiplicity distribution was sampled for each event randomly from a Gaussian distribution with a mean and sigma of:

$$N_{mean} = \mu \cdot N_{part} \ , \ \sigma = k \cdot \sqrt{\mu \cdot N_{part}} \tag{48}$$

In figure 107 the Glauber-fit to the $N_{primaryTrack}$ distribution for the minimum-bias and the central data are shown. The parameters μ and k

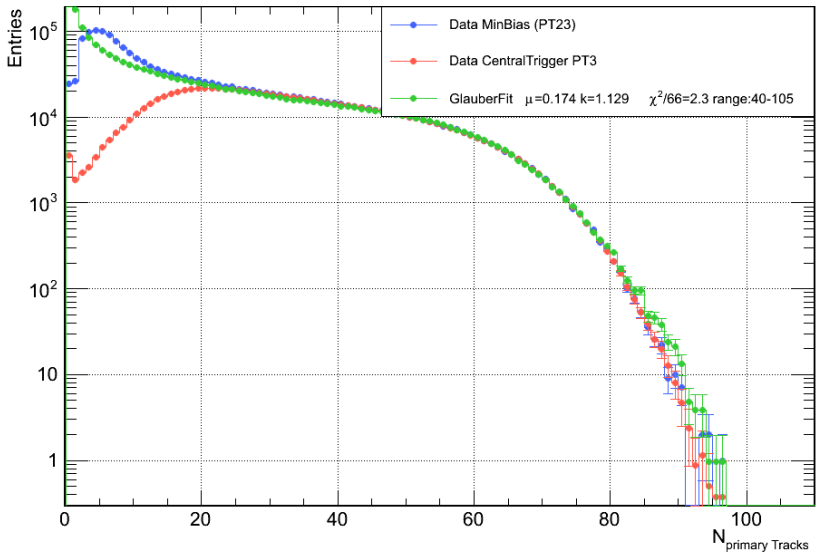

Figure 107: The uncorrected $N_{primaryTrack}$ multiplicity-distributions. Shown are (■) minimum-bias, (■) central data and the (■) Glauber-fit with $\mu = 0.174$ $k = 1.129$.

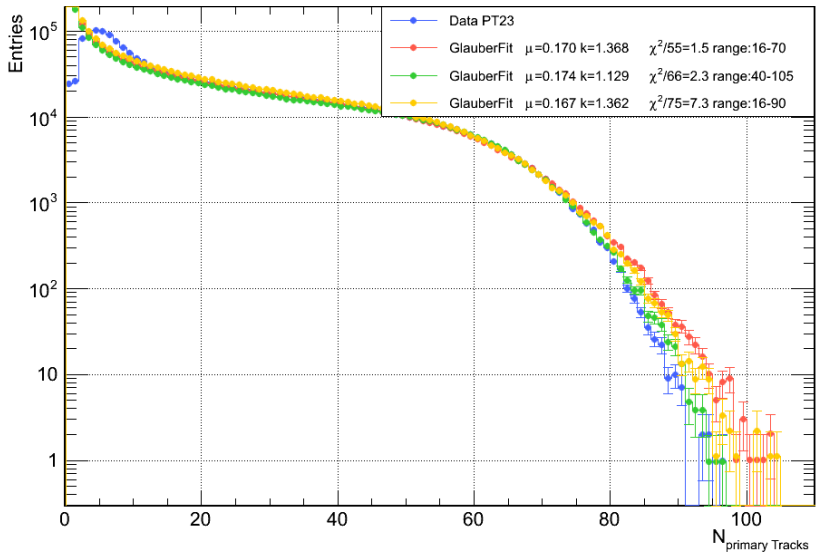

Figure 108: The uncorrected $N_{primaryTrack}$ multiplicity-distributions for minimum-bias data (■) compared to the Glauber-fits with different fit-ranges. The resulting reduced χ^2/ndf are (■) 1.5 (■) 2.3 (■) 7.3.

are determined by a χ^2-minimization procedure, which compares an ensemble of various simulated multiplicity distributions in a certain multiplicity fit-range with the measured one. The multiplicity fit-range is needed to exclude regions from the fit with a trigger bias or with strong event losses due to the selection methods. A selection of Glauber-

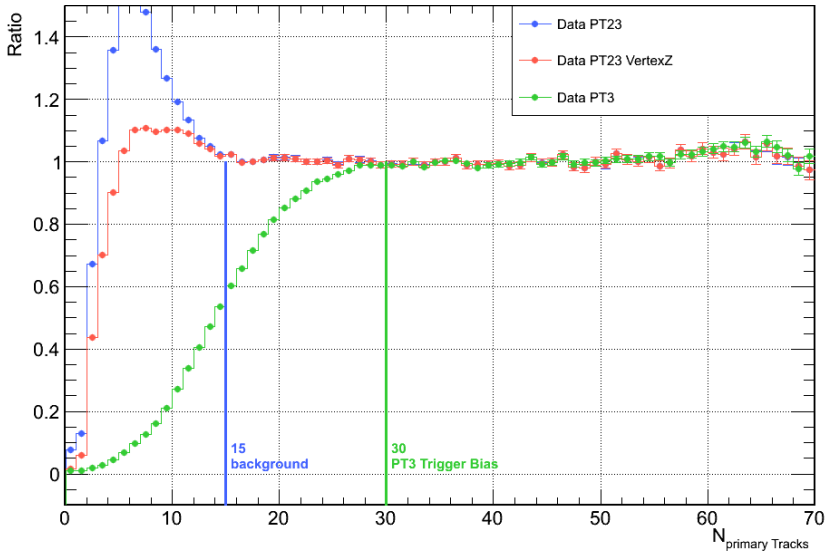

Figure 109: The ratio between the Glauber-fit to the (■) minimum-bias, the (■) minimum-bias with a z-vertex cut in the target region $z > -60$ and the (■) central PT3-trigger data. The PT3-trigger bias at around 30 and the contribution of background and off-target reactions below 15 are visible as an enhancement in the ratio.

fits with different fit-ranges, the resulting fit-parameters μ, k and the reduced χ^2/ndf-values are shown in figure 108. In figure 109 the ratio between the Glauber-fit to the minimum-bias data and to the data with an additionally z-vertex cut ($z > -60$) in the target region is shown. The contribution of background and off-target reactions

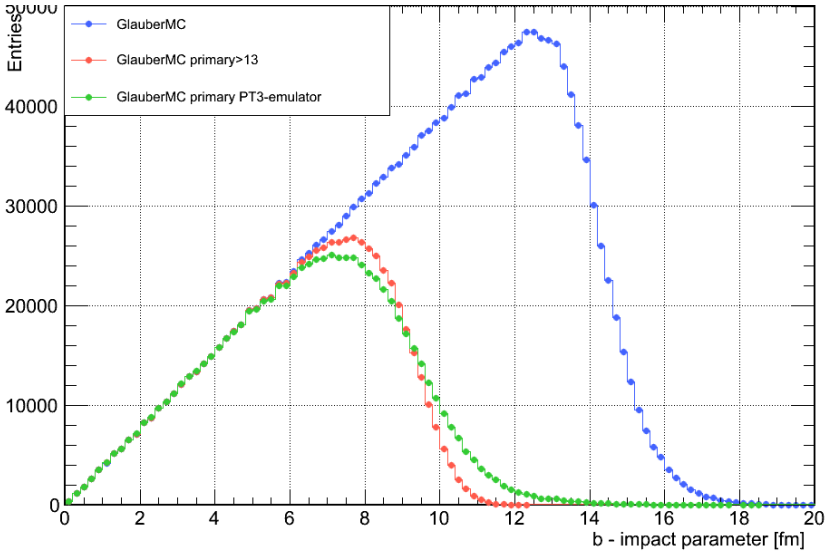

Figure 110: Impact parameter distribution from the Glauber MC used in the simulation of $N_{primaryTracks}$ with the (■) minimum-bias Glauber MC, the (■) sharp-cut $N_{primaryTracks} > 13$ and the (■) PT3 emulator with $p_0 = 13.8$, $p_1 = 5.39$. The resulting cross section $\sigma_{PT3}/\sigma_{tot}$ is 40% and 41%, respectively.

below $N_{primaryTracks} < 15$ is visible as an enhancement to the reaction

cross section calculated by the Glauber MC. The central PT3 data is also plotted with its trigger bias around 30. The parametrization with the trigger-function eq. (46) results in a turn-on point $p_0 = 13.8$ and a slope $p_1 = 5.39$. The corresponding estimation for the PT3 cross section would be around $\sigma_{PT3}/\sigma_{tot} = 41\%$. To estimate the contribution of gold-carbon reactions in figure 111 Glauber MC data for Au+C are simulated and fitted to the multiplicity-distribution obtained with a vertex-cut in the region around the Start-detector.

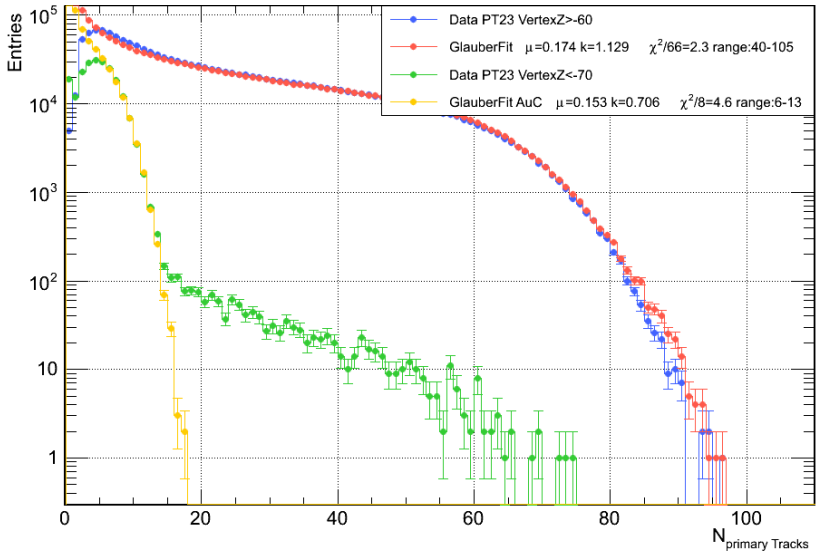

Figure 111: The uncorrected N_{ch} multiplicity-distribution determined by the number of *primary tracks*, similar to figure 107, with minimum-bias data and the corresponding Glauber MC simulation, but with an z-vertex cut around the Start-detector position to exclude the target region.
(■) Target z-vertex > -60
(■) Glauber-fit $\mu = 0.174, k = 1.129$
(■) Start-det. z-vertex < -70
(■) Glauber-fit AuC $\mu = 0.153, k = 0.706$

In figure 112 the Glauber-fit to the total transverse kinetic energy E_t distribution is shown.

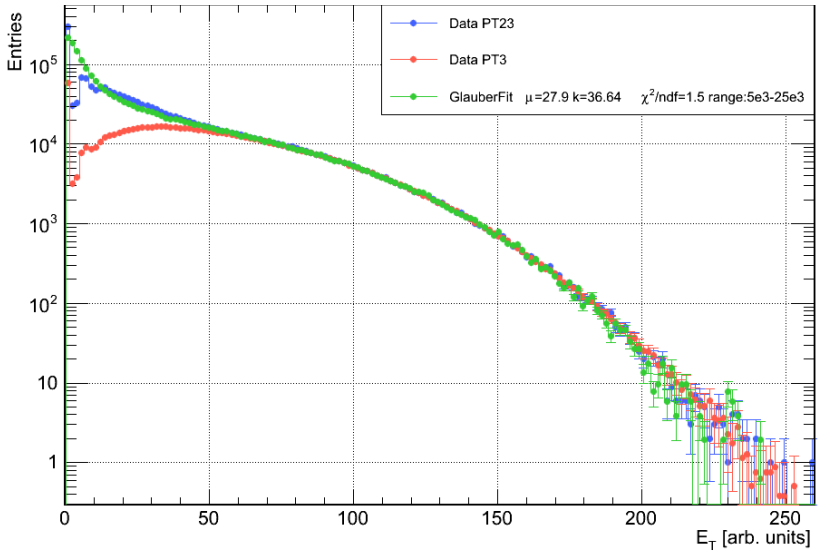

Figure 112: The uncorrected E_t distribution with (■) minimum-bias, (■) central PT3-trigger and the (■) Glauber-fit with $\mu = 29.9$ $k = 36.6$.

Comparison of Glauber-fit to full MC simulation

As a proof-of-concept the multiplicity-distribution obtained from a full MC with the UrQMD event-generator and HGeant detector simulation was fitted in the same approach like data and is plotted in figure 113.

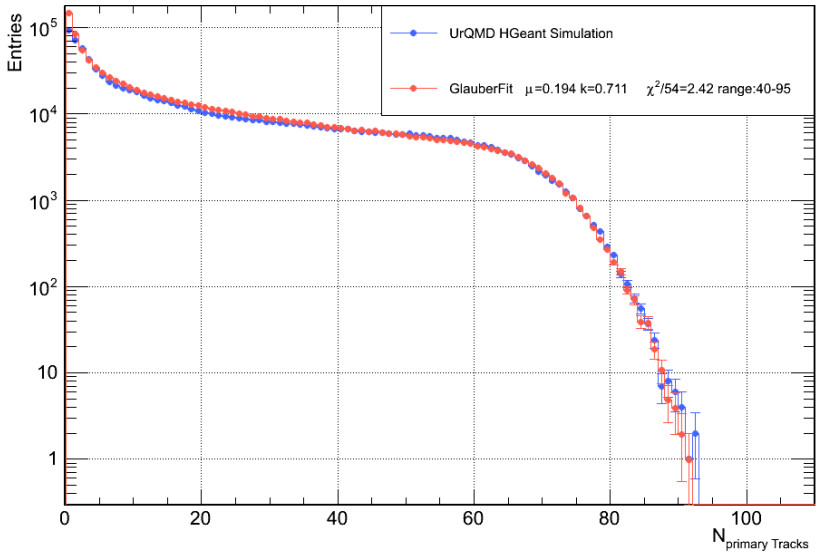

Figure 113: The uncorrected $N_{primaryTrack}$ multiplicity-distribution obtained with (■) minimum-bias data with a full MC with HGeant and UrQMD, and the (■) Glauber-fit with $\mu = 0.194, k = 0.711$.

The comparison between the initial impact-parameter distribution of the UrQMD model and the one estimated with the Glauber-fit is shown in figure 114, where the mean impact-parameter $\langle b \rangle$ is plotted as function of the multiplicity-bin. An systematic shift by ≈ 0.5 fm of the mean $\langle b \rangle$ and an uncertainty of ≈ 10 in $N_{primaryTrack}$-bins between the two distributions is visible.

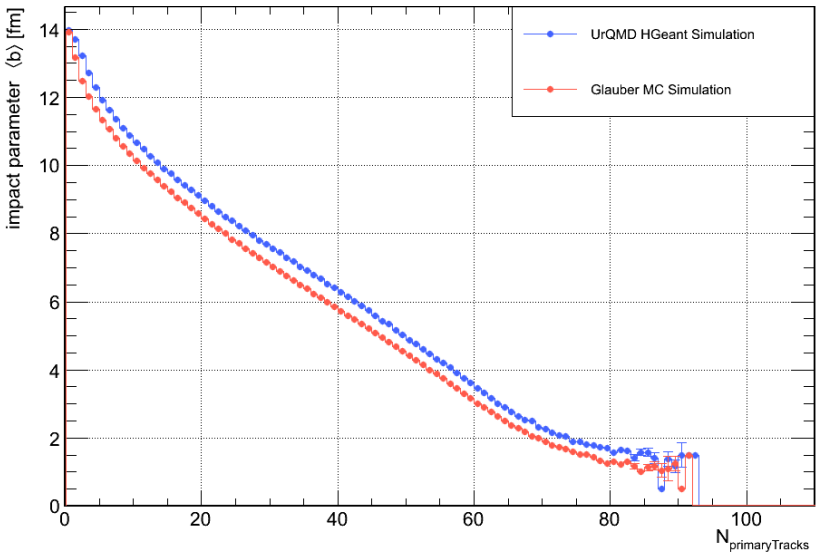

Figure 114: The mean impact-parameter $\langle b \rangle$ as a function of $N_{primaryTrack}$ with (■) input from minimum-bias MC with HGeant and UrQMD, and the (■) resulting impact-parameter obtained by the Glauber-fit shown in fig. 113.

Particle multiplicity and centrality dependence

To investigate the centrality dependence of the pion and proton multiplicities, the mean particle event multiplicity is shown for identified charged pions in figure 115 and for protons in figure 116. A nearly linearly increasing function of the primary track multiplicity is observed. The output from the full MC simulation with the event-

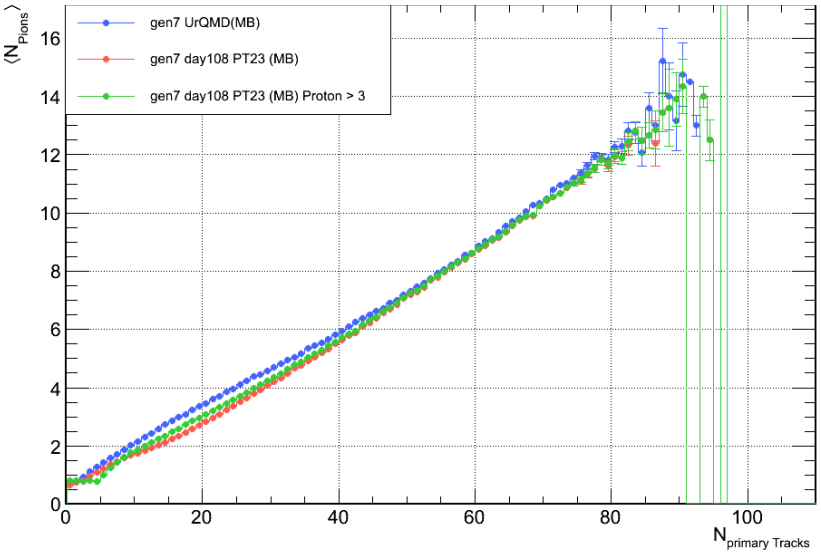

Figure 115: The mean pion event multiplicity as a function of $N_{primaryTrack}$ obtained with (■) full MC (UrQMD), (■) minimum-bias data and additionally with the (■) condition to measure more than 3 identified protons.

generator UrQMD is plotted. Also here the mean pion multiplicity is as expected scaling linearly with the primary track multiplicity, in reasonable agreement with the simulation. In contrary to protons, all

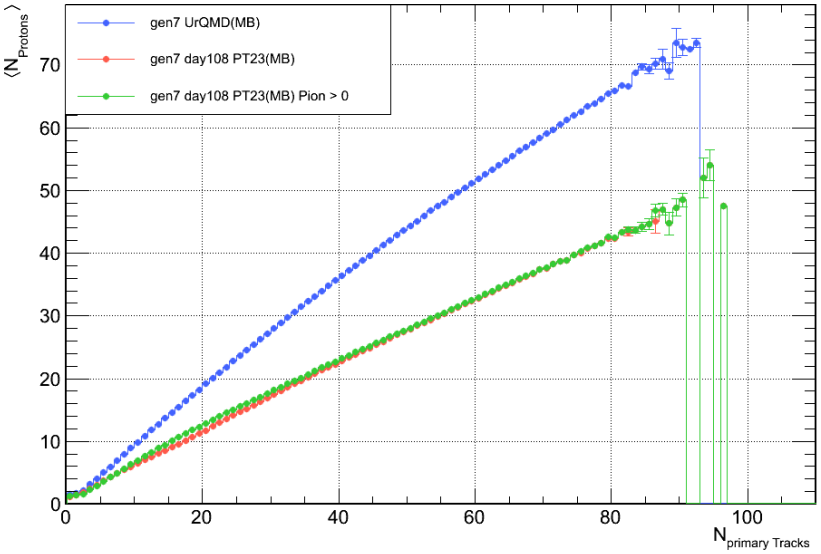

Figure 116: The mean proton event multiplicity as a function of $N_{primaryTrack}$ with (■) full MC (UrQMD), (■) minimum-bias data and additionally with the (■) condition to measure at least one identified pion.

charged pions are produced in the collision process, dependent on the

available energy, which scales with centrality. To exclude events with a low multiplicity of identified protons or pions this minimum condition was applied as additional event selection method. The difference between the mean proton multiplicity in data and simulation is mainly caused by the selection efficiency for the identified protons and the proton yield in UrQMD, neglecting here the production of clusters.

Pions vs. Npart

The scaling of the pion-production with centrality was measured first with the relativistic heavy-ion experiments at Bevalac [5, 11] and it

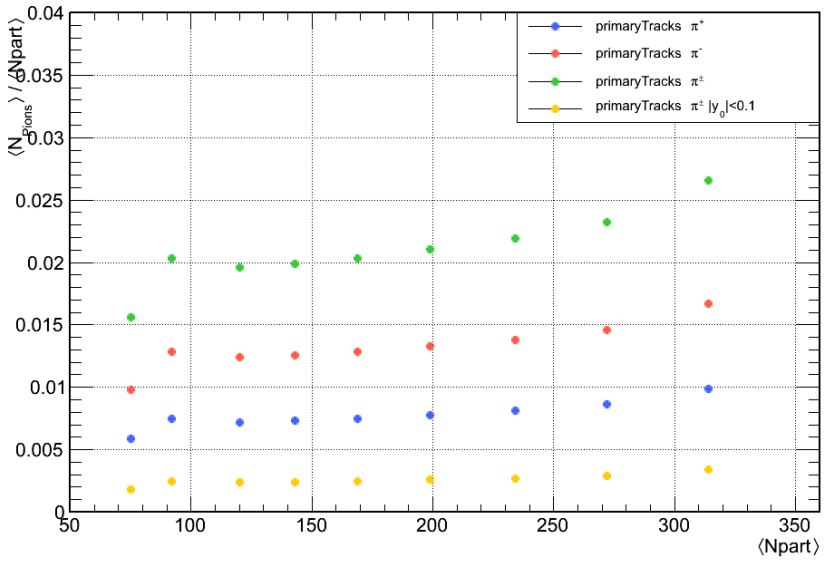

Figure 117: The uncorrected mean pion multiplicity divided by the average number of participants $\langle N_{pion}\rangle/\langle N_{part}\rangle$ as a function of $\langle N_{part}\rangle$ in 5% intervals centrality percentile estimated by *primary tracks*. (■) π^+ (■) π^- (■) $\pi^{\pm}$ and (■) at mid-rapidity measured $\pi^{\pm}$.

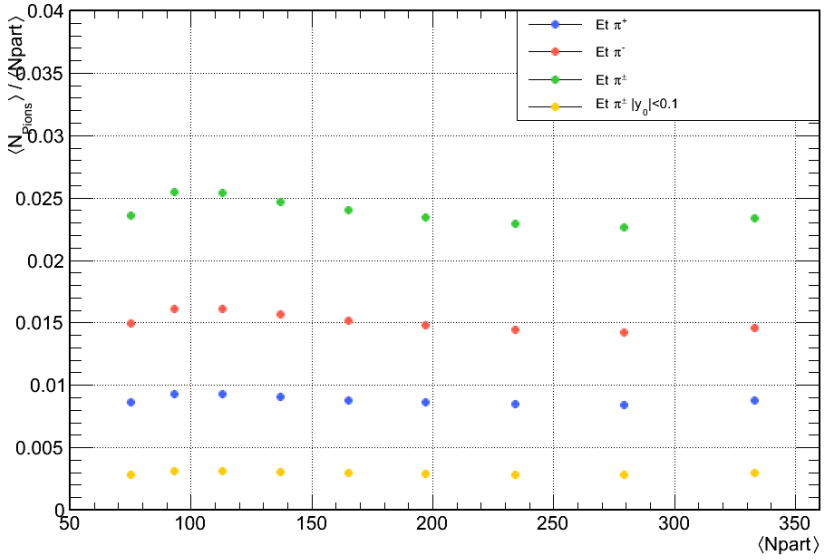

Figure 118: The uncorrected mean pion multiplicity divided by the average number of participants $\langle N_{pion}\rangle/\langle N_{part}\rangle$ as a function of $\langle N_{part}\rangle$ in 5% intervals centrality percentile estimated by E_t. (■) π^+ (■) π^- (■) $\pi^{\pm}$ and (■) at mid-rapidity measured $\pi^{\pm}$.

was suggested that the number of produced pions is scaling with the number of participating nucleons N_{part}. In an review [10] of experimental Au+Au data at collision energy of 1 AGeV at the SIS18 (TAPS, KaOS, FOPI) a value of 0.086 ± 0.1 pions per participating nucleon was determined. In figure 117 uncorrected mean event pion multiplicities

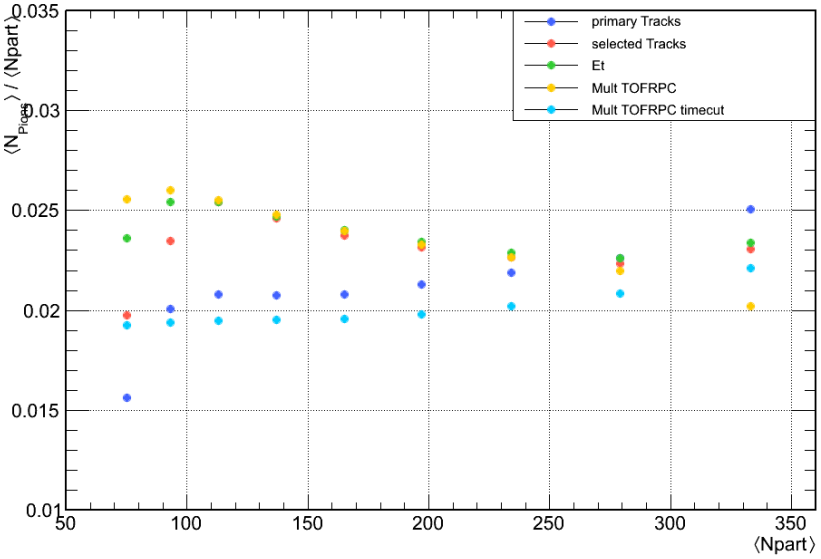

Figure 119: The uncorrected mean pion multiplicity divided by the average number of participants $\langle N_{pion} \rangle / \langle N_{part} \rangle$ as a function of $\langle N_{part} \rangle$ in 5% intervals centrality percentile estimated (■) *primary tracks* (■) *selected Tracks* (■) E_t and (■) TOFRPC-hits (■) TOFRPC-hits with timecuts.

per event and per number of participating nucleons is plotted against $\langle N_{part} \rangle$ in intervals of 5% centrality percentile, estimated by *primary tracks*. The figure 118 shows the same, but versus the centrality estimator E_T. The systematic difference between the used centrality estimators is shown in figure 119. To summarize, the ratio of the number of identified pions divided by the number of participating nucleons N_{part}, estimated by the different methods, shows here a consistent flat centrality dependence. The next step is the analysis of the yield of produced charge particle, in particular the corrected yield of the pion production, in terms of the centrality dependence. Based on the outcome of this systematic study of the different centrality estimators in comparison to the Glauber-fit, adjustments and calibrations of the estimator were done in preparation of the next data generation (gen8). Also new methods of event selection were developed to account for pile-up events. To correct the time dependent fluctuations of the track-based estimators, caused by the changing efficiencies of the MDC-detectors, a method based on the running mean of the used event multiplicity is implemented. The goal is to further improve the response of the estimators in terms of accuracy and resolution. Further on the systematic uncertainties in the estimation of the centrality classes have to be evaluated for the next data generation (gen8).

Bibliography

[1] A. Akindinov and other. "Performance of the ALICE Time-Of-Flight detector at the LHC". English. In: *The European Physical Journal Plus* 128.4, 44 (2013). DOI: 10.1140/epjp/i2013-13044-x.

[2] T. Aumann et al. "Inclusive measurements of electromagnetic dissociation of ^{197}Au targets". In: *Phys. Rev. C* 47 (4 Apr. 1993), pp. 1728–1737. DOI: 10.1103/PhysRevC.47.1728.

[3] W. Bayer, U. Scheeler, and Petra Schütt. "Accelerator Operation Report". In: vol. 2013-1. Darmstadt: GSI Helmholtzzentrum für Schwerionenforschung, 2013, 255–p. URL: http://repository.gsi.de/record/52152.

[4] P. Beckmann et al. "Collective azimuthal alignment in relativistic heavy ion reactions". In: *Modern Physics Letters A* 02.03 (1987), pp. 163–168. DOI: 10.1142/S0217732387000215.

[5] J. W. Harris et al. "Pion production in high-energy nucleus-nucleus collisions". In: *Phys. Rev. Lett.* 58 (5 Feb. 1987), pp. 463–466. DOI: 10.1103/PhysRevLett.58.463.

[6] Claudia Höhne. *System-Size Dependence of Strangeness Production in Heavy-Ion Collisions at 158 AGeV*. 2003. URL: http://archiv.ub.uni-marburg.de/diss/z2003/0627.

[7] W. Reisdorf et al. "Central collisions of Au on Au at 150, 250 and 400 A·MeV". In: *Nuclear Physics A* 612.3–4 (1997), pp. 493 –556. ISSN: 0375-9474. DOI: 10.1016/S0375-9474(96)00388-0.

[8] W. Reisdorf et al. "Systematics of central heavy ion collisions in the regime". In: *Nuclear Physics A* 848.3–4 (2010), pp. 366 –427. ISSN: 0375-9474. DOI: 10.1016/j.nuclphysa.2010.09.008.

[9] R. Schicker and Haralabos Tsertos. "Simulation studies of the HADES first level trigger. Part 1: Performance in heavy ion induced reactions". In: *Nucl. Instrum. Meth. A* (1996). arXiv:nucl-ex/9610002 [nucl-ex].

[10] P Senger and H Ströbele. "Hadronic particle production in nucleus-nucleus collisions". In: *Journal of Physics G: Nuclear and Particle Physics* 25.5 (1999), R59. URL: http://stacks.iop.org/0954-3899/25/i=5/a=201.

[11] R. Stock. "Particle production in high energy nucleus-nucleus collisions". In: *Physics Reports* 135.5 (1986), pp. 259 –315. ISSN: 0370-1573. DOI: 10.1016/0370-1573(86)90134-1.

Danksagung

Mein größter Dank gilt meinem Diplomvater Christoph Blume für die Möglichkeit meine Diplomarbeit in seiner Arbeitsgruppe anfertigen zu können, für seine stetige Hilfe bei Fragen, seine fortlaufende Unterstützung und seine Begeisterungsfähigkeit für das Themenfeld. Unter anderem möchte ich mich für die Gelegenheit bedanken an zwei Test-Strahlzeiten am CERN und einer am MAMI-Beschleuniger teilnehmen zu können, sowie der damit verbundenen lehrreichen Erfahrungen mit dem Handwerk des Detektorbau und der Feinheiten der Detektorauslese.

Ein großer Dank geht an Tetyana Galatyuk für die Zweit-Korrektur meiner Arbeit, die Unterstützung während der Tests der ECAL-Frontend-Boards im neu aufgebauten Detektor-Labor und die Hilfestellungen und detaillierten Erklärungen bei der Analyse der Gold-Gold Daten.

Außerordentlicher Dank gilt auch Reinhard Stock, von dessen Wissen ich bei jedem unserer Gespräche im höchsten Maße profitierte. Auch an Herbert Ströbele geht mein Dank, ohne seine Motivation ich den Unterschied zwischen *wounded* und *participating nucleons* in meiner Arbeit nicht explizit aufgegriffen hätte.

Meinen Arbeitskollegen Julian Book und Hans Beck möchte ich besonders herzlich danken für die spannenden Diskussionen, die regelmäßigen Kaffeepausen und die aufmunternden Worten, meinen HADES Mitstreitern Heidi, Timo, Patrick, Katharina, Claudia für die schöne Zeit abseits der Physik bei einem Bierchen, sowie meinen CBM-TRD Beamtime Mitstreitern Florian, Susanne und Milad bei einem Weinchen.

Ich möchte der gesamten HADES Kollaboration, für Ihre warmherzige Aufnahme, der sehr angenehmen Atmosphäre und den lehrreichen Diskussionen danken. Insbesondere bei Ilse und Wolfgang König möchte ich mich für ihre Expertise bedanken und für die interessanten Gespräche über ihre Erfahrungen im Physikalltag. I would like to thank Piotr Salabura and Grzegorz Korcyl for their help in the setup and running of the *Cracow* ecal read-out and also many thanks to Pavel Tlusty and Ondřej Svoboda for their support in all technical question about the ECAL-modules and further on in the event characterization of the gold-gold data.

Ein riesiges Dankeschön geht an Marianne Frey für ihre herzliche Art und ihr Organisationstalent, sowie an Werner Amend, Ulrich Köpf und allen Mitgliedern des IKF, die einem immer spontan bei jeglichen Problemen oder Fragen zur Seite stehen.

Besonders meinem Vater und meiner Schwester danke ich für ihre Kraft, ihr Verständnis und ihren Rückhalt, die diese Arbeit erst ermöglicht haben. Abschließend möchte ich mich bei Jana bedanken, dafür dass sie alle wichtigen Dingen im Leben im Blick hat und mir jeden Tag versüßt.

Erklärung

Ich versichere hiermit, dass ich die vorliegende Arbeit selbständig verfasst, keine anderen als die angegebenen Hilfsmittel verwendet und sämtliche Stellen, die benutzten Werken im Wortlaut oder dem Sinne nach entnommen sind, mit Quellen– bzw. Herkunftsangaben kenntlich gemacht habe.

Frankfurt am Main, den 22. Juni 2015

Behruz Kardan